Curso 2012/13
CIENCIAS Y TECNOLOGÍAS/15
I.S.B.N.: 978-84-15910-74-9

MARÍA TRINIDAD TAPIA PERALTA

Minor Merger Effects on Galaxy Evolution

Director
MARC BALCELLS COMAS

SERVICIO DE PUBLICACIONES
UNIVERSIDAD DE LA LAGUNA

SOPORTES AUDIOVISUALES E INFORMÁTICOS
Serie Tesis Doctorales

Examination date: december, 2012
Thesis supervisor: Marc Balcells Comas

ISBN: xx-xxx-xxxx-x
Depósito legal: TF-xxxx/2012

a Carmen,
y Francisco

Agradecimientos

Concluir un proyecto que conlleva tanto esfuerzo como lo es una tesis doctoral, me obliga a reflexionar sobre las circunstancias y las personas que han contribuido a que esto sea posible.

Quisiera agradecer a mi director de tesis, Marc Balcells, por compartir su experiencia y por su invaluable guía durante estos años. De igual manera, a César, Carmen, Nacho y Patricia por hacerme partícipe de sus ideas.

A mis padres y a mi hermana, por apoyarme incondicionalmente, incluso cuando ello ha significado poner miles de kilómetros entre nosotros.

A mis amigos y compañeros de despacho, por compartir esta aventura. Especialmente a Víctor, Mireia, Jose, María y Andrés por haberse convertido en mi familia por adopción.

A todos ustedes mil gracias,

Trini

Resumen

Esta tesis trata de los efectos que la acreción de satélites produce en la dinámica de las galaxias, usando métodos basados en simulaciones de N-cuerpos. Esta organizada en tres grandes temas: el primero trata sobre la evolución en tamaño de las galaxias compactas a alto desplazamiento al rojo; el segundo, sobre el gradiente de metalicidad que exhiben los remanentes de dichas galaxias, y el tercero acerca de la conexión entre la acreción de satélites y el engrosamiento del disco.

En el modelo jerárquico de formación y evolución de galaxias (White & Rees 1978), las fusiones juegan un papel crucial. Por lo tanto, es importante estudiar el efecto que la acreción de satélites tiene en la evolución de las galaxias. Fue a partir del trabajo pionero de Toomre & Toomre (1972) que las peculiaridades morfológicas comenzaron a ser consideradas como el resultado de interacciones de marea, y surgió la pregunta acerca de la conexión entre colisiones entre galaxias y la actividad nuclear en galaxias. Desde entonces ha habido un incesante acopio de evidencias teóricas y observacionales reforzando la idea de que las fusiones constituyen uno de los procesos más importantes en la evolución de las galaxias.

En las fusiones mayores (razón de masa menor o igual a 4:1), el remanente exhibe propiedades muy diferentes de las de cualquiera de sus galaxias progenitoras debido al cambio violento en su campo gravitatorio (e.g. van Albada 1982; Kennicutt et al. 1987; Kormendy & Kennicutt 2004; González-García & Balcells 2005; Cox et al. 2006; Bournaud et al. 2011; Prieto et al. 2012). En contraste, las fusiones menores, en las cuales una de las galaxias es mucho menor que la otra (razón de masa mayores a 10:1), producen únicamente cambios pequeños en la galaxia mayor (e.g. Athanassoula et al. 1997; Aguerri et al. 2001; Eliche-Moral et al. 2006; Hopkins et al. 2008b; Combes 2009; Villalobos et al. 2010).

Se ha encontrado que las fusiones son el proceso por excelencia para explicar

la formación de galaxias elípticas de masa intermedia y de estructuras a pequeña escala perdurables tales como cúmulos globulares masivos, colas de marea, corrientes (del inglés *streams*), núcleos centrales desacoplados, etc., (Bournaud 2009). Sin embargo, este escenario está en contradicción con la existencia de galaxias sin bulbo o puramente discoidales (van den Bosch 2001; Abadi et al. 2003a; D'Onghia & Burkert 2004; Kormendy & Fisher 2005), fallo directamente relacionado con la alta tasa de fusiones característica de un escenario de formación jerárquica como es el ΛCDM.

La relevancia de las fusiones para el crecimiento cosmológico y la transformación de galaxias depende del número de fusiones que una galaxia experimenta a lo largo de su vida. Este es usualmente cuantificado mediante la tasa de fusiones, que se define como el número medio de fusiones que una galaxia típica sufre por Giga-año, la cual se estima combinando medidas observacionales de la fracción de galaxias en fase de fusión (a partir de distorsiones o de estadística de pares), con determinaciones del tiempo de fusión a partir de simulaciones y modelos simplicados (e.g. Mihos 1995; Conselice 2006). Estudios han encontrado que el número medio de fusiones calculados a partir de simulaciones cosmológicas son mayores que los observados (Quilis & Trujillo 2012 y referencias contenidas). De igual manera, es objeto de debate la relativa importancia de las fusiones mayores o menores y su dependencia con el desplazamiento al rojo (z); por ejemplo, López-Sanjuan et al. (2010) encuentran que las fusiones mayores juegan un papel menor en la formación de galaxias elípticas de masa intermedia, favoreciendo una formación a través de fusiones menores.

Existen aún preguntas abiertas acerca del papel que las fusiones juegan en la formación de las galaxias actuales. En esta tesis, nos hemos enfocado en tres de ellas. Concretamente, nos planteamos los siguientes objetivos: (1) en un escenario cosmológico de crecimiento jerárquico dominado por energía oscura y materia oscura fría, determinar usando simulaciones de N-cuerpos si la historia de fusiones típica de una galaxia elíptica explica el crecimiento observado en el radio efectivo, cuando se incluyen únicamente procesos de dinámica gravitatoria, es decir, no se incluyen procesos de formación estelar. Ver Capítulo 3. (2) Como verificación del modelo de fusiones menores para el crecimiento de elípticas, predecir el rango de gradientes de metalicidad que se espera encontrar en galaxias elípticas a $z = 0$, a partir de una suposición sobre el gradiente de poblaciones inicial de la galaxia. Ver Capítulo 4. (3) Como test de los efectos de las fusiones menores en galaxias de disco, estudiar la contribución de estas fusiones al calentamiento dinámico del disco y a la deposición de material acretado proveniente del satélite; estudiar específicamente los efectos numéricos en las medidas del calentamiento de discos galácticos. Ver Capítulo 5. Las conclusiones del trabajo se presentan en el Capítulo 6.

Evolución en tamaño de las galaxias elípticas en un universo ΛCDM

En el capítulo 3 estudiamos la evolución en tamaño de las galaxias elípticas en un universo ΛCDM. Estudios observacionales de galaxias masivas han revelado que estas galaxias eran extremadamente compactas a desplazamientos al rojo mayores (Daddi et al. 2005; Trujillo et al. 2007; van Dokkum et al. 2008; Pérez-González et al. 2008; Buitrago et al. 2008). Sin embargo, tales galaxias compactas no se observan en el universo local (Bernardi et al. 2006; Trujillo et al. 2009; Ferré-Mateu et al. 2012), lo que implica que las galaxias masivas han experimentado una evolución en tamaño hasta la época actual. Para explicar tal evolución se ha sugerido que las fusiones "secas" (pobres en gas) con galaxias menos densas son el mecanismo más prometedor para transformar una galaxia compacta a alto z en una galaxia elíptica actual (Naab et al. 2007; Kaviraj et al. 2009; Hopkins et al. 2010a; Oser et al. 2012; Whitaker et al. 2012; Hilz et al. 2012).

Dado que sigue sin esclarecerse si simulaciones de formación de galaxias en un entorno cosmológico son capaces de reproducir la diversidad de galaxias observadas a alto y bajo z (Kaufmann et al. 2012), hemos elaborado un conjunto de simulaciones con el objetivo de analizar si en un marco de referencia cosmológico la acreción "seca" de satélites es capaz de producir el crecimiento en tamaño observado en las galaxias masivas a alto desplazamiento al rojo. Para ello, hemos extraído de simulaciones cosmológicas la historia de fusión, la razón de masas y las órbitas de ocho galaxias elípticas para re-simularlas a alta resolución con nuestro modelo de galaxia compacta a alto z. Debido a que las simulaciones cosmológicas carecen de resolución numérica suficiente para extraer información acerca de la forma de las galaxias, hemos supuesto que éstas, al igual que las galaxias progenitoras, son galaxias elípticas y que sus tamaños obedecen relaciones observacionales (Shen et al. 2003; Trujillo et al. 2006). Hemos encontrado que todos los remanentes son menos compactos que sus galaxias progenitoras a desplazmiento al rojo elevados ($z = 2$) como resultado de la fusión en la que los satélites depositan material en las partes externas de la galaxia, produciendo así su crecimiento. La acreción de satélites produce un crecimiento en tamaño en un factor 4 en radio y un factor 2 en masa, lo cual es compatible con lo observado.

En la figura 1, mostramos la evolución del radio efectivo y la dispersión de velocidades para una de nuestras historias de fusion, en la cual la galaxia progenitora acreta ocho satélites (indicados por la lineas azules en el panel superior). Las bandas horizontales denotan los intervalos de tiempo en los cuales la simulación no fue computada. Se observa un gran incremento en el radio efectivo de ∼4.9 mientras que la dispersión de velocidades cambia en apenas un factor ∼1.1.

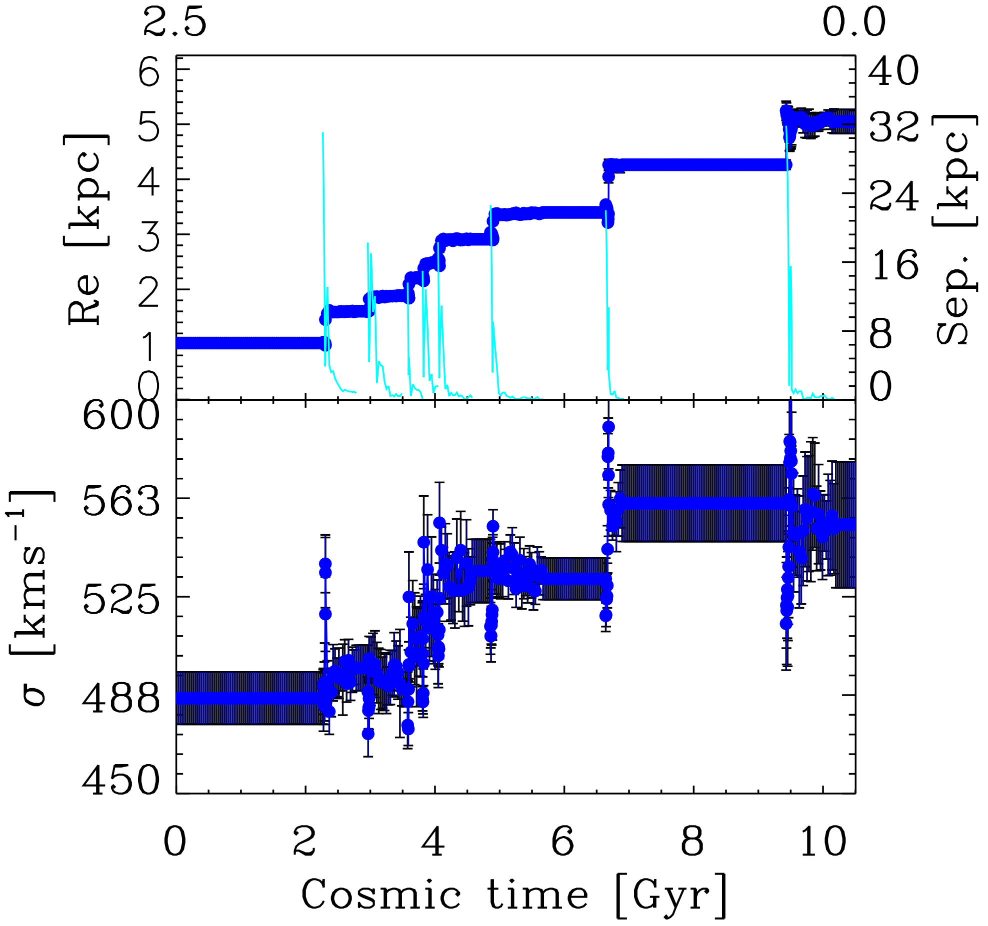

FIGURE 1— Evolución temporal de una de nuestras historias de fusión, la número 7 (ver Tablas 3.2 y 3.3). Panel superior: evolución temporal del radio efectivo. La separación entre la mediana de la distribución de masa de la galaxia principal y la mediana de la distribución de masa del satélite se muestra en color azul. Panel inferior: Evolución temporal de la dispersión de velocidades.

En la aproximación simplista de que las ocho elípticas simuladas son una muestra representativa de la población de elípticas masivas entre $z = 2$ y $z = 0$, esperamos las relaciones entre radio efectivo medio $r_{\rm e}$, desplazamiento al rojo z, dispersin de velocidades σ y masa estelar $M_\star$ que se muestran en las ecuaciones

1 a 4:

$$\mathrm{r_e} = (6.882 \pm 0.050\ \mathrm{kpc})\,(1+\mathrm{z})^{-1.738\pm0.121} \tag{1}$$

$$\sigma/\sigma(\mathrm{z}=2.5) = \left(279.534 \pm 0.005\ \mathrm{kms^{-1}}\right)(1+\mathrm{z})^{-0.123\pm0.018} \tag{2}$$

$$\mathrm{r_{ef}}/\mathrm{r_e}(\mathrm{z}=2.5) = (1.182 \pm 0.035)\left(\frac{\mathrm{M_{\star f}}}{\mathrm{M_\star(z=2.5)}}\right)^{(1.547\pm0.147)} \tag{3}$$

$$\sigma_\mathrm{f}/\sigma(\mathrm{z}=2.5) = (1.008 \pm 0.011)\left(\frac{\mathrm{M_{\star f}}}{\mathrm{M_\star(z=2.5)}}\right)^{(0.044\pm0.038)} \tag{4}$$

para el radio y la dispersión de velocidades respectivamente.

Con nuestros remanentes, hemos explorado la relación entre la masa dinámica y la masa estelar para un mismo objeto, donde hallamos que nuestros remanentes satisfacen $M_{dyn} \approx 2\left(\sigma^2 r_e/G\right)$, que corresponde a un escalado notablemente menor que el valor tomado por canónico para galaxias elípticas a $z=0$, $M_{\mathrm{dyn}} = 5(\sigma^2 r_{\mathrm{e}}/G)$ (Cappellari et al. 2006).

Como conclusión, encontramos que las fusiones “secas” de satélites con contrastes de densidades realistas en un entorno cosmolgíco son capaces de reproducir la evolución en tamaño de las galaxias elípticas masivas.

Efectos de las fusiones secas sobre los gradientes de metalicidad de galaxias elípticas masivas

En el capítulo 4 estudiamos los efectos de las fusiones secas sobre los gradientes de metlicidad de las galaxias elípticas masivas. En el escenario de formación jerárquica de galaxias, es más complicado establecer predicciones sobre el gradiente de metalicidad resultante en el remanente de una fusión, dado que este depende de un gran número de parámetros libres (Sánchez-Blázquez et al. 2007). Puesto que los satélites son los responsables del cambio en metalicidad debido a que depositan su estrellas en las partes externas, es interesante observar las características específicas en el perfil de metalicidad a distancias radiales donde el material acretado empieza a ser apreciable.

Nuestras simulaciones de la historia de fusión de galaxias elípticas masivas en una cosmología ΛCDM proporcionan modelos ideales para estudiar el efecto que las fusiones “secas” producen en los gradientes de metalicidad de las galaxias elípticas actuales. Para realizar dicho estudio, hemos tomado un subconjunto representativo de nuestras historias de fusión y, asumiendo que nuestros modelos obedecen relaciones masa-metalicidad observadas, hemos asignado a cada galaxia una metalicidad inicial (Vale Asari et al. 2009) así como un gradiente radial (Spolaor et al. 2009) en fución de su masa y el desplazamiento al rojo al cual fue acretada, obteniendo así los perfiles radiales de metalidad del remanente. Encontramos que el efecto de acretar satélites es producir un gradiente de metalicidad menos profundo y que un número más alto de satélites acretados tiende a producir perfiles más suaves que cuando se acreta un numero inferior de galaxias, aunque la masa depositada sea similar. Así mismo, encontramos que la amplia dispersión encontrada en nuestros resultados es compatible con la dispersión en los gradientes de metalicidad observados en galaxias elípticas masivas (e.g. Gorgas et al. 1990; Fisher et al. 1995; Sánchez-Blázquez et al. 2006; Mehlert et al. 2003; Koleva et al. 2011). Nuestro resultado sugiere que, solo por el hecho de que la mezcla debido a las fusiones no es completa y que la masa se deposita preferentemente en las partes externas de la galaxia, el efecto combinada de fusiones entre $z = 2$ y$z = 0$ es de aplanar el perfil de metalicidad, por lo que el gradiente final es ∼40% del gradiente a $z \sim 2$.

Fusiones menores y engrosamiento del disco

El disco grueso constituye un componente general en galaxias de disco (ver Dalcanton & Bernstein 2002; Yoachim & Dalcanton 2006); sin embargo, su mecanismo de formación todavía no es entendido (van der Kruit & Freeman 2011). Las fusiones menores contribuyen al crecimiento de un disco grueso mediante dos mecanismos cualitativamente distintos: mediante estrellas del disco grueso de galaxias externas que subsiguientemente son depositadas por un evento de acreción a altas alturas-de-escala (e.g. Abadi et al. 2003b; Yoachim & Dalcanton 2005); en el segundo caso, las estrellas del disco grueso se forman inicialmente en el disco delgado y son dinámicamente calentadas a alturas-de-escala mayores por choques con los satélites (e.g. Quinn et al. 1993; Walker et al. 1996; Robin et al. 1996; Velazquez & White 1999; Chen et al. 2001; Aguerri et al. 2001).

Para estudiar el engrosamiento del disco grueso por acreción de satellites, hemos creado una batería de modelos consistente en una galaxia de disco huésped y un satélite que es una réplica escalada del mismo, el cual hemos construido utilizando tres números diferentes de partículas con el fin de caracterizar el efecto de la resolución numérica, seleccionando dos razones de masa entre la galaxy huésped y su satélite así como dos tipos de órbitas (directa y retrógrada). Encontramos que los satélites construidos con un factor $\alpha_{TF} = 3.5$ son completamente destruidos, formando puentes y colas de marea que conectan ambas galaxias. El proceso de acreción produce el engrosamiento del disco en un factor ~ 2.7–3.5. De las medidas de la distribución vertical se desprende que el remanente esta dominado por la distribución vertical del disco de la galaxia húesped y que el disco del satélite contribuye a enriquecer las partes más externas del disco de dicha galaxia. El bulbo de la galaxia satélite contribuye a la estructura interna del remanente (ver Figura 2). Después de corregir nuestros valores de la distribucin vertical del disco por calentamiento a dos cuerpos (*two-body effect*) no se encontró una relación clara entre el numero de partículas y el valor de la mediana de la distribución vertical, por lo que las diferencias en las medidas se deben a inestabilidades globales que se propagan. Hemos comparado un subconjunto de nuestros modelos con los modelos publicados por Eliche-Moral et al. (2006) y encontramos un buen acuerdo entre las medidas con un coeficiente de correlación de Pearson de $\sim$ 0.90 para los casos directos y 0.88 para los casos retrógrados. Además, encontramos que órbitas retrógradas tienden a engrosar el disco en la parte más externa mientras que los casos directos son más eficientes engrosando el disco a radios más internos.

Encontramos que la acreción de un satélite produce el engrosamiento del disco, generando una estructura en forma de cuña, formada tanto por restos del satélite como por material del disco delgado que ha sido calentado dinámicamente. Adicionalmente, vemos que un solo satélite de baja masa no es suficiente para perturbar el disco en gran medida y para generar isofotas de densidad cuadradas que se esperarían encontrar en un disco grueso (Bournaud et al. 2009).

Conclusiones de la tesis

Como conclusión, a través del análisis de la evolución en tamaño de las galaxias compactas a alto desplazamiento al rojo, hemos encontrado que nuestro estudio favorece el modelo de formación jerárquica, en el que las galaxias no han sido formadas a partir de un colapso monolítico simple, sino por procesos de fusión. Sin embargo, si consideramos los gradientes de metalicidades, encontramos que el escenario del colapso monolítico no puede ser completamente descartado y que se necesitan más estudios para validar cualquiera de los escenarios para la evolución de las galaxias masivas. Un estudio futuro consistiría en cambiar las galaxias de nuestras historias de fusión por galaxias tipo disco, pues se ha encontrado que una gran fracción de galaxias masivas alto desplazamiento son de este tipo (van der Wel et al. 2011; Weinzirl et al. 2011; Szomoru et al. 2012), y explorar si mediante esos modelos somos capaces de generar las propiedades de la galaxias elípticas actuales.

Respecto a las fusiones menores y la formación del disco grueso, concluimos que con un solo satélite no es posible discernir cualitativamente el mecanismo de engrosamiento del disco. Los futuros estudios irán encaminados a considerar un entorno cosmológico que reproduzca posibles historias de acreción para la Vía

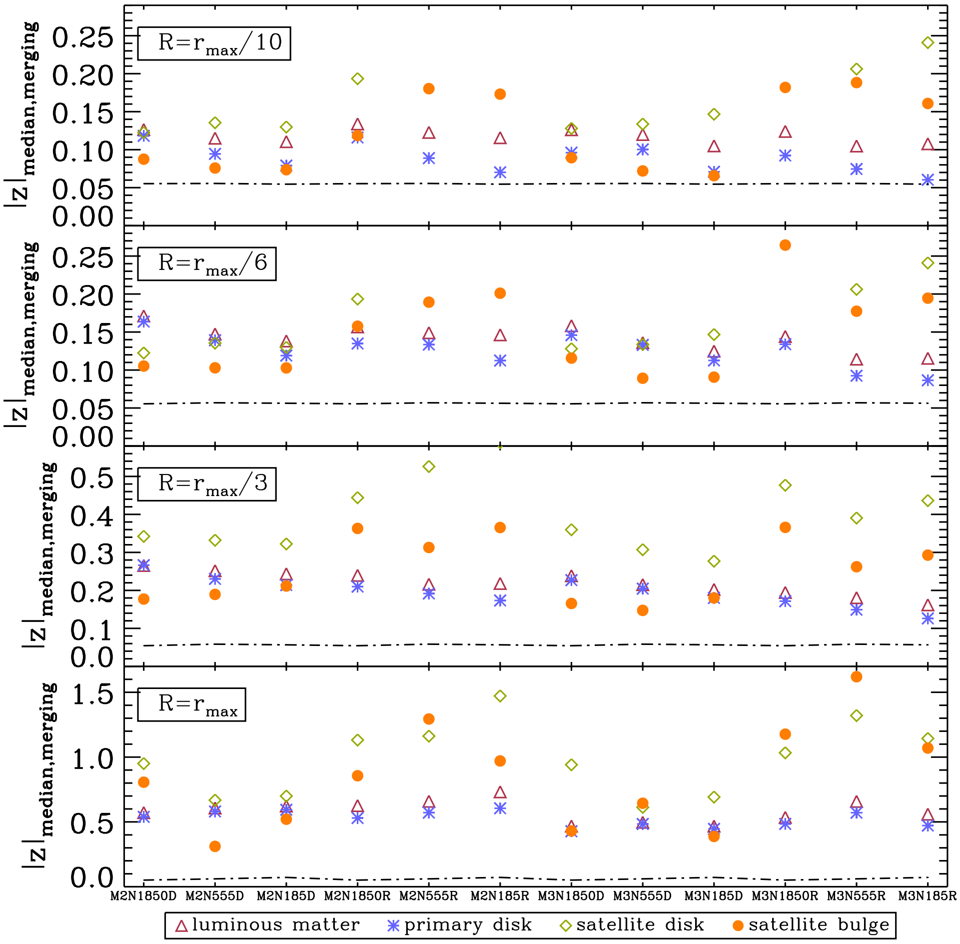

FIGURE 2— Medianas de la distribución vertical para cada remanente, corregido por el efecto de dos-cuerpos. Los triángulos rojos corresponden al total de la materia luminosa, los asteriscos azules a las partículas luminosas que originalmente formaban el disco del galaxia principal; los diamantes verde-lima corresponden al disco del satélite y los círculos naranjas a la materia luminosa del bulbo del satélite. Panel superior: medidas al radio más interno que representa ∼10% de la longitud inicial del disco de la primaria. Panel medio-superior: medidas del radio fijo que contiene ∼ 20% de la longitud inicial del disco de la primaria. Panel medio-inferior: medidas que aproximadamente coinciden con el radio de media masa de la galaxia principal. Panel inferior: medidas al máximo radio. Dado sue las partículas del bulbo del satélite no alcanzan radios tan externos, su presencia es insignificante. En todos los paneles la línea quebrada corresponde a la escala-de-altura inicial (z_D= 0.1) .

Láctea, lo que además nos permitiría una comparación directa con la misma.

Abstract

In this thesis we study the effect that minor mergers have on the evolution of galaxies. We focus on three topics: the size evolution of massive elliptical galaxies, metallicity gradients in elliptical galaxies, and the formation of the thick disc.

To study if, in a ΛCDM universe, cosmological dry merger histories can generate the observed size evolution of massive elliptical galaxies, we analyzed eight different high-resolution merger histories of massive elliptical galaxies. The mass ratio and orbital parameters of these galaxies were extracted from self-consistent cosmological simulations, and we followed observational relationships to set their sizes. Our progenitor galaxies at $z = 2$ resemble observed high-redshift galaxies with $r_e \sim 1$ kpc with a mass range between $5.21 \times 10^{10}\mathrm{M}_{\odot}$ and $2.18 \times 10^{11}\mathrm{M}_{\odot}$, and a variety of velocity dispersions from $\sim 236\ \mathrm{km\,s^{-1}}$ to $\sim 486\ \mathrm{km\,s^{-1}}$. We find that the median growth is a factor 4 in size and a factor 2 in mass from z=2 to z=0, with a moderate increase of the velocity dispersion.

To study if sequential dry minor mergers induce a gradient of metallicity in the remnant of a high redshift, massive elliptical galaxy, we have estimated the metallicity gradients of a representative subsample of our merger histories from Chapter 3 in order to examine whether we can reproduce the metallicity gradients observed in present-day elliptical galaxies by following observational mass-metallicity relationships for our cosmological-motivated dry mergers remnants. We find that the metallicity profiles are approximately linear with $\log(r)$, and that the effect of accreting satellites is to produce a shallower metallicity gradient. The final gradients are consistent with those observed in $z = 0$ massive ellipticals. A high number or sequential accretions tend to produce a smoother metallicity gradient than fewer merger events, even when the total accreted mass is approximately the same. We also find a large scatter in the observed gradients, which scales with the number of sequential accretions and which is compatible with the large scatter in metallicity gradients observed in massive

ellipticals.

Within the merger-driven scenarios, there are two qualitatively different corresponding mechanisms. In the first case, thick-disc stars form in external galaxies and are subsequently deposited by accretion events at large scale heights (e.g. Abadi et al. 2003b; Yoachim & Dalcanton 2005). To study the effects of minor mergers on disc thickening, focussing on quantifying the effects of numerical heating, we perform a suite of merger experiments of the single accretion of one satellite onto a disc galaxy, using a range of mass ratios, orbital types and number of particles. Our conclusion is that both mechanisms, the accretion of satellites and the heating of the disc, play a role in the building of the thick disc in the merger-driven scenario. The accretion of a satellite results in the deposition of mass in the outer parts and the injection of kinetic energy into the disc, thus heating the disc and enhancing the settling of thin disc material into greater heights. We stress the necessity of more than one satellite to shape a thick disc by tidal debris of disrupted systems or to produce a big change in the direction of the angular momentum of the disc to generate a slowly rotating or counterrotating thick disc. Also, we find that the single accretion of a low-mass satellite produces a thickening of a factor $\sim$ 2.7–3.5. Nevertheless, it is not sufficient to perturb the disc and to produce the boxy isophotes expected if the thick disc is formed by mergers.

Contents

Agradecimientos **v**

Resumen **vii**

Abstract **xvii**

1 Introduction **1**

1.1 Galaxies 1

1.1.1 General properties 1

1.1.2 Morphological properties 2

1.1.3 Classification schemes 3

1.2 Galaxy formation models 6

1.2.1 Monolithic collapse 6

1.2.2 Hierarchical galaxy formation 6

1.3 Mergers 7

1.3.1 Mergers of disc galaxies 8

1.3.2 Mergers of elliptical galaxies 9

1.4 Merger rate measurements 9

1.5 Present challenges 10

1.5.1 Size evolution of massive elliptical galaxies 10

1.5.2 Disc thickening in disc galaxies 12

1.6 N-body simulations 12

1.6.1 Relevant dynamics 13

1.6.2 Numerical methods 13

1.6.3 Software environments 16

1.6.4 Specialised hardware methods 16

1.7 Motivation of the thesis 16

2 Objectives 19

3 Size evolution of elliptical galaxies in a λCDM universe 21
3.1 Introduction 21
3.2 Motivation 23
3.3 Models and simulations 24
  3.3.1 Galaxy model 24
  3.3.2 Properties of the galaxy model 26
3.4 Merger trees 28
  3.4.1 Progenitor galaxies 29
  3.4.2 Merger histories 33
  3.4.3 Size of the satellites 33
3.5 Computational aspects 34
  3.5.1 Particles in the merger trees 34
  3.5.2 Runs 34
  3.5.3 Energy conservation 36
3.6 Methods 39
  3.6.1 Effective radius 39
  3.6.2 velocity dispersion 40
  3.6.3 Stellar mass 41
  3.6.4 Dynamical mass 41
  3.6.5 Surface density profile 42
3.7 Results 42
  3.7.1 Stellar surface density profile 42
  3.7.2 Effective radius and velocity dispersion 42
  3.7.3 Redshift evolution 44
  3.7.4 Stellar mass-size relation 47
  3.7.5 Dynamical and stellar masses 51
3.8 Conclusions 52
3.9 Future work 54

4 Effects of dry mergers on the metallicity gradients of massive elliptical galaxies 57
4.1 Introduction 57
4.2 Motivation 59
4.3 Sample 60
4.4 Observationally derived metallicity 60
  4.4.1 Total metallicity 60
  4.4.2 Radial metallicity gradient 61
4.5 Results and discussion 61

4.5.1 Remnant 2 62
4.5.2 Remnant 3 64
4.5.3 Remnant 7 64
4.5.4 Remnant 8 64
4.6 Conclusions 65
4.7 Future work 65

5 Minor mergers and disc thickening 67
5.1 Introduction 67
5.2 Motivation 70
5.3 Galaxy model 70
5.3.1 Building of the galaxy model 70
5.3.2 Parameters of the model 72
5.3.3 Satellite galaxy 72
5.3.4 Set of main galaxies 73
5.4 Suite of models 75
5.4.1 Orbital parameters 76
5.5 Computational details 77
5.5.1 Runs 77
5.6 Methods 77
5.6.1 Vertical distribution 77
5.6.2 Separation distance 79
5.6.3 Surface density 79
5.6.4 Rotation curve 79
5.7 Results 79
5.7.1 Surface density profile 80
5.7.2 Vertical distribution 80
5.7.3 Orbit-vertical scale relationship 88
5.7.4 Velocity dispersion profile 91
5.7.5 Isophotes 94
5.8 Conclusions 94
5.9 Future work 96

6 Conclusions 99

A Appendix section of chapter 3 103
A.1 Building spherical two-component model 103
A.1.1 Potential-density pair 103
A.1.2 Distribution functions of the models 105
A.2 GADGET-2 input file 108

B Appendix section of chapter 5 111
B.1 GADGET-2 input file 111
B.2 Queue system 114
B.3 Orbit of the encounter 114

Bibliography 117

1

Introduction

The study of the universe has been a constant since the origins of mankind, it has involved science, philosophy, esotericism and religion. From the cosmogony of the ancient civilizations, the ideas of the aristotelian universe, to the medieval conception, there has been a constant effort to figure out “what is going on out there”. The rise of astronomy as we conceive it today has been a long journey full of milestones. Just to mention some of them: the first observations with a telescope by Galileo in 1609, the legacy of Isaac Newton, the discovery of other planets like Uranus by William Herschel in 1781, the use of photography in astronomy, the development of the theory like Einstein’s relativity, the discovery of the Big Bang’s echo in 1965 and, more recently, the building of large telescopes (Bachiller 2009).

1.1 Galaxies

1.1.1 General properties

We define galaxy as an object formed by stars, gas in different phases (ionized, neutral, either atomic or molecular) and dust, which is gravitationally bound and remains in dynamical equilibrium due to the rotation or the velocity dispersion, or a combination of both, and has a stellar mass from around 10^7 $M_\odot$ to about 10^{12} $M_\odot$ (the low boundary is imposed to distinguish galaxies from globular clusters). It is widely accepted today that galaxies also contain vast amounts of dark matter, generally assumed to be non baryonic.

According to their physical size and mass, galaxies can be classified as dwarf, normal and giant galaxies. Sizes are usually parametrized by the half-mass radius and usually range from a few hundreds of parsecs (pc) for dwarf galaxies to few tens of kpc for giants. Galaxies show and approximate luminosity range in the R band from a few times 10^5 $L_\odot$ to around few times 10^{11} $L_\odot$.

The majority of galaxies are organized into a hierarchy of associations known as groups and clusters, which in turn usually form large superclusters. At the largest scale, these associations are generally arranged into sheets and filaments surrounded by immense voids.

1.1.2 Morphological properties

In optical images of galaxies we can distinguish morphological structures such as spheroids, disc, bars, arms, rings, shells and a stellar halo surrounding the galaxy. Such observed features allow us classify galaxies in four big types (Binney & Tremaine 2008):

Elliptical galaxies

Smooth and featureless stellar systems containing little or no cool interstellar gas or dust and little or no stellar disc. They have a range of R-band luminosities of $10^4 < L_\odot < 10^{12}$. The fraction of galaxies that are elliptical depends on the local density of galaxies, ranging from 10% in the field to 40% in the centre of dense clusters galaxies (Dressler 1980; Whitmore & Gilmore 1991). Their surface density profile follows on average a Sersic-law (Sersic 1968).

Elliptical galaxies follow tight scaling relations defined by their size, velocity dispersion, surface brightness and luminosity. The most commonly studied relations are: the luminosity/mass-size (Shen et al. 2003; McIntosh et al. 2005, the correlation between the velocity dispersion and with the absolute magnitude, the so-called Faber-Jackson relation (Faber & Jackson 1976), the Kormendy relation (Kormendy 1977) and the fundamental plane (Djorgovski & Davis 1987; González-García & van Albada 2003; Nigoche-Netro et al. 2009; La Barbera et al. 2010; Fernández Lorenzo et al. 2011).

Spiral galaxies

These galaxies contain a prominent disc composed of stars, gas, and dust. The disc contains spiral arms (filaments in which galaxies are continuously being formed). About 60% of all the luminous galaxies are spirals, but the fraction drops to $\leq$ 10% in the cores of galaxies clusters (Dressler 1980; Whitmore & Gilmore 1991).

The surface brightness in spiral galaxies discs, which traces the radial distribution of stars obeys an exponential law (de Jong 1996). Spiral galaxies have typical circular speed between 100 and 300 $\mathrm{km\,s^{-1}}$. The rotation rate of spirals in the flat part the circular-speed curve is related to their luminosity by the

Tully-Fisher law (Tully & Fisher 1977, see also Sakai et al. 2000 and references therein).

Most spiral galaxies contain a bulge, a centrally concentrated stellar system that has a smooth and amorphous appearance. The origin of bulges is not well understood: some resembles small elliptical galaxies and presumably formed in the same way, while others resemble thickened discs, and may have formed from the disc through dynamical processes (see Kormendy & Kennicutt 2004 for a review).

Spirals galaxies are also divided into "normal" or "barred". The bar is an elongated, smooth stellar system that is a reminiscent of a rigid paddle or stirrer rotating a the centre of the galactic disc. About half of all spirals are barred (Eskridge & Frogel 1999).

Lenticular galaxies

Lenticulars share properties with elliptical and spiral galaxies. Like spirals, they contain a rapidly rotating disc, a bulge, and sometimes a bar, and the disc obeys the exponential surface-brightness law characteristic of spirals. Like ellipticals, they have little or no cool gas or recent star formation, are smooth and featureless in appearance and exhibit no spiral structure. They comprise almost half of the galaxies in the high-density centers of galaxy clusters (see Aguerri 2012 for a review).

Irregular galaxies

These galaxies are characterized by the lack of a well defined shape, but often appear to be morphologically barred. They are extremely common, more than one third of our neighbors belong to this type (Whitmore & Gilmore 1991). A minority of galaxies are classified as irregular simply because they fit nowhere else: these include spiral or elliptical galaxies that have been violently distorted by a recent encounter with a neighbor, galaxies in last stages of merging, and galaxies undergoing and intense burst of star formation that overwhelms the stellar populations that usually determine the classifications.

1.1.3 Classification schemes

The most widely used classification scheme is that introduced by Hubble in his book *The realm of the Nebulae* (Hubble 1936). Hubble's scheme divides regular galaxies into three broad band classes: ellipticals, lenticulars and spirals. This scheme is often known as Hubble's tuning-fork diagram, after the shape in which it is traditionally represented (see Figure 1.1). Due to the belief that the Hubble sequence might indicate an evolutionary sequence (E $\rightarrow$ S0 $\rightarrow$ Sa $\rightarrow$

Sb → Sc → Sd → Sm → Irr), ellipticals and lenticulars were referred to as "early type", whereas spirals and irregulars were called "late type".

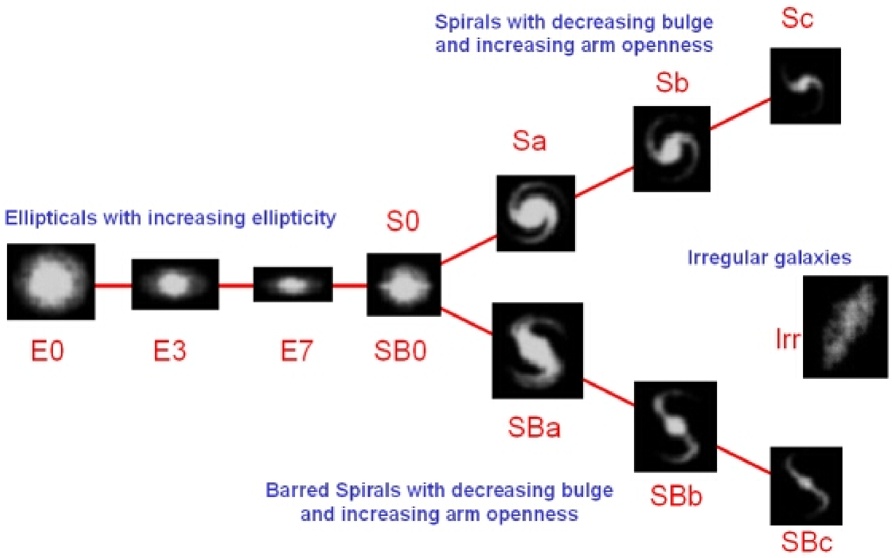

FIGURE 1.1— Hubble classification scheme. Elliptical galaxies: denoted with the letter "E" followed by an integer which characterises their apparent ellipticity. Shown to the right of the diagram, the spirals are divided into two parallel branches. The regulars occupy the upper branch and are denoted by the letter S, while the lower branch contains the barred spirals, which are given the symbol SB. Both types of spirals are further subdivided according to the detailed appearance of their spiral structures. Membership to one of these subdivisions is indicated by adding a lower-case letter to the morphological type. Lenticulars (S0), are located at the center of the diagram where the two spiral arms meet the elliptical branch. Irregulars (Irr) do not fit into the Hubble sequence because they have no regular structure. Figure credit: © Swinburne University of Technology.

This classification scheme was later expanded by de Vaucouleurs (1959), and the modern classification of galaxies, in which spirals are classified according to their luminosity class, was introduced by van den Bergh (1976). Recently, Kormendy & Bender (1996, 2012), updated van den Bergh's parallel sequence galaxy classification by proposing that S0 galaxies form a sequence S0a-S0b-S0c that parallels the sequence Sa-Sb-Sc of spiral galaxies. They extended the S0a-S0b-S0c sequence to spheroidal (Sph) galaxies that are positioned in parallel to irregular galaxies in a similarly extended Sa-Sb-Sc-Im sequence, and proposed that Sph galaxies of increasing luminosity form a continuous sequence with the discs (but not bulges) of S0c-S0b-S0a galaxies (as can be seen in Figure 1.2).

Remarkably, the Sph-S0-disc sequence is almost identical to that of Irr galaxies + spiral galaxy discs, suggesting that Sph galaxies are transformed "red and dead" Scd-Irr galaxies, in the same way that many S0 galaxies are transformed red and dead Sa-Sc spiral galaxies.

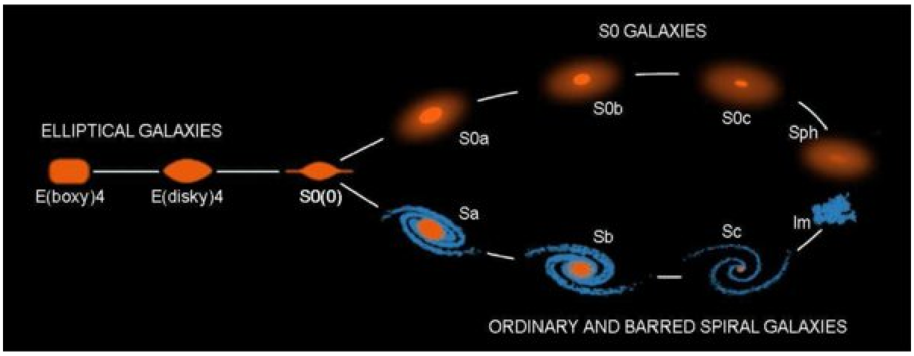

FIGURE 1.2— Schematic representation of the parallel-sequence morphological classification of galaxies envisaged by Kormendy & Bender (1996) which illustrates the proposed update in the Hubble's classification scheme for the evolution of the SO galaxies. Source: Kormendy & Bender (2012).

The visual classification of galaxies has the problem of its dependency on the human eye, and although it is done by specialists, it is not free of subjectivity. As an alternative, new classification schemes have been proposed, for example, the ATLAS-3D project, in which galaxies are classified according to their kinematical properties (Cappellari et al. 2011). Another problem associated with visual classification is the time needed to classify large samples such as the Sloan Digital Sky Survey (SDSS; Abazajian et al. 2003). Nevertheless, the Galaxy Zoo project (Lintott et al. (2008)) has collected simple morphological classifications of nearly 900 000 galaxies drawn from the Sloan Digital Sky Survey, contributed by hundreds of thousands of volunteers (Lintott et al. 2011). Another way to classify galaxies is to use automatic classifications. The automatic classifications are divided in two broad groups: parametric and non-parametric. Parametric classifications reproduce galaxy measurements using parametric laws, such as the surface brightness distribution (e.g. Morgan & Mayall 1957). Non-parametric galaxy classifications are based on the measurements of a set of galaxy parameters that are correlated with the Hubble sequence. Several galaxy parameters have been used for decades for galaxy classification; for example, galaxy colors (Strateva et al. 2001 and references therein) and light concentration indices (e.g.Gavazzi et al. 1990), or using algorithms that combine several parameters in three dimensions (e.g. Huertas-

Company et al. 2011).

1.2 Galaxy formation models

1.2.1 Monolithic collapse

The first working picture for the formation of galaxies was proposed by Eggen et al. (1962), in which disc galaxies form through a monolithic collapse of a large gas cloud. As the cloud collapses, the gas settles down into a rotating disc. The implications for galaxies in general were later envisaged by Sandage et al. (1970). The next paragraph presents a summarized account of this scenario.

A protogalaxy starts to collapse out of intergalactic material. It is either already rotating or it acquires its angular momentum from the torques exerted by nearby condensations. As the material falls together, condensations are formed that will later become globular cluster and globular cluster-like stars. The collapse of the galaxy in the radial direction is eventually stopped by rotation, though it continues in the vertical-direction giving rise to a thin disc. With the increased density, the rate of star formation increases. In their evolution, the first-generation stars enrich the remaining gas with heavy elements formed in their interiors, with the result that later generations, formed from this same material, show smaller ultraviolet excess. The gas, which must have become hot, radiates away much of the energy of the collapse. At first, the gas follows the orbits of the stars that were formed from it, but the gas and the stars become separated near perigalacticum, after which, relieved of its extra energy by collisions with other gas clouds, the gas settles into circular orbits appropriate to its angular momentum and continues to produce later generations of stars that also move in nearly circular orbits. The first-generation stars, on the other hand, continue in the highly eccentric orbits produced by the original collapse. This scenario predicts a vertical metallicity gradient. It also predicts that the metallicity is lower for stars in more eccentric orbits.

1.2.2 Hierarchical galaxy formation

A few years later, the wide acceptance of the concept of hierarchical assembly and the discovery that galaxies are embedded in extended massive halos of dark matter, led to the two-stage galaxy formation model of White & Rees (1978). This model proposes that approximately 80% of the material in the Universe is not in gas or luminous stars but rather in some “dark” form that was condensed at an early epoch into small “dark” objects, and that, irrespective of their nature, these objects must subsequently have undergone hierarchical clustering. As each stage of the hierarchy forms and collapses, gravitational effects wipe out its substructure, leading to a self-similar distribution of bound masses.

This model, in contrast to the monolithic collapse, implies that the luminous inner part of galaxies cannot have formed by purely dissipationless clustering. Rather, it most probably condensed from residual gas lying in the transient potential wells provided by the dark matter.

White & Frenk (1991) devised models to calculate the characteristics of the galaxy population in a universe where galaxy formation occurs gravitationally, as originally envisaged by White & Rees (1978), where gas cools, condenses, and forms stars within a hierarchical clustering distribution of dark matter. The method developed allowed them to calculate a number of properties of galaxies, such as star formation rates, luminosity functions for galaxies and for galaxy aggregates, and predict a systematic relation between their properties (i.e, luminosity, circular velocity, metallicity, gas content, and total or stellar mass-to-light ratio). They found that assembly may well occur continuously rather than in a well-defined event, suggesting that discs must form within a halo which has already reached equilibrium and form stars in a somewhat longer time scale than that of halo collapse and gaseous dissipation. In addition, discs must have avoided major mergers since the formation of most of its stars. Systems where stars formed primarily before or during the collapse are expected to be seen as ellipticals or as the bulge of spirals. Discs form around bulges from weakly bound residual gas or from newly accreted material, a process which can occur only if the galaxy's halo remains relatively undisturbed and continues to gain mass. Small galaxies tend to form first.

1.3 Mergers

Until the 1970s, most astronomers believed that collisions between galaxies seldom occur, except in high-density regions such as clusters. It was not until the restricted three-body simulations by Toomre & Toomre (1972) that many of the morphologically peculiar galaxies started to be accounted as the result of tidal interactions, and the question about the connection between galaxy collision and nuclear activity in galaxies arose. Since then, there have been increasingly strong theoretical motivations and observational indications that collisions are one of the most important processes in galaxy evolution.

Mergers are usually classified according to the mass ratio between the involved galaxies as:

- **Major merger**: a mass ratio less or equal than 4:1.
- **Minor merger**: a mass ratio bigger than 10:1.

- **Intermediate merger**: a mass ratio intermediate between major and minor merger.

Mergers are also 'classified' by their gas richness as:

- **Wet merger**: merger between gas-rich or blue galaxies.
- **Dry merger**: It take place between gas-poor or red galaxies.

Major mergers, in which the merging galaxies have similar masses, lead to a merger remnant that looks quite different from either of its progenitors due to the violent change in the gravitational field (e.g. van Albada 1982; Kennicutt et al. 1987; Di Matteo et al. 2009; Prieto et al. 2012). In contrast, minor mergers, in which one of the merging galaxies is much smaller than the other, produces only small changes in the larger galaxy (e.g. Quinn et al. 1993; Walker et al. 1996; Naab et al. 2009; Eliche-Moral et al. 2012).

1.3.1 Mergers of disc galaxies

Many present-day galaxies owe their properties to the violent change in gravitational field mentioned above. Because mergers scramble discs and induce dissipation and starbursts, they are thought to produce classical bulges and elliptical galaxies (Kormendy & Kennicutt 2004).

Binary mergers of disc galaxies have been proven to be very good candidates for being the main formation mechanism for intermediate mass ellipticals (e.g. Naab & Burkert 2003; Bournaud et al. 2005; Cox et al. 2006; Hopkins et al. 2008a), whether by dissipationless major mergers (e.g. Hernquist 1993; González-García & Balcells 2005; Boylan-Kolchin et al. 2005; Cox et al. 2006) or by gas-rich mergers (e.g Cox et al. 2006; Bournaud et al. 2011). Another consequence of gas-rich mergers is induced star formation (e.g. Hopkins et al. 2005) and nuclear (quasar) activity (e.g. Hopkins et al. 2005; Li et al. 2007; Ivison et al. 2012).

On the other hand, minor mergers are a good mechanism to enhance secular processes such as the dynamical heating of the stellar disc (Hopkins et al. 2008b, Tapia et al. 2010a,b), which can lead to the formation of a new disc or reinvigorate an existing one, generating the so-called thick disc (Villalobos & Helmi 2008, 2009; Villalobos et al. 2010; Di Matteo et al. 2011).

This kind of mergers may also form bars and tidal spirals, including both internal waves and extended tidal tails (Combes 2009), and rotationally-supported stellar inner disc and rings (Athanassoula et al. 1997; Eliche-Moral et al. 2011) and contribute to the bulge growth (Aguerri et al. 2001; Eliche-Moral et al. 2005, 2006).

Merging processes induce an increasing difference in the rotational support of the old and young stellar components (Qu et al. 2011).

Spheroids may also be formed through both major mergers and minor mergers (Combes 2009). Bournaud & Combes (2004) showed that several successive mergers in the range of mass ratios 10:1 to 4:1 can form elliptical galaxies with larger efficiency than single major mergers.

A drawback of this scenario, given the high merging rates characteristic of hierarchical scenarios such as ΛCDM, is the existence of bulge-less and pure disc galaxies (van den Bosch 2001; Abadi et al. 2003a; D'Onghia & Burkert 2004; Kormendy & Fisher 2005). This is especially critical in bulge-less disc galaxies with high rotation velocities: assembling the massive halos of such galaxies requires many mergers, which should lead to the growth of a bulge.

1.3.2 Mergers of elliptical galaxies

Mergers between early-type galaxies can generate a more massive elliptical galaxy (González-García & Balcells 2005; Naab et al. 2006; González-García et al. 2009) and the widening of the Fundamental Plane (González-García & van Albada 2003).

Mergers between unequal elliptical galaxies are able to produce counterrotating cores due to the deposition of orbital angular momentum in the core of the remnant (Balcells & Quinn 1990). From a kinematical point of view of early-type galaxies, the dissipationless mergers have been suggested to play a major role in the evolution and formation of the slowest rotators (Emsellem et al. 2007).

The observations of faint shells or ripples around the elliptical galaxies, discovered by Malin and Carter (Malin & Carter 1980, 1983) were shown to be tidal debris formed by the collision of an elliptical galaxy and a disc galaxy by Quinn (1984).

1.4 Merger rate measurements

The relevance of merging for the cosmological growth and transformation of galaxies depends on the number of mergers a galaxy undergoes throughout its life. It is usually quantified by means of the merger rate, defined as the mean number of mergers a typical galaxy suffers per Gyr.

Since the galaxy merger rate cannot be directly measured from observations, it is inferred from the merger fraction, defined as the fraction of galaxies undergoing a merger in a given redshift interval. The galaxy merger fraction is a direct observational quantity. Merger fractions may be estimated from statistics of close pairs (e.g., Patton et al. 2000), or morphological criteria (e.g., Conselice 2003; López-Sanjuan et al. 2009a). It is usually parametrized with a relation of the type $(1+z)^n$. The merger rate is derived form the merger fraction by assuming a typical merger duration, which is estimated from merger simulations and simplified models (Mihos 1995; Conselice 2006). Hence, the merger rate between $z=0$ and $z=1$ is found to be lower in more massive galaxies (López-Sanjuan et al. 2009b). López-Sanjuan et al. (2012) have claimed that massive early-type galaxies have undergone 0.89 mergers (0.43 major and 0.46 minor) since $z\sim 1$, leading to a mass growth of $\sim 30\%$ (75%/25% due to major/minor mergers), that merging is the main contributor to the size evolution of massive ETGs at $z\leq 1$, accounting for $\sim 50-75\%$ of that evolution in the last 8 Gyr. Nearly half of the evolution due to mergers is related to minor (mass ratio $< 1/4$) events.

1.5 Present challenges

Mergers are the major processes to explain the formation of long-lived small-scale stellar structures: massive bound globular clusters, tidal tails and streams, decoupled nuclear cores, etc., (Bournaud 2009). Models successfully explain the structure build-up of the cold dark matter component of the Universe (Springel et al. 2005a). However, they have difficulties at explaining the evolution of the baryonic component, even with modeling that incorporates star formation, active galactic nuclei and supernova feedback, and the multiphase nature of the interstellar medium (e.g., De Lucia & Blaizot 2007). Although there has been recent progress (e. g., Hopkins et al. 2010b; Oser et al. 2010) there are still open questions about the role of galaxy mergers in the formation of today's galaxies. Next, we will focus on two problems: size evolution of massive elliptical galaxies, and disc thickening in disc galaxies.

1.5.1 Size evolution of massive elliptical galaxies

Observations of massive galaxies ($M \gtrsim 10^{11}\ M_{\odot}$) have revealed that they were extremely compact at high redshift (Daddi et al. 2005; Trujillo et al. 2007; van Dokkum et al. 2008; Pérez-González et al. 2008; Buitrago et al. 2008). However, at $z\sim 0$ such galaxies are very uncommon (Bernardi et al. 2006; Trujillo et al. 2009; Ferré-Mateu et al. 2012), implying that the present-day early-type galaxies were not fully assembled at $z\approx 2$ and underwent significant structural evolution until the present day, more compact than present-day equal-mass systems. This size evolution is not consistent with a scenario whereby massive galaxies were fully assembled in the early Universe, and have subsequently evolved passively until today (i.e. a pure monolithic scenario). A more compatible scenario is one where a fraction of the most massive galaxies possibly formed in a short monolithic-like collapse and then evolved through major gas-rich or gas-poor merging (Trujillo et al. 2007).

Figure 1.3 illustrate the observed size evolution of the most massive elliptical galaxies located $\sim$ 710 arcmin^2 in the Extended Groth Strip (EGS). We see that since redshift $\sim$1.5 spheroid-like galaxies (Sersic index $n > 2.5$) with masses larger than $10^{11} h_{70}^{-2}$ $M_\odot$ have increase their sizes a factor of $\sim$4.

The contribution of major and minor mergers to the mass growth and size evolution of massive early-type galaxies depends of the merger rates of major and minor mergers. However, the actual predicted rates of major mergers are not high enough to explain the size evolution (López-Sanjuan et al. 2012).

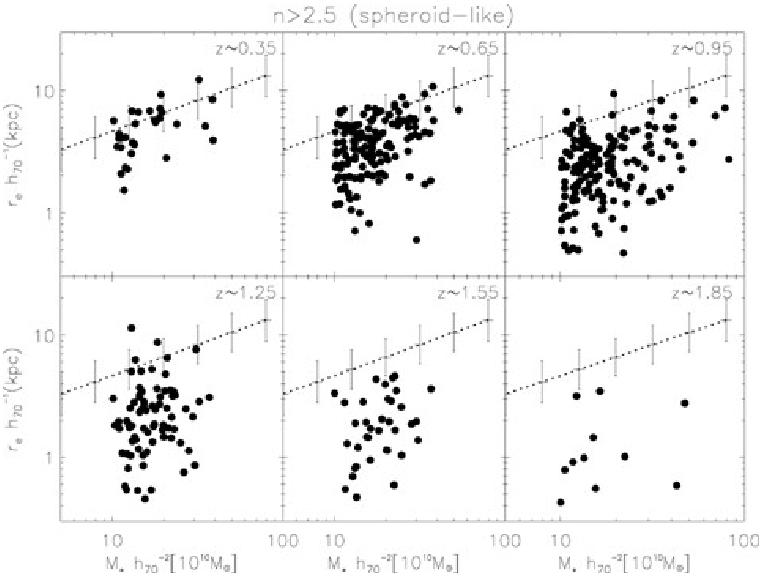

FIGURE 1.3— Stellar mass size distribution of the spheroid-like galaxies from Trujillo et al. (2007). The points correspond to their sample of 831 galaxies with masses larger than $10^{11} h_{70}^{-2}$ $M_\odot$ located over $\sim$ 710 arcmin^2 in the Extended Groth Strip (EGS). Over-plotted are the mean and dispersion of the distribution of the Sérsic half-light radius of the SDSS early-type ($n > 2.5$) galaxies as a function of the stellar mass. The mean size relative error is < 30 per cent. Uncertainties in the stellar mass are $\sim$ 0.2 dex.

1.5.2 Disc thickening in disc galaxies

The discs of disc galaxies contain a substantial fraction of their baryonic matter and angular momentum, and much of the evolutionary activity in these galaxies, such as the formation of stars, spiral arms, bars and rings, and the various forms of secular evolution, take place in their discs. Thick discs are common in disc galaxies, but their formation is not yet understood (van der Kruit & Freeman 2011). Among the various mechanisms, accretion of satellites (e.g., Villalobos & Helmi 2008, 2009; Di Matteo et al. 2011), stars migrating from the inner disc and significantly thickening the disc when it is seen edge-on (e.g., Minchev et al. 2012), or small amounts of star formation in the warp structure (e.g., Roškar et al. 2010) have been proposed.

Recent observations that thick discs are on average more massive than previously reported (Comerón et al. 2011; Knapen et al. 2012) and the improvements in the detailed structural decomposition of galaxy images (Peng et al. 2002; Méndez-Abreu et al. 2008; Laurikainen et al. 2010), have reinvigorated the debate about the relevance of secular evolution and the satellite perturbations, which according to Bird et al. (2012), appear to be a mechanism for inducing radial migration that can operate in concert with migration induced by bars and spiral structures.

1.6 N-body simulations

N-body simulations use computers to calculate the dynamical evolution of a system of particles, usually under the influence of physical forces, such as gravity. They are widely used tools in astrophysics, with applications from few-body or solar system-like systems, all the way up to galactic and cosmological scales (Hut 2008).

The history of N-body simulations started with a pioneering attempt by Holmberg (1941), who followed the evolution of a 37 particle system, where the force was calculated using lightbulbs and galvanometers (taking advantage of the same r^2 scaling of electromagnetic and gravitational interactions). Computer simulations started in the early sixties using up to 100 particles (e.g. see von Hoerner 1960 and Aarseth 1963) and had their full bloom in the eighties with the development of fast and efficient algorithms to deal with collisionless systems, such as particle-mesh codes (see Hockney & Eastwood 1988 and references therein) and the tree method (Barnes & Hut 1986).

1.6.1 Relevant dynamics

The underlying dynamics relevant to the astrophysical context of a system of N particles interacting gravitationally is typically Newton's law plus, if required, an external potential field. The force $\vec{F_i}$ acting on particle i of mass m_i is:

$$\vec{F_i} = -\sum_{j \neq i} G m_i m_j \frac{\vec{r_i} - \vec{r_j}}{\mid \vec{r_i} - \vec{r_j} \mid^3} - \vec{\nabla} \cdot \Phi_{\text{ext}}(\vec{r_i}) \tag{1.1}$$

where $G = 6.673 \cdot 10^{-11}$ m^{3}kg^{-1}s^{-2} is the gravitational constant, and Φ_{ext} is the external potential. The problem is thus a set of non-linear second order ordinary differential equations relating the acceleration $\partial^2 \vec{r_i}/\partial^2 t = \vec{F_i}/m_i$ with the position of all the particles in the system.

The gravitational force (equation 1.2) presents a singularity when the distance between two particles approaches 0, which can lead to arbitrarily large relative velocities. The singularity may be avoided by introducing a softening length (ϵ) in equation (1.2) (e.g. see Aarseth 1963), i.e. by modifying the gravitational interaction at small scales. For example:

$$\vec{F_i} = -\sum_{j \neq i} G \frac{m_i m_j}{(\mid \vec{r_i} - \vec{r_j} \mid^2 - \epsilon^2)^{3/2}} \tag{1.2}$$

where $\epsilon > 0$ is the softening length, a typical distance below which the gravitational interaction is not allowed to grow. To minimize the force errors and the global impact of the softening for distances larger than ϵ, finite size kernels that ensure continuous derivatives of the force may be employed (e.g., see Dehnen 2001). This strategy effectively suppresses binary formation and strong gravitational interactions, but at the price of altering the dynamics of the system.

1.6.2 Numerical methods

Direct N-body method

The direct N-body method does not introduce approximations in the solution of the equations of motion and thus delivers the highest accuracy at the price of the longest computation time, of the order of $O(N2)$ per time step. A state-of-the-art, publicly available, serial direct N-body integrator is Aarseth's NBODY6 (Aarseth 1985, 1999; Hemsendorf et al. 1997; Nitadori & Aarseth 2012). Direct N-body simulations are used to study the dynamical evolution of star clusters.

Particle mesh method

In this case, the gravitational potential of the system is constructed over a grid starting from the density field and by solving the associated Poisson equation. Particles do not interact directly between each other but only through a mean field. The method essentially softens the gravitational interactions at small scales, that is to say, below the cell length. The density field is constructed using a kernel to split the mass of the particles to the grid cells around the particle position. The deriving force, defined on the grid, is then assigned back to the particles using the same kernel employed for the density field construction, in order to avoid spurious self forces. Since this method is limited by the mesh size, a smaller mesh or some other technique, such as adaptive grid the so-called AMR method, as are the codes MASCLET (Mesh Adaptive Scheme for CosmologicaL structurE evoluTion; Quilis 2004) and Enzo (Eulerian block-structured adaptive mesh refinement cosmology code; Bryan & Norman 1998; O'Shea et al. 2004; Norman et al. 2007), or the expansion of the density and potential of the system in terms of a basis of orthogonal eigenfunctions (Hernquist & Ostriker 1992), is used to compute the small-scale forces.

Fast multipole method

The Fast Multipole Method (Greengard & Rokhlin 1987) uses a multipole expansion to compute the force from a distant source cell within a sink cell. One advantage of the fast multipole method is that the symmetry in the treatment of sink and source cells with respect to the multipole expansion can guarantee an exact conservation of the momentum. Recent successful implementations of fast multipole codes or hybrids with tree code scheme include Dehnen's Cartesian expansion scheme, the GyrfalcON code (GalaxY simulatoR using falcON; Dehnen 2000) and PKDGRAV (Parallel K-D tree GRAVity code; Stadel 2001).

Tree method

The tree code method (Barnes & Hut 1986) provides a fast, general integrator for collisionless systems. The volume is usually divided up into cubic cells in an oc-tree, so that only particles from nearby cells need to be treated individually, and particles in distant cells can be treated as a single large particle centered at its center of mass (or as a low-order multipole expansion). In fact, in a tree code, strong interactions at small scale are typically softened (however, see McMillan & Aarseth 1993). The resulting computation time scales as $O(N\log(N))$, though the approximations introduce small force errors. TREESPH code (A unification of SPH with the hierarchical TREE method; Hernquist & Katz

1989) is an example of the implementation of this method. For a schematic illustration of this method see Figure 1.4.

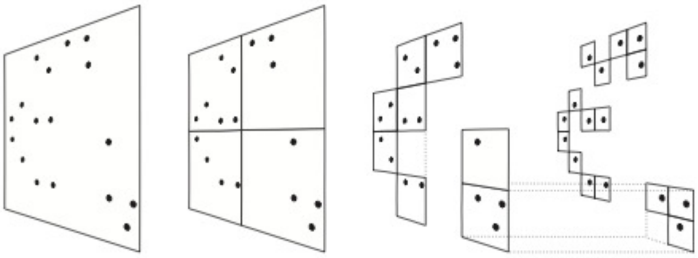

FIGURE 1.4— Schematic illustration of the Barnes & Hut oc-tree Barnes & Hut 1986 in two dimensions. The particles are first enclosed in a square (root node). This square is then iteratively subdivided in four squares of half the size, until exactly one particle is left in each square (leaves of the tree). In the resulting tree structure, each square can be progenitor of up to four siblings and the empty squares need not to be stored. Source: Springel et al. (2001).

P3M and PM-Tree codes

In order to increase the force resolution of particle mesh codes it has been proposed to couple a mean field description on large scales with a direct, softened, treatment of the gravitational interactions on distances of the order of or below a few grid spacings (e.g. see Springel et al. 2005b). This method is called P3M: Particle-Particle-Particle-Mesh, and efficiently increases the dynamic range of the parent PM algorithm. However, in presence of strong clustering, a large number of particles will interact directly between each other, significantly slowing down the computation to $O(N2)$. This problem can be solved by using adaptive meshes, whereby the spatial resolution is refined in regions of high density. Adaptive P3M codes have a computational cost that scales as $O(N\log(N))$, like tree code's. Finally, another possibility is to resort to a tree code for the short range force evaluation leading to a hybrid PM-Tree scheme. These methods are generally extremely well suited for cosmological simulations e.g. GADGET (GAlaxies with Dark matter and Gas intEracT; Springel et al. 2001; Springel 2005) and DEVA codes (a multistep AP3M-like SPH; Serna et al. 2003).

GADGET-2 Computes gravitational forces with a hierarchical tree algorithm (optionally in combination with a particle-mesh scheme for long-range gravitational forces) and represents fluids by means of smoothed particle hydrodynamics (SPH). The code can be used for studies of isolated systems, or for simulations that include the cosmological expansion of space, both with or without periodic boundary conditions. In all these types of simulations, GADGET follows the evolution of a self-gravitating collisionless N-body system, and allows gas dynamics to be optionally included. Both the force computation and the time stepping of GADGET are fully adaptive, with a dynamic range which is, in principle, unlimited.

1.6.3 Software environments

In addition to the availability of stand-alone codes, several software environments have been created that contain various tools to set up initial conditions, run simulations, and analyze and visualize their results. For example, NEMO (an extendible Stellar Dynamics Toolbox) and Starlab (software package for simulating the evolution of dense stellar systems and analyzing the resultant data).

1.6.4 Specialised hardware methods

An alternative approach to increase the efficiency of numerical resolution of the N-body problem is to optimize the hardware. The basic idea is to optimize a hardware pipeline to compute $(r_i - r_j) / \mid \vec{r_i} - \vec{r_j} \mid^3$. This special purpose hardware can then be interfaced with a general purpose computer, which carries out all the other numerical operations required to solve the equations of motion.

Another recent promising hardware development is the possibility to use Graphic Cards (GPUs) to carry out the central processing unit (CPU) intensive force evaluation. The performance of current generation of GPUs appears to be superior (in terms of Flops/$ ratio). At present, two of the top ten world's fastest computer systems, Tianhe-1A[1] and Titan[2], are equipped with GPUs.

1.7 Motivation of the thesis

Minor mergers are more frequent than major mergers. Therefore, it is of great interest to study their role in galaxy evolution.

Specifically, because they are good candidates to explain size growth in ellipticals, we believe it is important to quantify how much size growth is due to minor mergers. Realistic merger rates are required for the results to be

---

[1] Supercomputer capable of a maximum range of 2.566 petaFLOPS. Located at the National Supercomputing Center in Tianjin, China. It is now equipped with 14,336 Xeon X5670 processors and 7,168 Nvidia Tesla M2050 general purpose GPUs.

[2] Titan is a 20 petaflop supercomputer developed by Cray, Inc. and the Oak Ridge National Laboratory. It is the transformation of the Jaguar supercomputer at Oak Ridge, to use GPUs in addition to CPUs.

meaningful. While this can be accomplished including gas dynamics and star formation, N-body models without these two components are more robust and provide a good starting point.

In addition, because disk thickening via minor mergers is a gravitational problem, it is interesting to quantify disc thickening using models with sufficient particle numbers to minimize discreteness effects.

2

Objectives

The objective of this thesis is to shed light on the following questions:

- In a Λ cold dark matter (ΛCMD) universe, can cosmological dry merger histories generate the observed size evolution of massive elliptical galaxies? What is the corresponding change in the velocity dispersion of the galaxy?

- Assuming an initial metallicity gradient in the progenitor, and a simple chemical model with no star formation, what is the evolution of the metallicity profile as a consequence of the merger history? What are the ranges in metallicity gradients that the merger history predicts for $z = 0$ galaxies?

- In the framework of thick disc formation due to the accretion of satellites by a disc galaxy, which is the predominant cause underlying the observed thickening of the disc? Is it the disc material that has been heated or is it satellite material that is deposited onto the disc?

These three questions will be addressed in the next chapters.

3

Size evolution of elliptical galaxies in a λCDM universe

> *A good simulation, be it a religious myth or scientific theory,*
> *gives us a sense of mastery over experience.*
> *To represent something symbolically,*
> *as we do when we speak or write, is somehow to capture it,*
> *thus making it one's own.*
> *But with this appropriation comes the realization*
> *that we have denied the immediacy of reality*
> *and that in creating a substitute*
> *we have but spun another thread in the web of our grand illusion.*
> Heinz Rudolf Pagels
> The Dreams of Reason: The Computer
> and the Rise of the Sciences of Complexity (1988)

In this chapter we study the size evolution of massive elliptical galaxies driven by the accretion of satellites from $z = 2$ to the present. To understand the details of this growth we resimulate at high spatial resolution the merger histories of 8 elliptical galaxies, which we have obtained from hydrodynamical cosmological simulations. Realistic satellite densities are ensured by using observationally-derived mass-size relations. We find that the median growth is a factor 4 in size and a factor 2 in mass from z=2 to z=0, with a small increase of the velocity dispersion.

3.1 Introduction

Observations have revealed that massive galaxies ($M \gtrsim 10^{11}\ M_\odot$) at high redshift were more compact, showing smaller effective radius and consequently higher densities than present-day massive galaxies (Daddi et al. 2005, Trujillo et al. 2006, 2007; van Dokkum et al. 2008; Buitrago et al. 2008). About $\sim$

60% of all compact massive galaxies are red and are evolving passively (Pérez-González et al. 2008), suggesting that a red sequence may already be in place before $z = 2$ (Kriek et al. 2008). These "red and dead" galaxies show a typical size of $r_e \sim 1$ kpc (Buitrago et al. 2008) and velocity dispersion ranging from $\sim 280~\mathrm{km\,s^{-1}}$ to $\sim 540~\mathrm{km\,s^{-1}}$ (van Dokkum et al. 2010). If massive compact galaxies evolve at constant mass from z to the present, from a naïve application of the virial theorem, we would expect velocity dispersions twice as high at $z = 2$ than at $z = 0$, or about $\sigma \sim 500~\mathrm{km\,s^{-1}}$. In contrast, if galaxies have grown inside-out, then the increase of the mass in the outer parts may have occurred with little or no increase in the central velocity dispersion. There is only one measure of $\sigma \sim 510~\mathrm{km\,s^{-1}}$ (van Dokkum et al. 2009), the majority of measurements lying around $\sigma \sim 200 - 250\mathrm{km\,s^{-1}}$ (Cenarro & Trujillo 2009; Martinez-Manso et al. 2011). Such galaxies are very uncommon in the nearby universe (Bernardi et al. 2006; Trujillo et al. 2009; Ferré-Mateu et al. 2012), which means that the present-day early-type galaxies were not fully assembled at $z \approx 2$ and underwent significant structural evolution until the present day. Thus, it has been suggested that this entire population of compact, high-redshift red galaxies may be the progenitors of the most massive ellipticals and brightest cluster galaxies today (Hopkins et al. 2009b; Bezanson et al. 2009).

To explain such size evolution, many explanations have been put forward. The monolithic collapse scenario (Eggen et al. 1962) envisioned that all spheroidal galaxies formed very early via a rapid collapse of the gas at high redshift and that their observed properties are the consequence of the passive fading of their stellar populations, which has been ruled out (van Dokkum et al. 2008). In the framework of the hierarchical clustering of galaxy formation (White & Frenk 1991) we have a fading merger-induced starburst (Khochfar & Silk 2006; Cimatti et al. 2008; Hopkins et al. 2009b). Due to gas-rich mergers of disc galaxies (Scarlata et al. 2007). Also, Fan et al. (2008, 2010) have proposed that the quasar activity removes large amounts of gas from central galaxy regions, triggering a puffing up of the stellar component at constant stellar mass. However, in the light of recent observations (van Dokkum et al. 2010; Trujillo et al. 2011; Cooper et al. 2012) and the observed mild evolution in the velocity dispersion (e.g. Cenarro & Trujillo 2009), the later major or minor "dry" mergers with less dense galaxies seems the most promising mechanism to turn a compact high-z galaxy into an early-type present-day galaxy (Naab et al. 2007; Kaviraj et al. 2009; Hopkins et al. 2010a; Oser et al. 2012; Whitaker et al. 2012; Hilz et al. 2012). Minor mergers are particularly efficient in reducing the effective stellar densities, mildly reducing the velocity dispersions and rapidly increasing the sizes, building up stellar envelopes (Naab et al. 2009; Bezanson et al. 2009; Oser et al. 2010.

Recently, Oser et al. (2012) analyzing a set 40 re-simulations of individual halos found that the dominant accretion mode is the stellar minor mergers with typical galaxy mass-ratios of $\sim$ 5:1. Nevertheless, Nipoti et al. (2009) based on a set of simulations found that the dry mergers do not decrease the galaxy stellar-mass surface enough to explain the observed size evolution and also introduced substantial scatter in the scaling relations. Furthermore, Cimatti et al. (2012) by analyzing a large sample of early-type galaxies (ETGs) at $0 < z < 3$ and comparing it with a model of pure dissipationless (dry) merging in the ΛCDM framework have found that the pure dry merging ΛCDM model is marginally consistent with the average size evolution at $0 < z < 1.7$ but predicts descendants too compact for $z > 2$ progenitor ETGs. A similar conclusion has been reached by Newman et al. 2012, who estimated the minimum growth rate necessary to explain the declining abundance of compact galaxies and found that mergers may explain most of the size evolution observed at $z \lesssim 1$ if a relatively short merger timescale is assumed, but the rapid growth seen at higher redshift likely requires additional physical processes. Moreover, it remains unclear whether galaxy formation simulations in the context of the λCDM model can reproduce not only the existence of extremely compact galaxies at hight redshfit but also the fact that a large spread in the properties of massive galaxies exists at low and hight redshift (Kaufmann et al. 2012).

3.2 Motivation

Although there are many studies about the contribution of the minor mergers to the size evolution of massive galaxies, it remains unclear whether this physical process in a fully cosmological context is able to generate the observed properties of the present-day massive elliptical galaxies. To shed light on the topic we will perform a suite of high-resolution N-body simulations of the merging history of different compact elliptical galaxies, in which the accreted satellites will have orbits and mass ratios directly extracted from hydrodynamical cosmological simulations and the sizes will be realistic by following observational relationships.

For simplicity we limit ourselves to encounters between spheroidal systems. We neglect all dissipative processes, assuming that galaxies grow only by dry mergers. In other words, for given stellar mass growth rates our model will predict the maximum growth in size. In dissipative mergers, stellar mass could grow more than predicted by our models due to the conversion of gas into stars. Nevertheless, this process is believed to have the effect of making galaxies more compact (Hopkins et al. 2010a).

3.3 Models and simulations

3.3.1 Galaxy model

Our galaxy model consists of two components: a live dark matter halo with a Hernquist density profile (Hernquist 1990) and an isotropic Jaffe profile for the luminous matter (Jaffe 1983). The latter is chosen due to the fact that the Jaffe model has a realistic luminosity profile that closely resembles a $R^{1/4}$ profile, the only difference being that it has a steeper gradient at the center ($r < 0.1$). The Hernquist halo is a model which has a rising rotation curve and a rising velocity dispersion, as is observed in the spiral galaxies. This two-component model has been build using the code of Smulders & Balcells (Smulders & Balcells 1995). In this code, the method used to build a galaxy model in equilibrium is starting with a potential-density pair, for which the density profiles are precisely know, then find the distribution function by solving Eddington's formula for the separate densities in the potential generated by the total density using the method of the Gauss-Chebyshev quadrature. In the appendix section A.1 we give more details on how the code works.

Two component Jaffe-Hernquist models

The family of models used on the code are:

$$\begin{aligned}
\rho_{\mathrm{l}}(r) &= M_{\mathrm{l}}\frac{a_{\mathrm{J}}}{4\pi r^2(a_{\mathrm{J}}+r)^2} \\
\rho_{\mathrm{d}}(r) &= M_{\mathrm{d}}\frac{a_H}{2\pi r(r+a_{\mathrm{H}})^3} \\
\phi_{\mathrm{l}}(r) &= M_{\mathrm{l}}G\ln\Big(\frac{r}{r+a_{\mathrm{J}}}\Big) \\
\phi_{\mathrm{d}}(r) &= -M_{\mathrm{d}}G\frac{1}{a_{\mathrm{H}}+r} \\
\rho_{\mathrm{T}}(r) &= \rho_{\mathrm{l}}(r)\,+\,\rho_{\mathrm{d}}(r) \\
\phi_{\mathrm{T}}(r) &= \phi_{\mathrm{l}}(r)\,+\,\phi_{\mathrm{d}}(r)
\end{aligned} \tag{3.1}$$

where ρ_{l} is the density of the luminous matter, which has the same density profile as the Jaffe model (Jaffe 1983), and ρ_{d} is the density of the halo, which has the density profile of a Hernquist model (Hernquist 1990). M_{l} and M_{d} are the total masses of the luminous matter and the halo, respectively. The terms a_{J} y a_{H} are the length scale parameters.

The combined Jaffe-Hernquist model depends on the ratio between M_l and M_d and the ratio between the half-mass radius of the luminous matter and the half-mass radius of the halo, which is determined as follows:

$$r_{\frac{1}{2},\mathrm{l}}/r_{\frac{1}{2},\mathrm{d}} \;=\; \frac{a_\mathrm{J}}{(1+\sqrt{2})a_\mathrm{H}}. \tag{3.2}$$

The cumulative mass of the Jaffe component of the model is equal to

$$M_\mathrm{l}(r) \;=\; M_\mathrm{l}\frac{r}{a_\mathrm{J}+r}. \tag{3.3}$$

The cumulative mass for the Hernquist component of the model is:

$$M_\mathrm{d}(r) \;=\; M_\mathrm{d}\frac{r^2}{(r+a_\mathrm{H})^2}. \tag{3.4}$$

Units

A convenient set of units to match real typical ellipticals galaxies at high-redshift can be set using the equations:

$$V = \left(\frac{GM}{R}\right)^{\frac{1}{2}} \tag{3.5}$$

$$T = \left(\frac{R^3}{GM}\right)^{\frac{1}{2}} \tag{3.6}$$

Taking the following parameter values

$\mathrm{G} = 4.30\times 10^{-6}\frac{\mathrm{kpc}}{\mathrm{M}_\odot}\mathrm{km}^2\mathrm{s}^{-2}$

$\mathbf{M} = 1\times 10^{12}\mathrm{M}_\odot$

$\mathbf{L} = 0.625$ kpc

leads to a velocity and time units of:

$\mathbf{V} = 2622.975\ \mathrm{km\,s^{-1}}$

$\mathbf{T} = 0.238$ Myr

Hence, these will be the set of physical units that we will use throughout this chapter for the gravity constant, mass, length, velocity and time, respectively.

3.3.2 Properties of the galaxy model

In order to construct a typical massive galaxy at high redshift with an effective radius of ~ 1 kpc (Trujillo et al. 2007; Buitrago et al. 2008) and baryon dominated in the inner part, we set a mass ratio between the luminous and the dark matter component of 10 : 1, following González-García et al. (2009) in that baryonic objects are typically embedded in a dark matter extended halo which is 10 times more massive. We set a maximum radius (r_{max}) of 100 units of length, to ensure that the density of our model will slowly go down in the outskirts without artificial cutoffs. The length scale of the dark matter halo was chosen so that the half-mass radius of the dark component and the half-mass radius of the luminous component after the initial relaxation of the model differ in a factor of 5 (initially it was ~ 1, though after the initial relaxation it increased to ~ 2.25), with a parameter $\mathrm{a_H} = 4.828$, which after some tests proved to be the best-suited for our purposes. In those tests we also paid attention to the physical properties of the model, such as the projected circular velocity and the shape of the density profile (see Figure 3.1). We built our galaxy model using $250,000$ particles, a number large enough to properly represent the potential of the galaxy while keeping the simulations affordable in terms of computational time. See Table 3.1 for a summary of the properties of the galaxy model.

Table 3.1— Galaxy model parameters

$\mathrm{M_d/M_l}$ (1)	$\mathrm{r_{l\frac{1}{2}}/r_{h\frac{1}{2}}}$ (2)	$\mathrm{r_{max}}$ (3)	$\mathrm{a_H}$ (4)
10	5	100	4.828

Note.-, *Col. (1)*: Mass ratio, *Col. (2)*: Half-mass-radius ratio, *Col. (3)*: Maximum radius of the model, *Col. (4)*: length scale of the dark matter halo.

In Figure 3.1 we show a number of properties of the initial luminous and dark matter components of the model. We ensured that the density profile and the cumulative mass distribution were dominated by the luminous component in the inner part (labelled "Jaffe" and represented by the dotted line) and by the dark matter component in the outer region (labelled "Hernquist" and represented by the dashed line). Despite the fact that the potential (left-bottom panel) is determined mostly by the potential depth of the dark matter component, the luminous component contributed at the most internal radii. The circular velocity was checked to verify that the sum of the luminous and the dark matter components were approximately flat at all radii, dominated in the inner part by the luminous matter and in the outer part by the dark matter component.

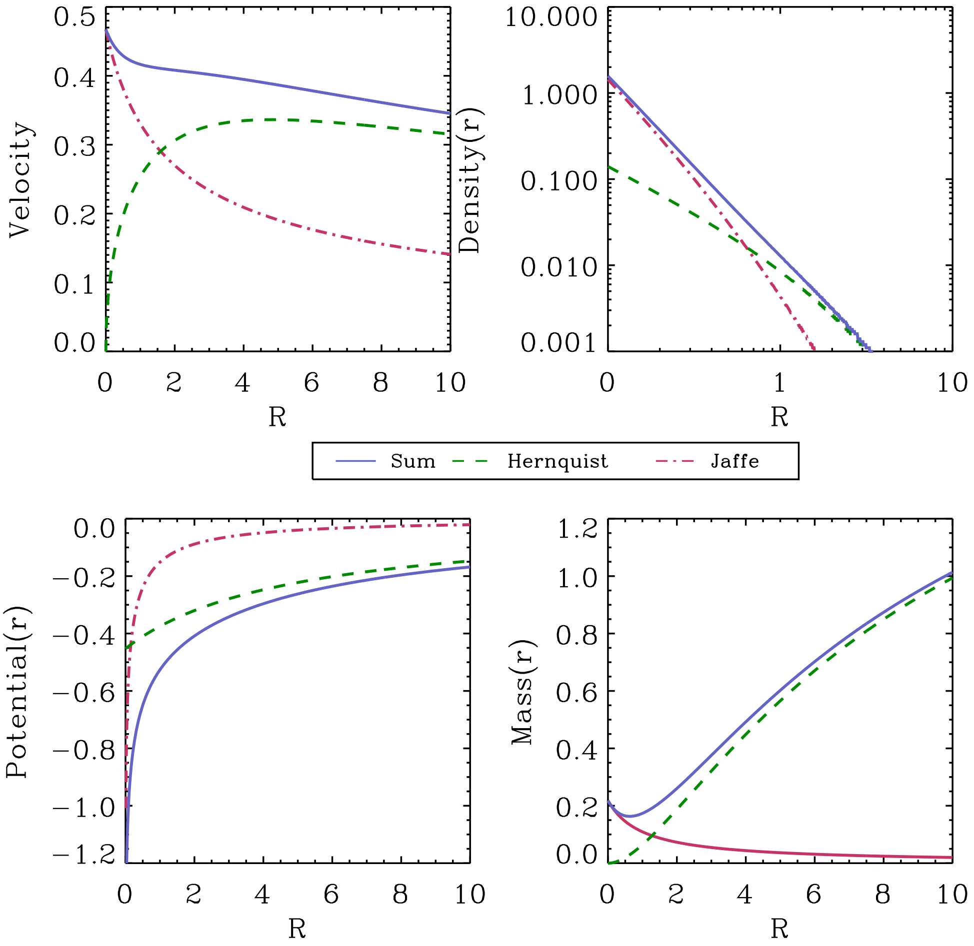

FIGURE 3.1— Physical properties that were taken into account to build the galaxy model. The quantities are expressed in arbitrary units (G=1, V=1, R=1). In all the panels, the dotted line corresponds to the luminous matter (labelled as "Jaffe") and the dash line is the dark matter component ("Hernquist"). The sum of both corresponds to the line labelled as "sum". We ensured that the radial distribution of the density, potential and cumulative mass were at the inner radius dominated by the luminous matter component and in the outer part by the dark matter component with a nearly flat total circular velocity.

In Figure 3.2, we show the surface density profile of the luminous and dark components of the galaxy model after relaxing in isolation for ~ 20 crossing times of the luminous component. We see that luminous matter has a more cuspy profile than the dark matter and that the point at which they intersect is

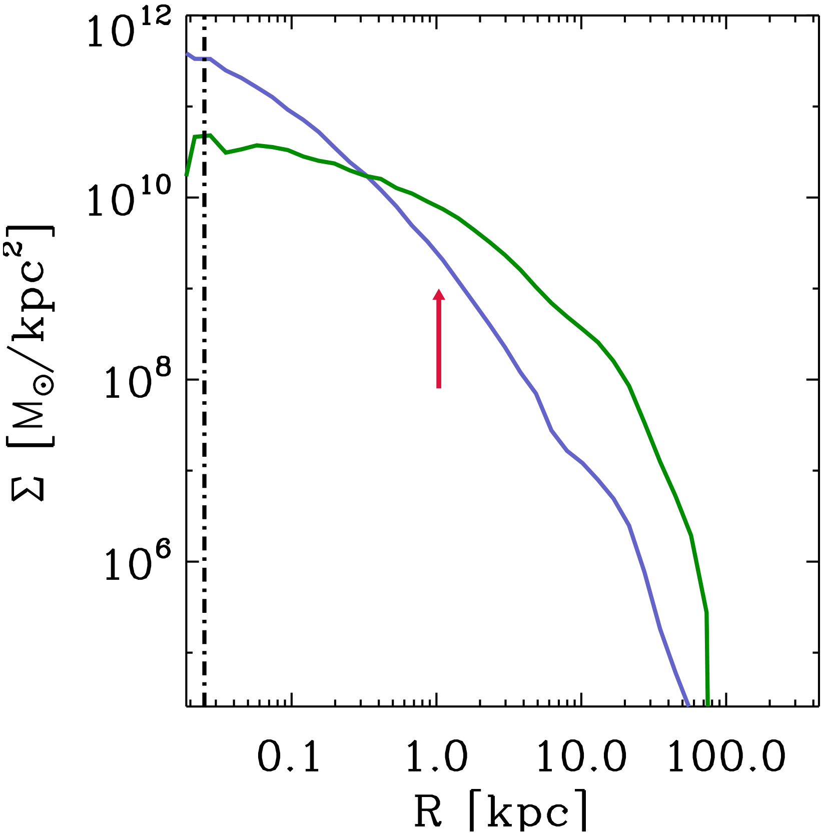

FIGURE 3.2— Stellar surface density profile of one of the progenitor galaxies. The blue line corresponds to the stellar mass and the green line to the dark matter. An arrow indicates the effective radius of the luminous matter. The dot-dashed line represent the softening length of the luminous matter.

at ∼ 0.3 kpc, which is smaller than the effective radius ($r_e = 1.46 \pm 0.006$ kpc) indicated by the red arrow. The galaxy model was built with the Smulders & Balcells code fulfilling the requirements above described.

3.4 Merger trees

Performing a fully cosmological simulation of galaxy evolution with enough resolution to study the dynamic of the baryonic matter requires a huge amount of time and computational resources. To circumvent this difficulty, the *resimulation* technique is widely used. It consists of replacing the formed objects with a model with higher resolution and running again the simulation. Since we are interested in the underlying dynamical processes of the accretion of satellites, it is necessary to have high-resolution galaxies in order to correctly describe the merger process.

3.4.1 Progenitor galaxies

Cosmological simulations

The initial simulations used to extract the initial conditions for the galaxy merger trees are part of the GALFOBS project[1] (Galaxy Formation at Different Epochs and in Different Environments: Comparison with Observational Data). They are N-body + SPH simulations that were performed using an OpenMP parallel version of the gravo-hidrodynamic code DEVA (Serna et al. 2003) and the methods for star formation and cooling described in Martínez-Serrano et al. (2008).

The main GALFOBS simulation was run in a periodic cube of 80 Mpc side, using 512^3 baryonic particles and 512^3 dark matter particles with a gravitational softening of $\epsilon = 2.3$ kpc and a minimum hydrodynamical smoothing length half this value. The applied cosmology was a ΛCDM model with $\Omega_m = 0.295$, $\Omega_b = 0.0476$, $\Omega_\Lambda = 0.705$, $h = 0.694$, an initial power-law index $n = 1$, and $\sigma_8 = 0.852$, values taken from CMB anisotropy data[2] (Dunkley et al. 2009). The mass resolution is $m_{\rm bar} = 2.42 \times 10^7 M_\odot$ and $m_{\rm dm} = 1.26 \times 10^8 M_\odot$ and the star formation parameters set to $\rho_{\rm thres} = 4.79 \times 10^{-25} {\rm gcm}^{-3}$ and $c_* = 0.3$.

In addition to the main run, the GALFOBS project simulated five different sub-volumes of side-length 26 Mpc for which the gravitational forces were derived from the full 80 Mpc box aumented by the hydrodynamical treatment (which is exclusively local) only in the respective sub-box.

The final populations at $M_{\rm star} > 10^{10.5} M_\odot$ have halo occupation statistics consistent with those estimated from other methods and confronted with observations (Guo et al. 2009, 2010; Leauthaud et al. 2011).

In order to construct merger trees, stellar (galactic) objects in each subvolume were identified at all simulation outputs in-between redshifts $z = 2$ and $z = 0$ using the algorithm `SKID` (Weinberg et al. 1997). The final galaxy samples were formed by joining together galaxies identified in each subvolume at each redshift.

The merger trees were constructed by cross-correlating the (stellar or halo) objects in consecutive simulation outputs. For this purpose, the tool `MergerTree` which forms part of the `AHF`[3] halo finder distribution. The latter, identifies all objects in a certain snapshot (in our case the previous redshift z_2) that con-

---

[1] http://www.deisa.eu/science/deci/projects2007-2008//GALFOBS

[2] http://lambda.gsfc.nasa.gov/product/map/current/params/lcdm_sz_lens_run_wmap5_bao_snall_lyapost.cfm

[3] freely available from `http://popia.ft.uam.es/AMIGA`

tribute particles (identified by their unique identification number) to a given object in the snapshot under consideration, z_1. We therefore have a mass-ordered list of progenitors for each and every object at any given redshift z_1 in a previous redshift z_2, with $z_1 < z_2$. Comparing the masses of the most massive progenitors with each other we define a major merger to have happened in between snapshots z_1 and z_2 when there are two progenitors with a mass ratio $\mu \geq 0.25$, regardless of the possible merging stage, i.e. whether the remnant at z_1 is already relaxed or not.

Thus, the merger tree of the largest eight objects with final masses $M_\star \gtrsim 10^{11} M_\odot$ (see Table 3.2) was built, and the initial conditions for the simulations of galaxy-galaxy encounters were computed in the following manner: At redshift z_2, the relative masses of each object is measured and assigned to the progenitors. The center of each object was derived by isolating these objects and calculating the centroid of the most bound particles. The relative separation of the two system is thus calculated and their relative velocities estimated. Finally, this allowed us to calculate the initial conditions of our progenitor systems by assuming keplerian orbits and translating the units to internal units. If the initial separation at redshift z_2 was not enough to ensure that the two systems are not overlapping, the keplerian orbits were traced back to the appropriate separation. The results of these calculations are presented in Table 3.3.

TABLE 3.2— Progenitor galaxies.

ID (1)	r_e [kpc] (2)	σ [kpc] (3)	Stellar Mass $[10^{11} M_\odot]$ (4)
1	1.043 ± 0.004	296.842 ± 4.897	0.833
2	1.039 ± 0.007	274.180 ± 3.221	0.674
3	1.038 ± 0.008	235.990 ± 1.584	0.521
4	1.036 ± 0.008	389.407 ± 7.643	1.380
5	1.045 ± 0.006	319.137 ± 6.439	0.923
6	1.044 ± 0.004	352.161 ± 7.019	1.160
7	1.025 ± 0.006	427.073 ± 8.444	1.670
8	1.025 ± 0.008	486.352 ± 9.962	2.180

Note.-, *Col. (1)*: Identification number of the merger history, *Col. (2)*: Effective radius of the progenitors galaxies, *Col. (3)*: velocity dispersion of the progenitors galaxies, *Col. (4)*: Stellar mass of the progenitors galaxies at $z = 2.5$.

Comparing the galaxy model

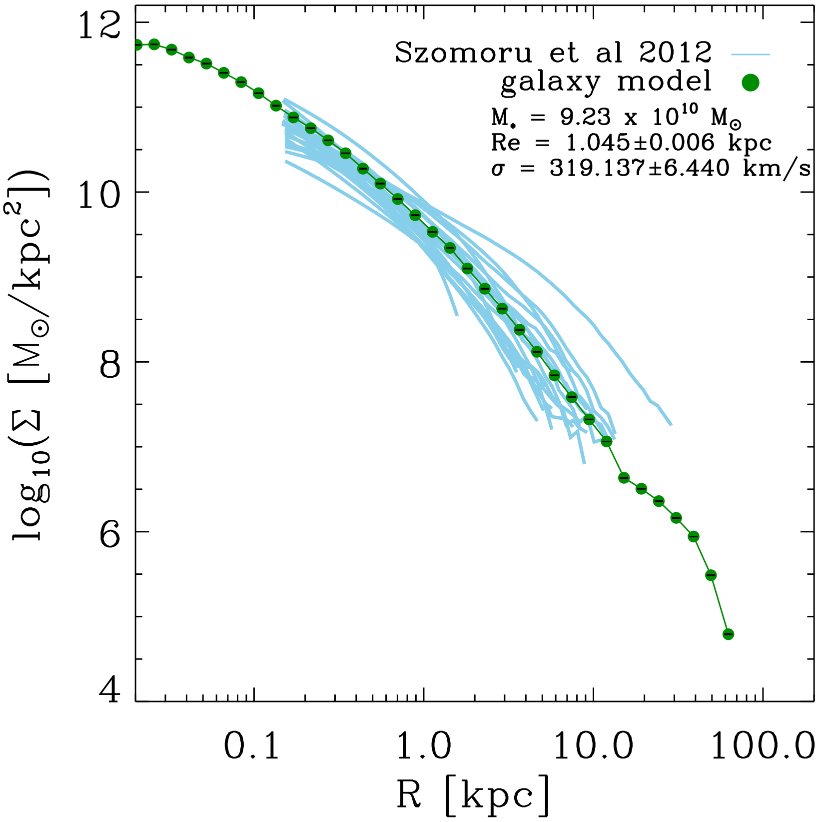

FIGURE 3.3— Stellar surface density profiles. The green circles correspond to one of our progenitor galaxies at $z = 2.5$ and the cyan lines correspond to the sample of high-redshift galaxies from Szomoru et al. (2012).

.

To show that the precursor models resemble an observed galaxy, in Figure 3.3 we compare the surface density profile of one of our galaxy models with high-redshift observed galaxies from the study of Szomoru et al. (2012). The Szomoru et al. (2012) sample consists of 21 quiescent galaxies stellar mass-limited at $z \sim 2$ of the GOODS-South field, that were taken using the deep Hubble Space Telescope Wide Field Camera 3 (HST WFC3) and are part of the CANDELS survey (The Cosmic Assembly Near-infrared Deep Extragalactic Legacy Survey) data-set (Closson Ferguson & CANDELS Collaboration 2011). In the observed range, our galaxy model nicely matches the observations.

In Figure 3.4 we present a summary of the masses and mass ratio as a function of the redshift. The majority of our satellites are in the range of intermediate mergers. A noticeable characteristic of our satellites is that only at $z \sim 1$ we have the mergers with mass ratio $\gtrsim 10:1$.

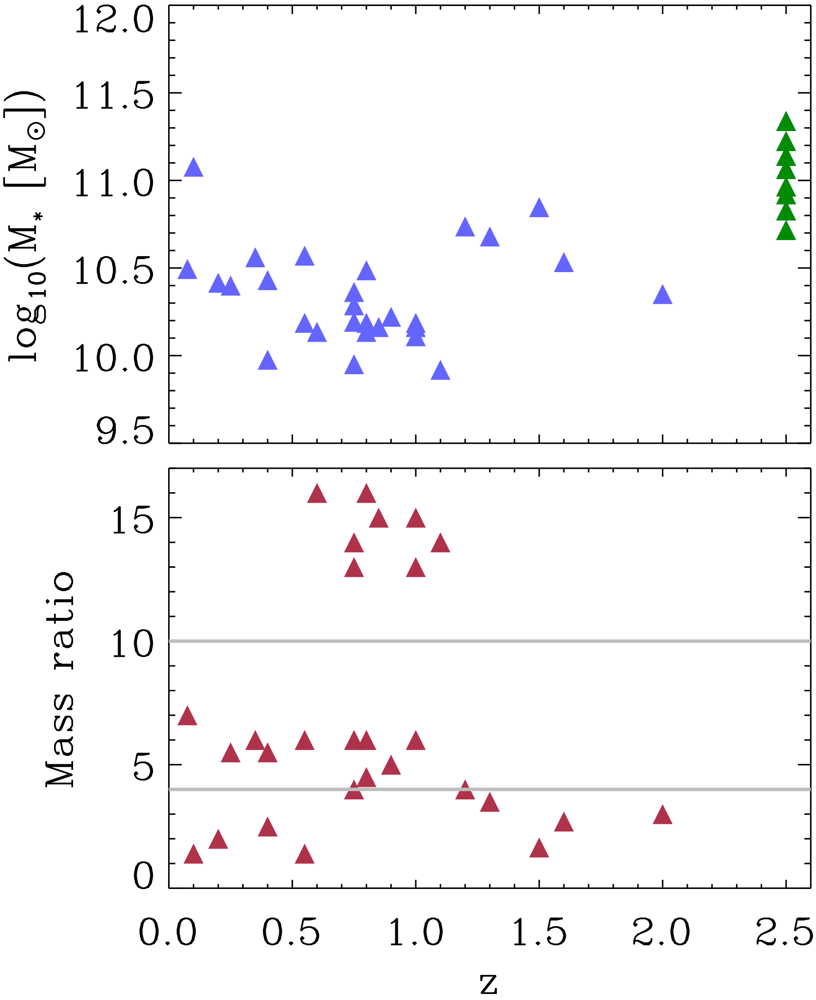

FIGURE 3.4— Upper panel: Range of stellar masses as a function of the redshift for the suite of simulations; the green triangles are the progenitor galaxies and the satellites are shown in blue. Lower panel: Mass ratio between the main galaxy and the satellites as a function of the redshift for the whole sample. The gray lines represent the mass ratios at which a merger is usually classified as major (4:1) and minor (10:1).

3.4.2 Merger histories

Given that the cosmological simulations lack the required resolution to recover the characteristics of the accreted galaxies appart from their mass, we will assume that they have the same shape as the progenitor, i.e. two components with the same parameters (see table 3.1) but with different number of particles in order to always have the same mass in each particle regardless of the galaxy to which it belongs.

3.4.3 Size of the satellites

In an attempt to make the satellites realistic, we have followed observational relationships to set their sizes. These are described below.

Size scaling relations

To set the radius of the satellites we use the size scaling relation given by Shen et al. (2003). In that work a sample of about $140,000$ galaxies from the Sloan Digital Sky Survey (SDSS) was used to study the size distribution of galaxies and its dependence on the luminosity, stellar mass and morphological type. They found that for each type of galaxy, the size distribution at given luminosity (or stellar mass) is well described by a log-normal function characterized by its median $\tilde{R}$ (half-light radius) and dispersion $\sigma_{\ln R}$. If we assume that the half-light radius is the same as the half-mass radius, the Shen et al. (2003) relation of the size distribution as a function of the stellar mass for the early-type galaxies can be written as:

$$\frac{r_{1/2}}{\mathrm{kpc}} = 1.15 \left(\frac{M_\star}{10^{10} M_\odot} \right)^{0.56} \tag{3.7}$$

where $r_{1/2}$ is the half-mass radius and $M_\star$ the stellar mass.

Rest-frame size evolution

To take into account the decrease of the stellar mass-size relation with redshift we use the relationship given by Trujillo et al. (2006). They used very deep near-infrared images of the Hubble Deep Field-South and the MS 1054-03 field in the J_S, H and K_S bands from FIRES (Faint InfraRed Extragalactic Survey; Franx et al. 2000), combined with those from GEMS (Galaxy Evolution from Morphology and SEDs; Rix et al. 2004) and SDSS to study the optical rest-frame size evolution from $z = 0$ to 3. They found that the rest-frame size evolution of the galaxies in the redshift range $0 < z < 3$ at a given luminosity

(L_V>$3.4 \times 10^{10} h_{70}^{-2} L_\odot$) and at given stellar mass ($M_\star \geqslant 3 \times 10^{10} h_{70}^{-2} M_\odot$) for highly concentrated objects (Sersic index $n > 2.5$) has evolved as:

$$r_{1/2}(z) = r_{1/2}(1+z)^{-0.45 \pm 0.10} \tag{3.8}$$

The whole sample, now including the sizes and orbital parameters of the satellites, can be seen in table 3.3.

3.5 Computational aspects

3.5.1 Particles in the merger trees

The eight progenitor galaxies have different masses but the same number of particles. However, each of the satellites in their corresponding merger tree has a specific number in order to have the same individual mass for each luminous and dark matter particle, irrespective of the galaxy from which it comes from.

Since we have some very active merger histories and others with only one or two accretion events, for some 'trees' we finalise with ∼800,000 particles, whereas in others ∼300,000 remain.

3.5.2 Runs

All the simulations were executed using the facilities of the *Red Española de Supercomputación* (RES) throughout the supercomputers LaPalma, Mare Nostrum, Tirant and Atlante, by means of the public version of the GADGET-2 (Springel 2005) code. We set a different softening length of 0.02 and 0.04 for the luminous matter and dark matter (in internal units), and an accuracy parameter of 0.005, which is good enough to assure an accurate force calculation. Each merger history took an average of 320 CPU hours to be completed. In the appendix section we show a example of a parameter file.

Each merger tree evolution was computed with a series of sequential GADGET -2 runs, one for each satellite. Long periods of evolution between successive accretions after the satellite in turn was fully merged were obviated. At the time of arrival, each satellite was placed in a suitable orbit (see Table 3.3) with respect to the total system center of mass as it was at the end of the run for the previous satellite.

Relaxation of the models

While the Smulders & Balcells code generates an accurate equilibrium two-component system, small inaccuracies in the numerical integration of the distribution function at small radii leads the core of the initial model to expand. We therefore evolve the initial model in isolation before using it in the merger

TABLE 3.3— Mass, size and orbital parameters of the satellites of the merger histories

ID (1)	$M_{\rm rat}$ (2)	z (3)	$r_{1/2}$ [kpc] (4)	$V_{\rm R}$ km/s (5)	$V_{\rm T}$ km/s (6)	separation [kpc] (7)	θ ° (8)	ϕ ° (9)
1	5	0.9	1.144	-268.593	201.182	33.900	0	0
2	3	2.00	1.1008	-516.648	172.356	21.688	0.0	0.0
	2.5	0.40	2.0182	-338.180	311.347	23.000	12.0	55.0
3	1.40	0.550	1.965	-295.873	177.313	29.250	0.0	0.0
	5.50	0.400	1.291	-300.068	193.313	22.125	24.0	25.0
	2.00	0.200	2.682	-256.265	234.494	26.875	56.0	128.0
4	4.50	0.80	1.650	-409.840	200.133	21.625	0.0	0.0
	5.50	0.25	1.943	-347.282	223.740	21.688	12.0	159.0
5	2.7	1.60	1.485	-662.852	254.612	18.563	0.0	0.0
	6	1.00	1.275	-516.359	179.018	20.000	48.0	45.0
	6	0.80	1.457	-598.642	279.085	14.688	56.0	87.0
	4	0.75	2.017	-416.712	202.992	21.563	67.0	23.0
	6	0.55	1.926	-319.819	260.829	22.250	56.0	123.0
6	1.65	1.50	2.264	-568.607	261.484	20.250	0.0	0.0
	14	1.10	0.963	-615.088	249.183	14.375	156.0	56.0
	13	0.75	1.135	-615.035	257.524	16.500	45.0	64.0
	6	0.75	1.823	-417.211	228.356	21.250	120.0	25.0
7	3.5	1.300	1.895	-461.381	233.812	21.938	0.0	0.0
	13	1.000	1.115	-517.200	253.379	16.563	56.0	45.0
	1.4	0.100	5.295	-292.645	257.052	28.125	59.0	156.0
8	4	1.200	2.080	-688.846	164.434	19.519	0.0	0.0
	15	1.000	1.174	-705.790	427.834	10.075	-50.0	125.0
	15	0.850	1.260	-624.006	337.262	9.538	-45.0	160.0
	16	0.800	1.276	-869.805	365.276	10.125	30.0	25.0
	14	0.750	1.441	-707.364	309.800	11.563	56.0	87.0
	16	0.600	1.447	-277.904	252.016	13.12	85.0	23.0
	6	0.350	2.798	-237.537	237.196	14.375	41.0	45.0
	7	0.075	3.100	-98.781	185.313	20.000	54.0	42.0

Note.- *Col. (1)*: identification number of the progenitor galaxy, *Col. (2)*: mass ratio, *Col. (3)*: redshift of the merger, *Col. (4)*: half-mass radius, *Cols. (5,6)*: radial and tangential velocities, *Col. (7)*: separation between the main galaxy and the satellite, *Cols. (8,9)*: angles of the orbit.

simulations. Those relaxation runs were executed for 400 internal time units (roughly 20 crossing times of the luminous matter half-mass radius).

In Figure 3.5 we show the temporal evolution of the energy of one of the initial models prior to using it in the merger simulations. In the left panel we have the evolution of the total energy, which is the sum of the total kinetic energy and the potential energy. We see that, even though the total energy tends to increase, it keeps very stable with a $\Delta E \approx 0.08\%$. In the right panel we show the scalar virial theorem evolution. The model reaches the virial equilibrium ($-2T/U = 1$) at $\sim 1/3$ of the total time and subsequently maintains itself closely oscillating around it.

3.5.3 Energy conservation

We checked whether GADGET-2 conserves total energy by evolving one of our progenitor galaxies in isolation over the entire duration of a merger tree. We found errors as high as $\sim 8\%$, such loss of energy being unacceptable in a numerical simulation. Thus, we repeated this simulation systematically changing the parameters that control the accuracy in the numerical integration of the distribution function, in order to to assay if the energy loss was a consequence of collective instabilities due to round-off errors when the model was built. However, the energy conservation problem remained. Hence, we modified the parameters that determine the time step and force accuracy in the GADGET-2 code. We found that changing the cell-opening criterion used in the three walks for computing the gravitational forces (TypeOfOpeningCriterion in the parameter file) from the scheme that tries to limit the absolute truncation error of the multipole expansion for every particle-cell interaction (TypeOfOpeningCriterion 1) to the standard Barnes & Hut scheme (TypeOfOpeningCriterion 0), solved our problem and our models preserved the energy to within 0.15%.

In Figure 3.6, we show a comparison between the total energy conservation for a progenitor galaxy before and after the changes introduced to solve the energy conservation problem. The green line corresponds to simulation with the TypeOfOpeningCriterion 1, and the blue line to the simulation with the standard Barnes & Hut scheme (TypeOfOpeningCriterion 0). In the top panel, we see that with the TypeOfOpeningCriterion 0 the evolution is very flat with an error of 0.71%, whereas with TypeOfOpeningCriterion 1, it continuously rises (top and middle panels) to 7.92%, never reaching the virial equilibrium. In contrast, the model with TypeOfOpeningCriterion 1, once it reaches the virial equilibrium does not deviate from it (bottom panel).

The standard Barnes & Hut scheme gives higher accuracy at the expense of computational cost. In order to keep the simulation time in affordable limits

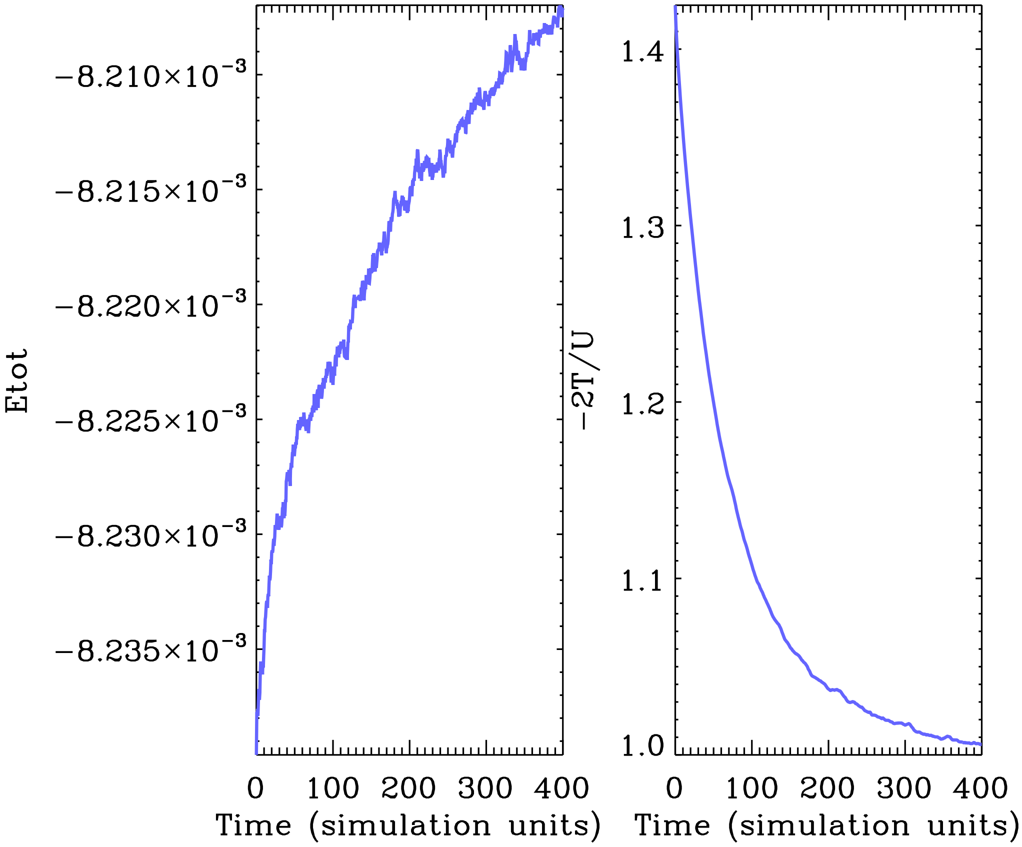

FIGURE 3.5— Total energy and virial theorem of one of the initial models evolved in isolation for 400 internal time units. Left panel: temporal evolution of the total energy of the model. Right panel: temporal evolution of the scalar virial theorem, which is equal to 1 when the system is in equilibrium.

without sacrificing the dynamics of the interactions, we obviated the periods of time between successive accretion of satellites and cut each run after the satellite was completely merged (considered to be completely merged when the centroid of the satellite mass distribution reaches the center of mass of the main galaxy) plus 10 half-mass crossing times of the luminous component of the given satellite (based on the merger histories that did not conserve energy). This time was shorter than that given by the cosmological simulations (see Table 3.3), which has the advantage of reducing the numerical noise that is inevitably produced in long-time integration simulations.

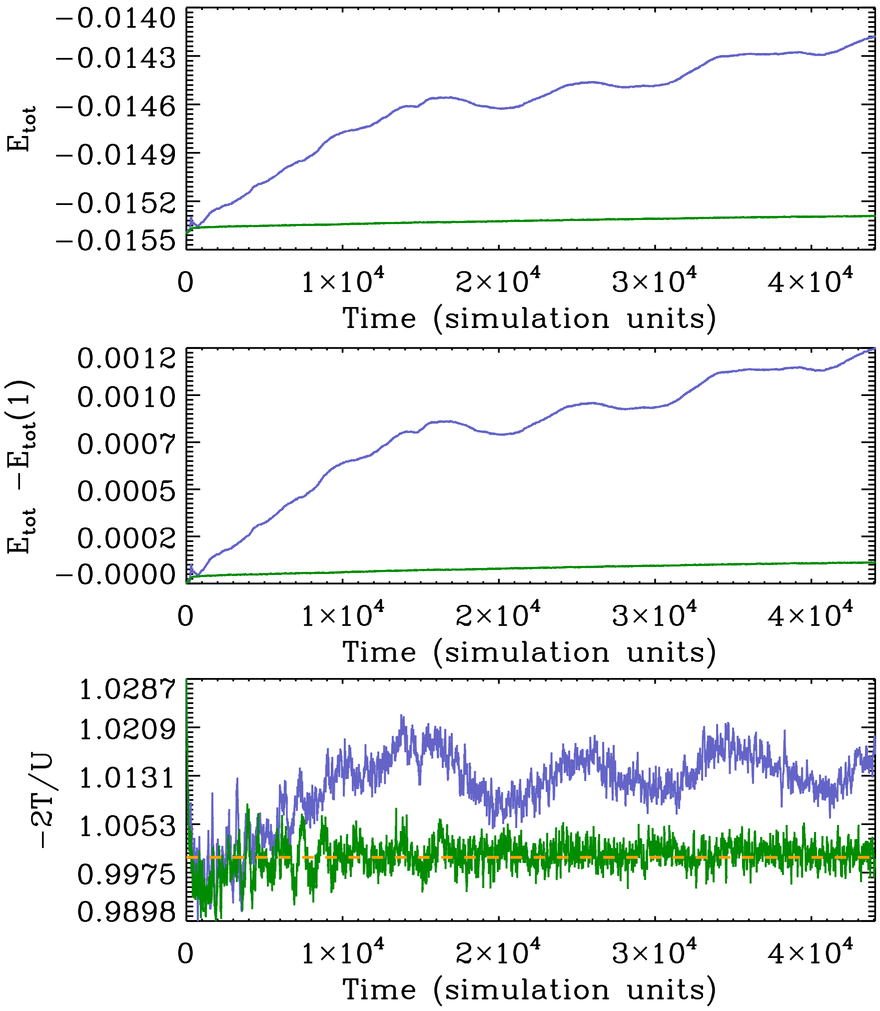

FIGURE 3.6— Total energy and virial theorem for one of our progenitor galaxies evolving in isolation for the whole simulation time of merger tree (which is equivalent to ∼ 10.54 Gyrs) with the two types of cell opening criteria allowed in GADGET-2. The green line corresponds to the standard Barnes & Hut scheme (TypeOfOpeningCriterion 0). The blue line corresponds to the criterion that limits the absolute truncation error of the multiple expansion (TypeOfOpeningCriterion 1). The yellow dashed line corresponds to those points that fulfill the virial equilibrium $-2T/U = 1$.

In Figure 3.7 we show the energy conservation of one of the merger trees. This particular case corresponds to that labelled “5” (see 3.2 and 3.3 Tables). In the top panel, we have the total energy during the simulation. The time is given by the cosmological simulations and the gaps correspond to the periods of time that were obviated. In the middle panel we show the total energy only for the simulation run time. In the bottom panel, we see the energy increase due to the accretion process, where the total energy of the system at the end of one accretion was considered as the initial value for the next one. For this merger tree we had estimated a total energy conservation of ~ 0.2.

Scaling relations between models

To test the code performance due to a change in the mass of the initial model, we took the effective radius and the velocity dispersion of two different models (calculated as explained in Section 3.6), and from equation 3.11 we have that $\sigma^2 = \alpha GM/R$. The ratio between the velocity dispersion is then given by:

$$\frac{\sigma_2^2}{\sigma_1^2} = \left(\frac{R_1}{R_2}\right)\left(\frac{M_2}{M_1}\right). \tag{3.9}$$

In Figure 3.8 we plot the ratios of both sides of the equation 3.9 for two of our progenitor galaxies (numbered 3 and 5 in Table 3.2) evolving in isolation for 8000 simulation time units. We see that the temporal evolution of the velocity dispersion ratio is more stable than the equivalent right hand side of the equation 3.9. If we compare the quotient between them (bottom panel), we see that they do not differ significantly; this deviation, of the order of 0.05, can be attribute to round-off errors. Thus, we can ensure that the models' outcomes under test are numerically well-behaved.

3.6 Methods

In this section we explain how we measured the physical properties of the models.

3.6.1 Effective radius

It has been estimated using the projected half-mass radius, which we directly measured from the projected profile as seen from 50 different randomly chosen lines-of-sight and taking the mean value and the standard deviation as an estimate of its error. The measurements were taken considering all the particles within a maximum radius.

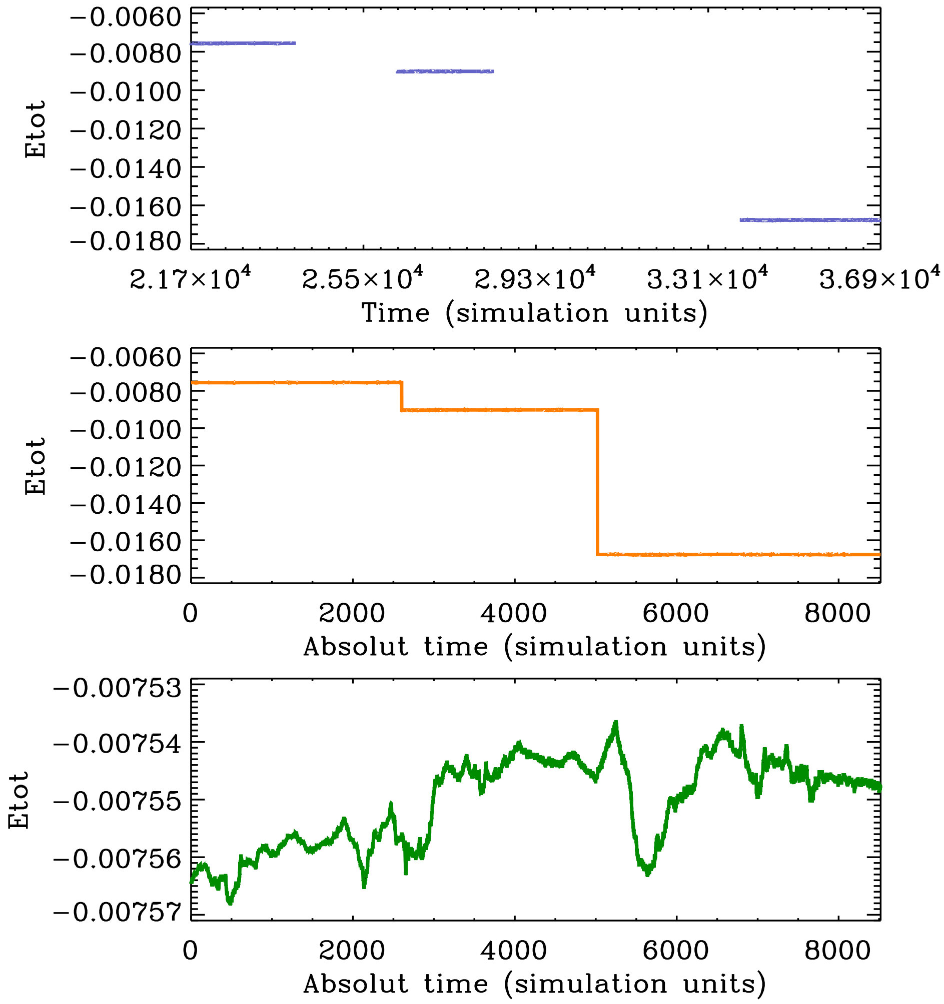

FIGURE 3.7— Energy conservation of one the merger tree 5. Top: Total internal energy during the entire simulation; the gaps correspond to the time intervals for which we did not computed the runs. Middle: Same as the upper plot but with the real simulated time only. Bottom: Normalized increase of energy. Considering the internal energy given by the sum of the initial and that contributed by each satellite.

3.6.2 velocity dispersion

It has been calculated from the projected velocity within the effective radius, considering the same maximum radius as in the calculation of the effective

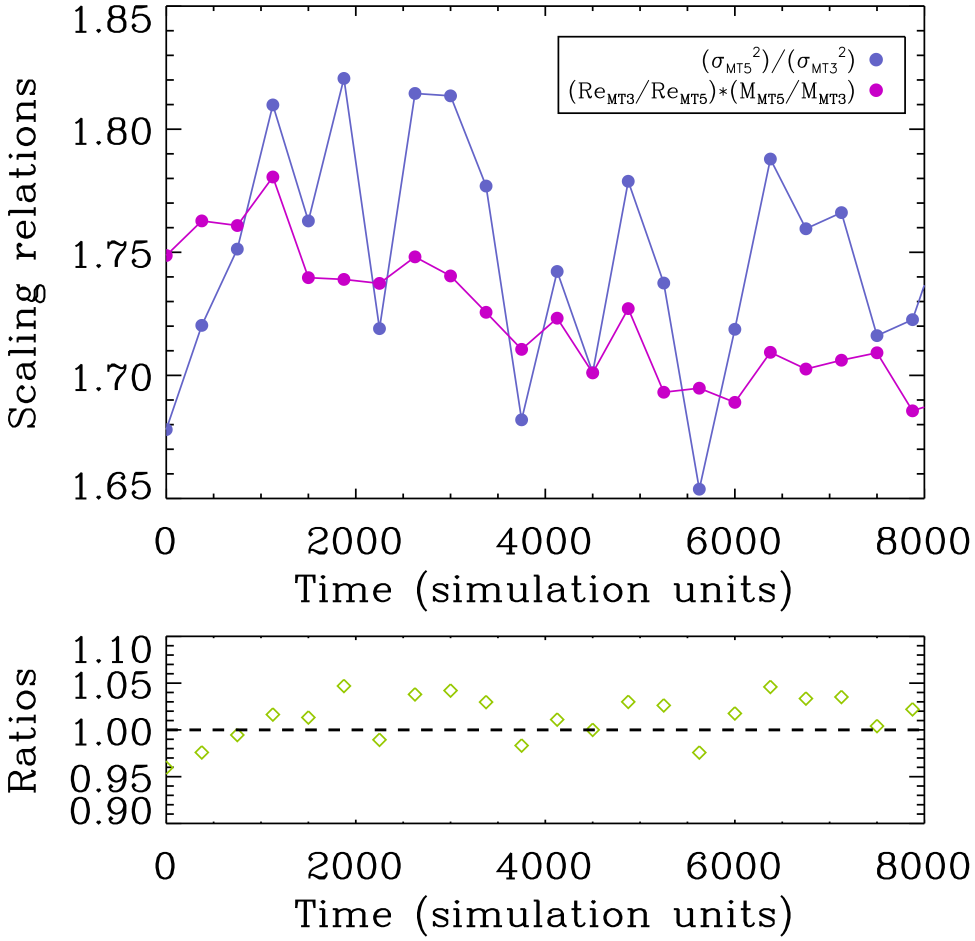

FIGURE 3.8— Top: Comparison of scaling relations for two galaxy models with different masses. Bottom: quotient of the above quantities.

radius. This method was used for all the models.

3.6.3 Stellar mass

The sum of the masses of all the luminous matter particles involved.

3.6.4 Dynamical mass

The estimate is obtained from the scalar virial theorem (Binney & Tremaine 2008, and references therein). The kinetic energy of a stellar system with mass

M is simply $K = \frac{1}{2}M < v^2 >$, where $< v^2 >$ is the mean-square speed and r_g the gravitational radius. Hence the virial theorem states that:

$$< v^2 >= \frac{|W|}{M} = \frac{GM}{r_\mathrm{g}} \tag{3.10}$$

Let M, R, and $\sigma = \sqrt{< v^2 >}$ denote mass, radius and velocity dispersion, respectively. According to the virial theorem, the velocity dispersion follows from $\sigma = \alpha GM/R$, where α is a parameter that takes into account the structure of the system.

Thus, the dynamical mass is given by:

$$M_{dyn} = \alpha \left(\sigma^2 R/G\right) \tag{3.11}$$

3.6.5 Surface density profile

To measure the surface density, we first put the galaxy model in the centre of coordinates and select a maximum coordinate (r_max) at which we will measure. Next, we define a linearly-spaced grid of $\log r$ values between a minimum $\log r = 0.1$ and r_max; then we find the projected coordinates, the cumulative mass M_cum, and calculate $M^i_\mathrm{cum}/\pi * ((x^i_\mathrm{proj})^2 + (y^i_\mathrm{proj})^2)$ for each i particle.

3.7 Results

3.7.1 Stellar surface density profile

In Figure 3.9 we show the stellar surface density profile of the merger trees. We can see the change in the stellar density profile since the beginning of the simulation (which corresponds to the green filled circles) to redshift zero when the last satellite has merged, for the material that originally belongs to the progenitor galaxy (the orange filled circles) and for the remnant (the blue filled circles). We have also plotted the stellar surface density of all the satellites at the end of the simulation (red filled circles). We see that the satellites' material is mainly deposited at most external radii and only a small amount reaches the center, which is dominated by the main galaxy. The overall effect of adding satellites is to decrease the stellar surface density profile in the inner part and moving it to the outskirts. That implies a remnant that has a lower density and is more extended than the progenitor high-redshift galaxy.

3.7.2 Effective radius and velocity dispersion

In Figure 3.10, we show the evolution of r_e and σ with time for the merger tree 7. In this tree, 8 satellites merge at approximate times 2.3, 2.9, 3.6, 3.8, 4.0, 4.9,

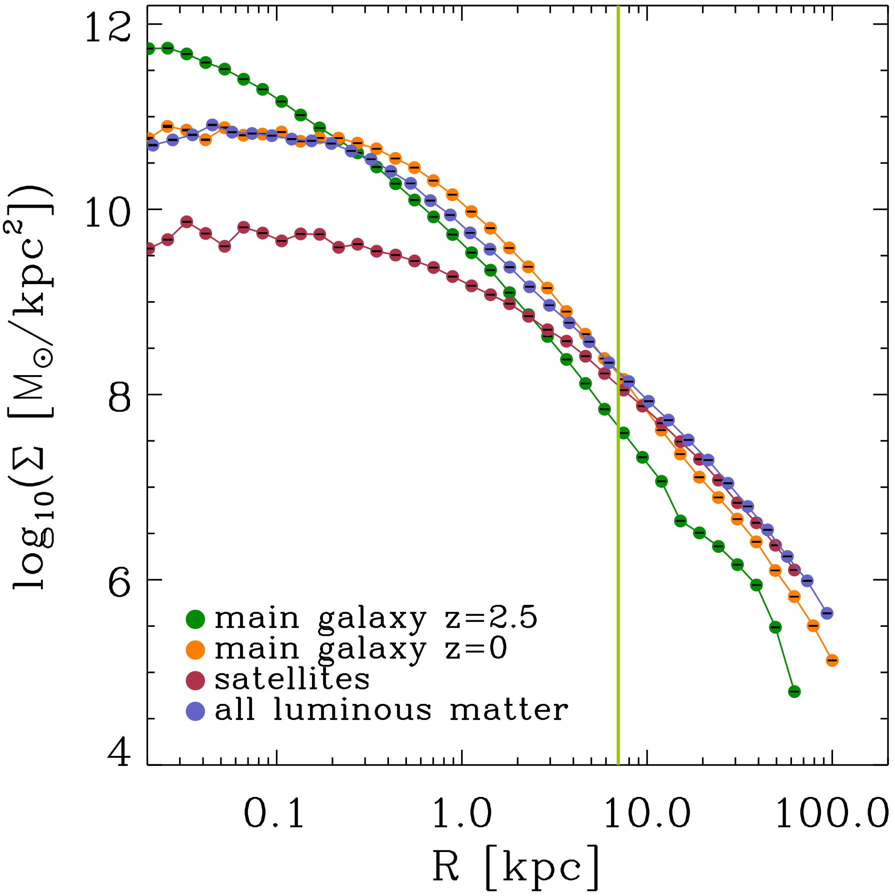

FIGURE 3.9— Stellar surface density profile of one merging history (labelled "7"). The green filled circles correspond to the progenitor at the beginning of the simulation at $z = 2.5$; the orange circles correspond to the final state of the material that originally belongs to the progenitor galaxy at $z = 0$; the red filled circles correspond to the contribution of all the satellites and the blue ones to the total luminous matter of the remnant at $z = 0.0$. The pale-green line represents the effective radius of the remnant at the end of the simulation.

6.7 and and 9.5 Gyrs, indicated by the blue lines in the top panel. Horizontal bands denote time intervals without mergers, in which the simulation was not computed. We find that r_e increases in each merger, with a total increase of a factor 4.928 ± 0.050. Surprisingly, the velocity dispersion changes by a factor 1.136 ± 0.064 only. This is our more active merger histories the others, however the highest size increase correspond to the labelled as the, which with just 2 satellites grow a factor 6.602 ± 0.038.

Size growth efficiency

The analytical estimations under the assumptions of energy conservation, single component galaxies, and a parabolic orbit in a minor merger of Naab et al. 2009 show that the ratio of the final to initial gravitational radius is:

$$r_{\mathrm{g,f}}/r_{\mathrm{g,i}} = \frac{(1+\eta)^2}{(1+\eta\epsilon)} \tag{3.12}$$

Where η is defined as $\eta = M_a/M_i$, which is the fractional mass increase from all the accreted material. And, $\epsilon = \langle v_a^2 \rangle / \langle v_i^2 \rangle$, are the mean square speed of the accreted material and the initial stellar system, respectively. The subscripts a, i and f denote accreted, initial and final, respectively.

We calculated the analytical growth estimation for all our models. Since the equation (3.12) is for one accretion event, we change each time what we consider the initial state and the accreted material, taking the cumulative mass, velocity and the radius of the remnant before the merger with the corresponding satellite as the initial material and the current satellite as the accreted material. To illustrate that in general we find a lower ratio of the final to initial radius than the analytical predictions, in Figure 3.11 we show the size and velocity dispersion ratio of one merger history (labelled 7). In the top panel we show the size ratio each time a satellite is accreted, both the analytical and the measured, and in the bottom panel the same for the velocity dispersion ratio. We see that the analytical estimations are systematically higher than our measurements. However, for the velocity dispersion we see the opposite, i.e. the velocity dispersion of our galaxies is higher than the one calculated analytically, except for two satellites (s3 and s5).

3.7.3 Redshift evolution

To find the relation between the effective radius and the redshift, we plot the effective radii of all our remnants against redshift in Figure 3.12. Individual measurements are plotted each time the remnant undergo an accretion, and median values are plotted at specific redshifts (6 intervals with the same redshift

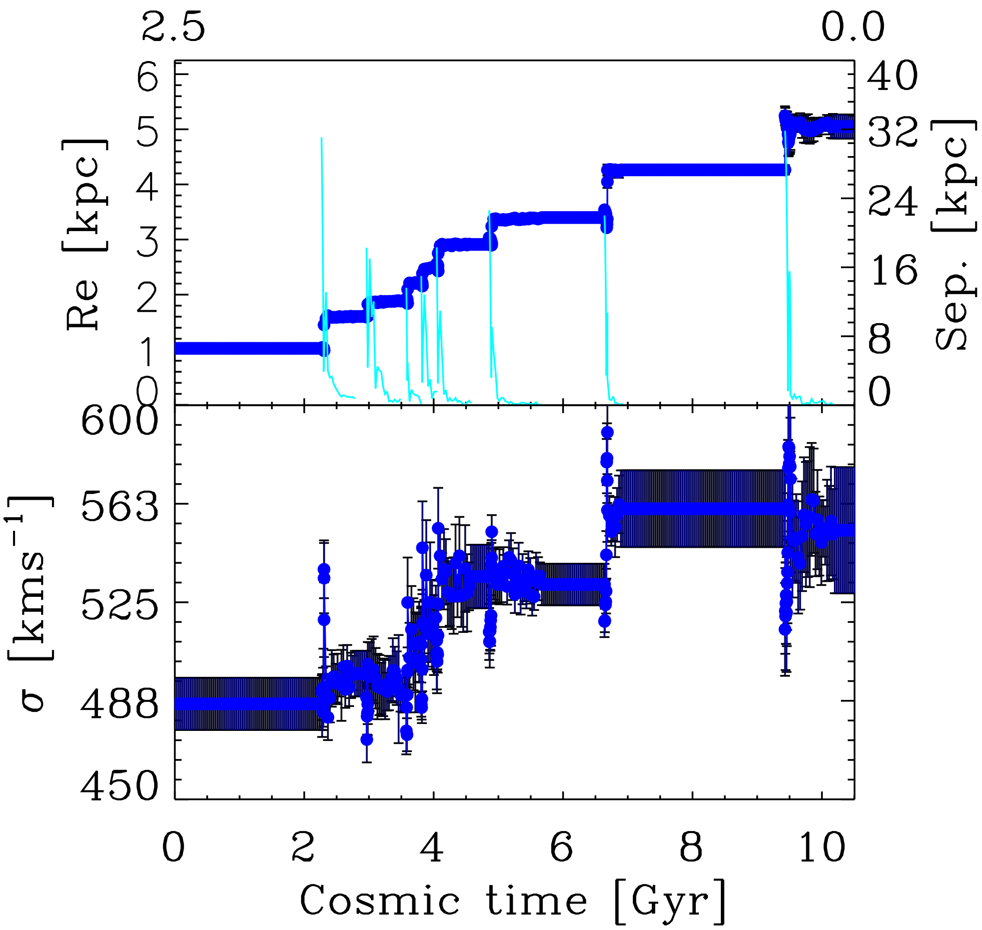

FIGURE 3.10— Temporal evolution of one merging history (labelled "7"). Top panel: Temporal evolution of the effective radius. The relative separation between the median of the mass distribution for the main galaxy and median of the mass distribution for the satellite is plotted in blue. Bottom panel: Temporal evolution of the velocity dispersion. A cosmic time equal to zero corresponds to redshift 2.5.

range as Figure 3.15). We fit a power law to the individual measurements using the ordinary least square bisector method (Isobe et al. 1990). Thus, we find that the relationship is:

$$\mathrm{r_e} = (6.882 \pm 0.050 \ \mathrm{kpc})\,(1+\mathrm{z})^{-1.738 \pm 0.121} \tag{3.13}$$

This result is similar to the founded by Oser et al. (2012), more akin to his

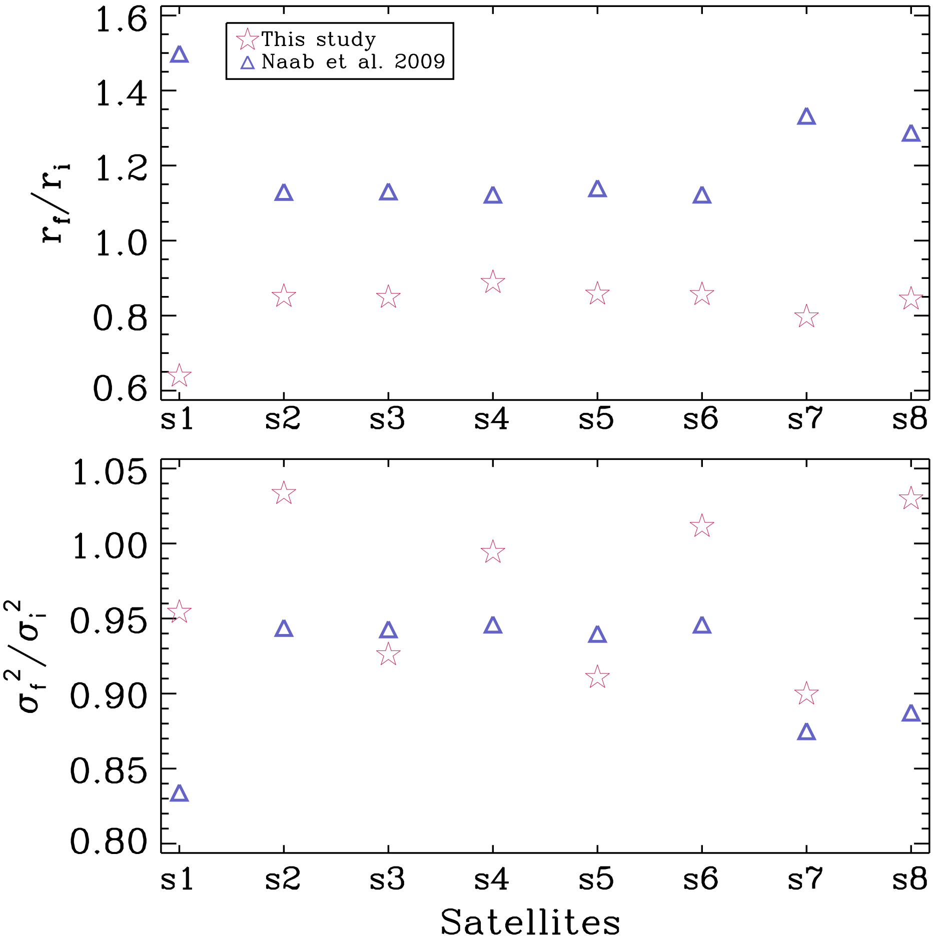

FIGURE 3.11— Size and velocity dispersion ratios for the merger tree "7". Top panel: ratios of the final to initial radius of the remnant each time an accretion event occurs. Red stars were calculated using our measurements and the blue triangles correspond to the analytical estimation following Naab et al. (2009). Bottom panel: velocity dispersion ratio.

quiescent galaxies than for his entire sample.

For the velocity dispersion we find that there is a slight increase due to the accretion events, in disagreement with what has been measured in other studies (Oser et al. 2012; Nipoti et al. 2012; Newman et al. 2012).

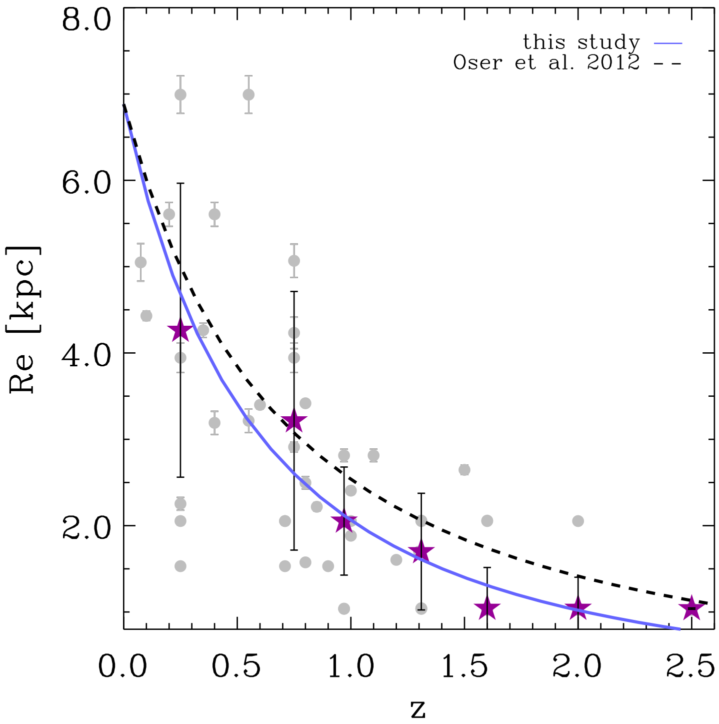

FIGURE 3.12— Effective radius of the remnants as a function of redshift. In gray we show all the individual measurements each time an accretion occurs; the magenta stars correspond to the median values separated in n redshifts intervals. our power law fit (blue line) and the fit of Oser et al. (2012) for his quiescent galaxies (dashed line) are over-plotted on the observed distribution of points.

$$\sigma/\sigma(\mathrm{z}=2.5)=\left(279.534\pm0.005\ \ \mathrm{kms}^{-1}\right)(1+\mathrm{z})^{-0.123\pm0.018} \tag{3.14}$$

3.7.4 Stellar mass-size relation

In the case of the relation between the effective radius and the mass, we also fitted an exponential relation (see Figure 3.14) and we have found it to be a good fit, since they follow the relationship

$$\mathrm{r_{ef}/r_e(z=2.5)}=(1.182\pm0.035)\left(\frac{\mathrm{M_{\star f}}}{\mathrm{M_\star(z=2.5)}}\right)^{(1.547\pm0.147)} \tag{3.15}$$

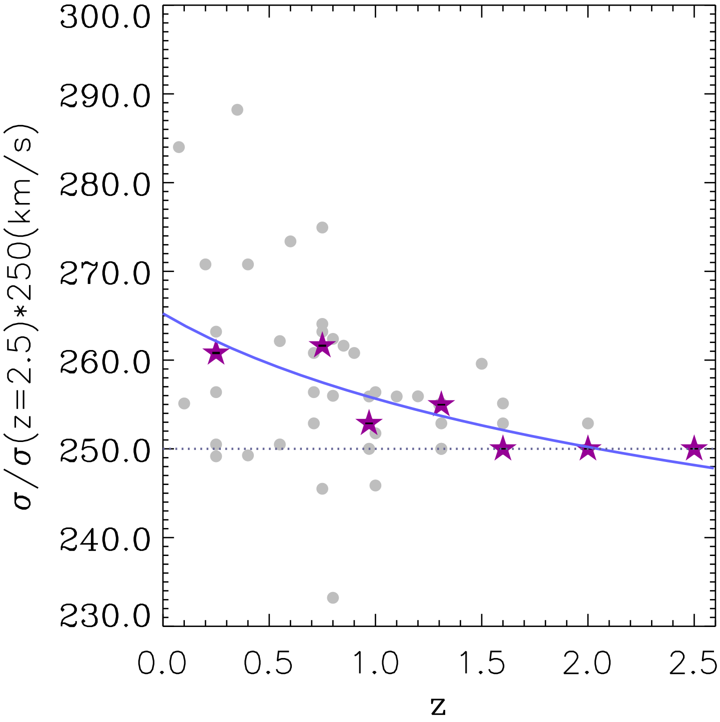

FIGURE 3.13— Velocity dispersion of the remnants as a function of redshift. We follow the same notation as in Figure 3.12, although in this case each measurement is normalized by the initial velocity dispersion of the progenitor at $z = 2.5$ and times 250 km s^{-1} .

And,

$$\sigma_{\rm f}/\sigma({\rm z}=2.5) = (1.008 \pm 0.011)\left(\frac{{\rm M}_{\star {\rm f}}}{{\rm M}_{\star}({\rm z}=2.5)}\right)^{(0.044\pm0.038)} \tag{3.16}$$

These relations are intermediate between that provided by Hilz et al. (2012), who found a large size increase of $r_e \propto M_{\star}^{2.00}$) and a much weaker size increase given by Nipoti et al. (2009), $r_e \propto M_{\star}^{1.09\pm0.29}$, and that $\sigma \propto M_{\star}^{0.07\pm0.11}$. Nipoti et al. (2009) argue that the growth of R_e with M due to dry mergers is too small to explain observations. We see here that our dry mergers lead to a more pronounced size growth. We show in the next section that our models match observed evolution of mass-size relation.

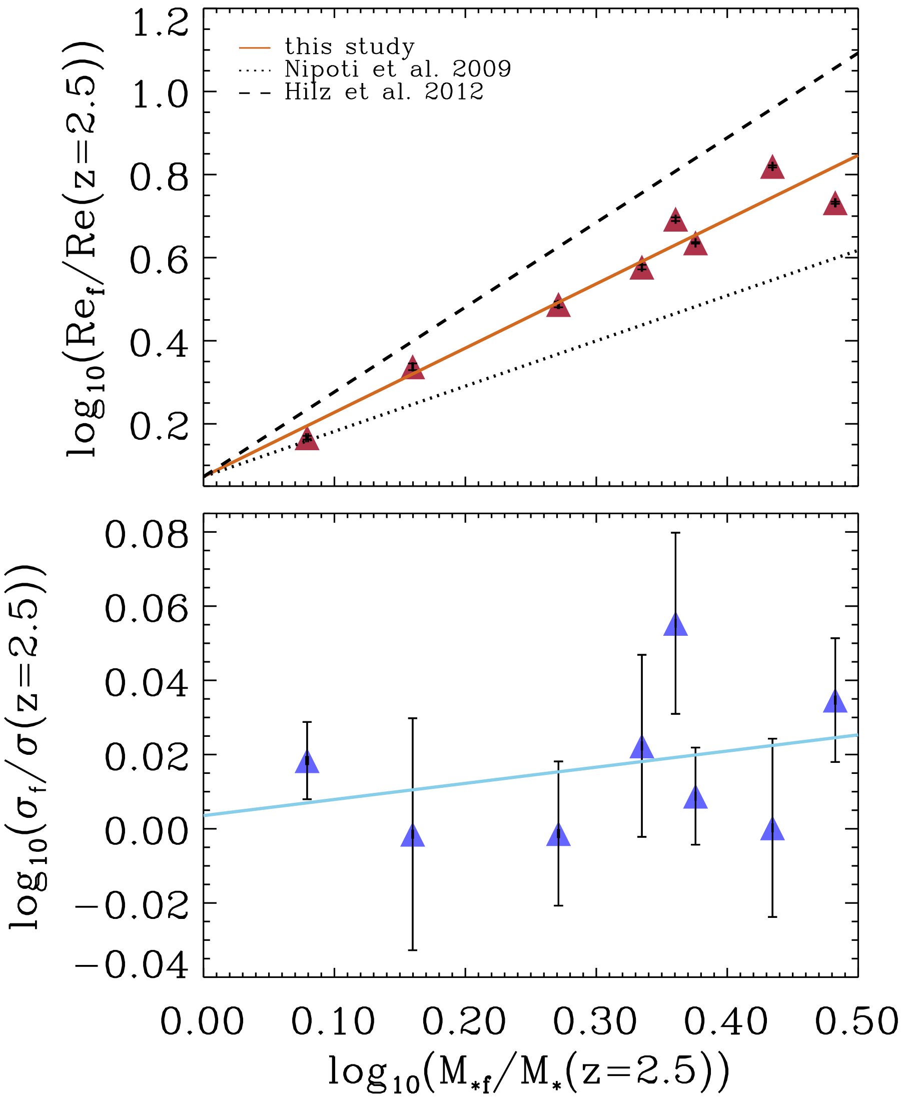

FIGURE 3.14— Relationship between stellar mass and effective radius, and stellar mass and the velocity dispersion for all our remnants. The red triangles represent the effective radii normalized to the initial effective radius of the main galaxy at $z = 2.5$; the blue triangles represent the velocity dispersion, also normalized by the initial velocity dispersion of the main galaxy. The brown and sky-blue lines are the power law fits, and the dashed and dotted lines are the fits of Hilz et al. (2012) and Nipoti et al. (2009), respectively.

Observed size-mass evolution

We have taken the sample of high-concentrated (spheroid like) galaxies from Trujillo et al. (2007) and over-plotted those to our simulated galaxies. Their sample consist of 831very massive galaxies ($M_\star \geq 10^{11}h_{70}^{-2}\mathrm{M}_\odot$) located over $\sim$ 710 arcmin^2 in the Extended Groth Strip (EGS) defined from the Palomar Observatory Wide-field Infrared (POWIR)/ DEEP-2 survey; Davis et al. 2003; Bundy et al. 2006; Conselice et al. 2007) and imaged with the Advanced Camera for Surveys (ACS) in the V band (F606W, 2660 s) and I band (F814W, 2100 s). Trujillo et al. (2007) split their sample according to their light concentration using the Sérsic index n. At a given stellar mass, both low ($n < 2.5$) and high ($n > 2.5$). Galaxy sizes were determined from a Sérsic model fit (Blanton et al. 2003). This comparison is presented in Figure 3.15, where we have divided the data (spanning the range $0 < z < 2.1$) into six redshift slices. We find that, though starting with ultra compact galaxies, our models reproduce quite well the observed distribution at $z = 0$.

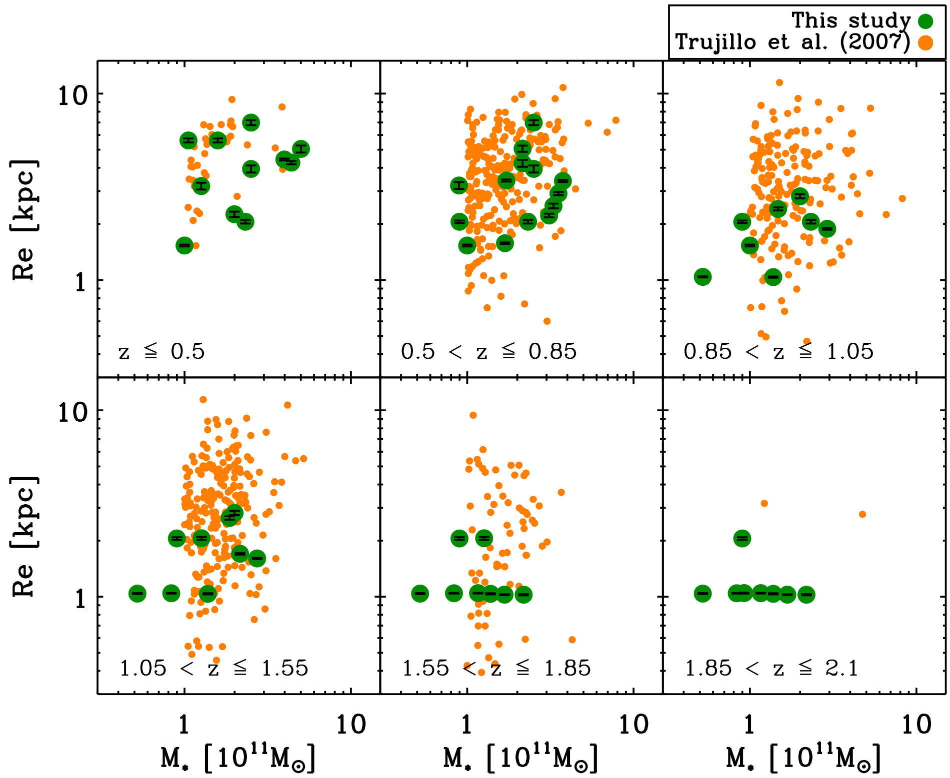

FIGURE 3.15— Effective radius distribution of our models. The stellar mass size distribution of the spheroid-like galaxies ($n > 2.5$) from the sample of Trujillo et al. (2007) are over-plotted.

3.7.5 Dynamical and stellar masses

Many studies have found a discrepancy between the stellar and the dynamical mass for early-type galaxies. For example, Cappellari et al. (2006) and van de Sande et al. (2011) showed that dynamical masses are on average equal or larger than stellar masses, whereas Martinez-Manso et al. (2011), studying four massive and compact early-type galaxies at $z \sim 1$, found that dynamical masses where smaller by an average factor of ~ 6. The discrepancy in the stellar mass may be related with the manner in which the different approaches account for the stellar populations (Ferré-Mateu et al. 2012) or due to variations in the initial mass functions in early-type galaxies as a function of their stellar mass-to-light ratios (Cappellari et al. 2012). For the dynamical mass, the estimates come from the scalar virial theorem (Binney & Tremaine 2008, and references therein); therefore it directly depends on the accuracy of the size and velocity dispersion measurements.

Following Bertin et al. (2002), equation 3.11 could be approximated as:

$$M_{vir} = K(n)\sigma^2 r_e/G. \tag{3.17}$$

With:

$$K(n) = 73.32/10.465 + (n - 0.95)^2 + 0.954, \tag{3.18}$$

where n is the Sersic index, R_e the circularized effective radii in kpc and σ the velocity dispersion in km/s. For $K(n)$, under the assumption of homology, Cappellari et al. (2006) determined that for a De Vaucouleurs $r^{1/4}$ profile, this factor is equal to 5.

In Figure 3.16, we show the stellar and dynamical mass for one of our merger histories (labelled as "8") along the simulation. In one case, we assume $\alpha = 1$ for the dynamical mass; in the other case, we take the factor $K(n) = 5$ given by Cappellari et al. (2006). The marked increase in the mass is due to the injection of mass from each of the satellites (eight in this case). We find that the stellar mass is larger than the dynamical mass when $\alpha = 1$, but lower when we consider $K(n) = 5$. It is remarkable that at the beginning of the simulation, the stellar mass of our model is close to the dynamical mass with $K(n) = 5$, but as the time passes the differences between these become larger. This leads us to conclude that the $K(n) = 5$ case is not appropriate for our models. Thus, we fit a power law to the stellar mass and the $\sigma^2 r_e/G$ in order to determine the α parameter, which can be seen in Figure 3.17. We have found that for our models:

$$\mathrm{M_{dyn}} = (1.451 \pm 0.047)\,(\mathrm{M}_\star)^{0.818 \pm 0.101} \tag{3.19}$$

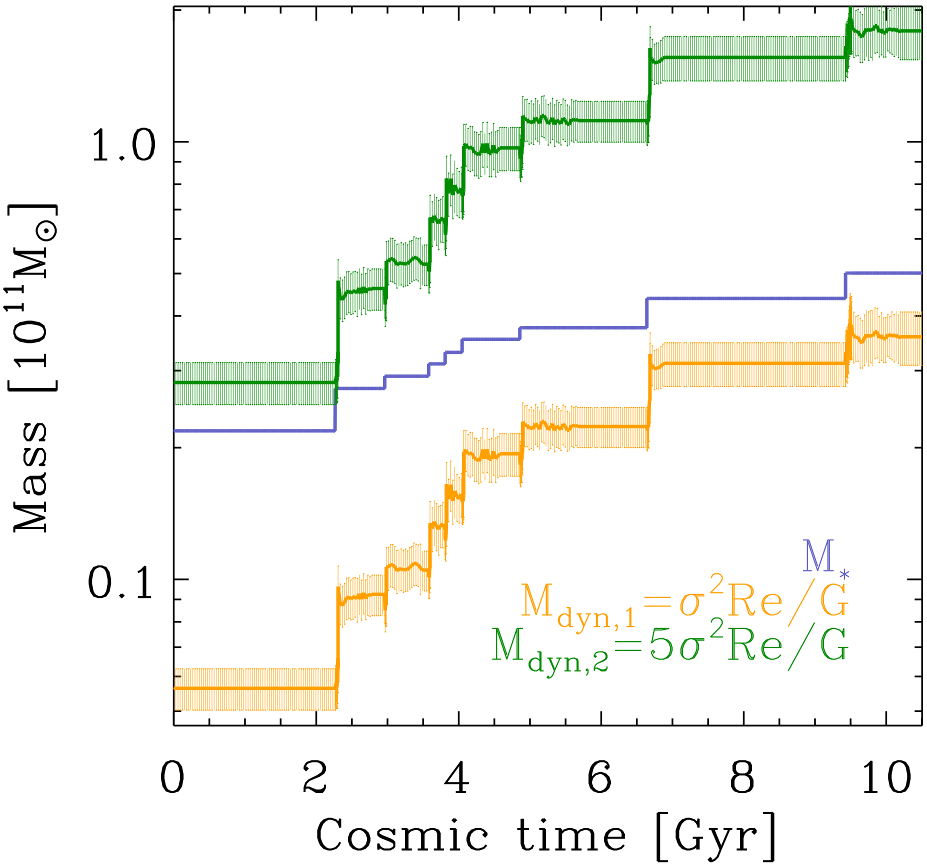

FIGURE 3.16— Temporal evolution of the stellar and dynamical mass for the merger history labelled as "8". Stellar mass is plotted in blue, the orange line corresponds to the dynamical mass assuming $\alpha = 1$ and the green line corresponds to the one with $K(n) = 5$.

$$\mathrm{M_{dyn}} = (1.744 \pm 0.233)\left(\sigma^2 \mathrm{r_e}/\mathrm{G}\right) \tag{3.20}$$

3.8 Conclusions

We analyzed eight different high-resolution merger histories of massive elliptical galaxies. The mass ratio and orbital parameters of these galaxies were extracted from self-consistent cosmological simulations, and we followed observational

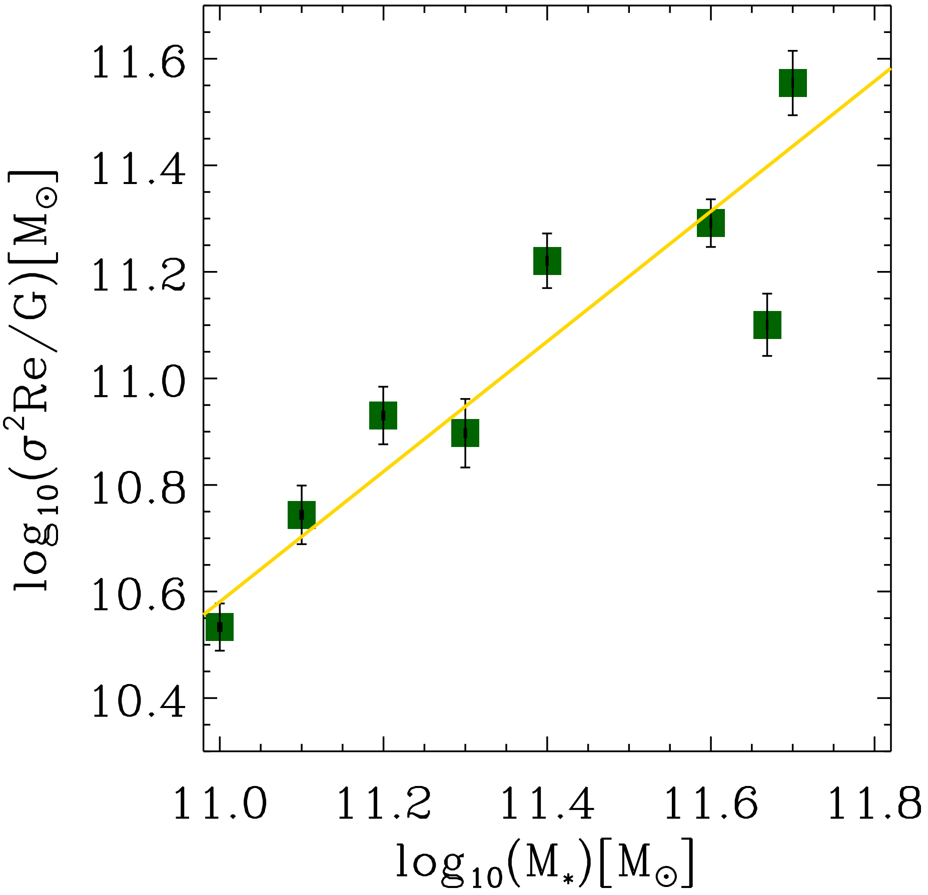

FIGURE 3.17— Power-law fit to the relation between the dynamical and stellar masses. The filled circles correspond to each of the remnants.

relationships to set their sizes. Our progenitor galaxies at $z = 2$ resemble observed high-redshift galaxies with $r_e \sim 1$ kpc with a mass range between $5.21 \times 10^{10}\mathrm{M}_\odot$ and $2.18 \times 10^{11}\mathrm{M}_\odot$, and a variety of velocity dispersions from ~ 236 km s^{-1} to ~ 486 km s^{-1} .

In all the simulations, only the most massive galaxy (the progenitor) survives until $z = 0$. These remnants, being less compact than their $z = 2$ counterparts, result from the merging and interactions with the accreted satellites, which loose their structure and deposit their material in the outer part of the main galaxy, producing its size growth. We found that our galaxies grow in size on average by a factor of 4.3208 ± 0.040 with a slight increase in the velocity dispersion of a factor of 1.043 ± 0.055. These findings are in agreement with diverse observational works (e.g. van Dokkum et al. 2011; Trujillo et al. 2011), as well as with simulations (Naab et al. 2006; Hopkins et al. 2010a; Oser et al. 2010), although the size increase is marginally smaller than that predicted from simple virial arguments Naab et al. 2009.

The increase of the mass in the outer parts occurred with little or no increase in the central velocity dispersion of our remnants, which supports the scenario whereby elliptical galaxies grow inside-out.

Observational estimates of van Dokkum et al. (2010) indicate a size growth of $r_e \propto M^{2.4}$. The size growth that we find is given by $r_e \propto M^{1.5}$ which, in spite of being more rapid than other studies (Nipoti et al. 2009, 2012), does not fully match the observations.

The dynamical mass of our remnants is smaller than the stellar mass, or greater if we follow the approximation of Bertin et al. (2002). We have found that our galaxies obey $M_{dyn} \approx 2\left(\sigma^2 r/G\right)$, which has a lower $K(n)$ than the one given by Cappellari et al. (2006).

To conclude, our results indicate that dry minor mergers provide a potential mechanism for explaining the size growth and the build-up of present-day massive elliptical systems.

3.9 Future work

One important limitation to our analysis is that we assume that the progenitors and accreted galaxies are all spheroids. Observational studies have found that at high-z a large fraction of massive compact galaxies were disk dominated (van der Wel et al. 2011; Weinzirl et al. 2011; Szomoru et al. 2012). Given that the comoving number density of $z \sim 2$ galaxies with stellar masses $\sim 10^{11}\mathrm{M}_\odot$ is the same as that of present-day galaxies with stellar masses $\sim 3 \times 10^{11}\mathrm{M}_\odot$ (van Dokkum et al. 2010), the present day descendants of those galaxies are 2–3 times more massive, ~ 5 times larger in half-light radius, and almost never have prominent stellar disks (van der Wel et al. 2009). Thus, it have been suggested a direct link between the disk-like galaxies at $z \sim 2$ and the pressure-supported, massive elliptical galaxies in the present-day universe (van der Wel et al. 2011; Weinzirl et al. 2011).

As we mentioned in Section 3.1, in general terms, massive galaxies have experienced a substantial growth since $z \sim 2$ and dry mergers seems the most promising mechanism to turn massive galaxies into their present-day descendent, which are primarily E and S0s. By replacing our elliptical parent galaxies with disc-dominated galaxies, from our merger histories we could explore whether dry mergers can generate remnants with $n \sim 4$, a higher effective radius, and a lower surface brightness within the effective radius than their progenitors (Naab et al. 2006; Naab & Trujillo 2006; Naab et al. 2009). Also, we could test if it is possible that the present-day descendants of $z \sim 2$ early-type galaxies might be the bulges of massive disc galaxies (Graham 2011), thus providing a constraint on the evolution that massive compact high-redshift galaxies have undergone.

4

Effects of dry mergers on the metallicity gradients of massive elliptical galaxies

In this chapter we explore whether sequential dry mergers produce a noticeable metallicity gradient in the remnant of a massive elliptical galaxy. To perform this study we followed observational mass-metallicity relationships to assign to each galaxy a total metallicity according to its mass and the redshift at which it was accreted and a radial metallicity gradient as a function of its mass. We find that the effect of satellite accretion results in a flattenning of the metallicity gradient in the remnant. Moreover, a high number of mergers are more efficient in smoothing the metallicty gradient.

4.1 Introduction

Stellar mass and metallicity are two of the most fundamental physical properties of galaxies. Both are metrics of the galaxy evolution process. Mass determines the assembly of galaxies over cosmic time and metallicity is the thermodynamical fossil imprint of galaxy formation and evolution mechanisms. Understanding how these quantities evolve with time and in relation to one another provides a strong constraint on galaxy formation.

The study of the relationship between mass and metallicity dates back several decades, beginning with the seminal work of Lequeux et al. (1979), who found a luminosity-metallicity relation for irregular galaxies. In elliptical galaxies, Visvanathan & Sandage (1977) established for the first time the existence of a color-luminosity relation, which was corroborated by numerous other works (e.g. Bower et al. 1992a,b). Later on, it was understood that this luminosity-metallicity relation is a manifestation of a more fundamental stellar mass-metallicity relation, whereby galaxies with larger stellar mass have higher metallicities (e.g. Garnett 2002; Pérez-González et al. 2003; Tremonti et al. 2004). The origin of this relation is debated, owing to the difficulty of connecting the information derived from observables to the ingredients needed for simple chemical evolution models (stellar mass, gas mass and metallicity). As with other fundamental relations in massive ellipticals such as the fundamental plane (e.g. Jorgensen et al. 1996), one of the fundamental challenges put by the color-luminosity relation is its strong tightness (Bower et al. 1992b), which suggests that the color-luminosity relation may be universal. Understanding the color as the combined tracer of age and metallicity of the stellar populations, the tight relation would require extremely synchronized and short-duration star formation events for all ellipticals in a distant past, undoubtedly a challenge to hierarchical formation models, and in excellent agreement with monolithic collapse models (e.g. Arimoto & Yoshii 1986).

Equally important as a check on formation models for elliptical galaxies are the systematics of metallicity gradients. Metallicity gradients have been inferred from color profiles (Peletier et al. 1990) and from line strength profiles (Gorgas et al. 1990; Sánchez-Blázquez et al. 2006). Current understanding is that color gradients in ellipticals become steeper with mass up to a galaxy mass about $\log M_\star \sim 10.5$, and show strong scatter for higher masses; bulges of early-type disk galaxies show a similar behavior (Balcells & Peletier 1994). These relations are useful because competing scenarios for the formation of early-type galaxies predict contrasting behaviors for the mass-metallicity gradient relation. In the classical model of monolithic collapse, the inflowing gas is chemically enriched by evolving stars and contributes metal-rich fuel for star formation. Thus, a negative radial gradient is established, in which central stars are more metal-rich than those born in outer galaxy regions (Eggen et al. 1962; Larson 1974). The depth of the galaxy potential well regulates the effectiveness of these processes, so that a strong correlation between metallicity gradients and galaxy mass is expected. Franx & Illingworth (1990) connected the diagnostics given by the mass-color relation and the mass-color gradient relation by noting that *local* color in ellipticals scales with escape velocity. This connection put in firm footing the concept that color, in as much as it is determined by metallicity, is established by the ability of the galaxy potential well to retain the metals expelled by supernovae into the interstellar medium. Subsequent more detailed modeling showed that the ability of higher-mass galaxies to retain more metals leads to steep negative metallicity gradients of -0.5 dex per radius dex, compared to low-mass systems with almost zero gradient (Gibson 1997; Chiosi & Carraro

2002).

In the hierarchical clustering scenario of galaxy formation, predictions of the resultant metallicity gradient of a merger remnant are more complicated, since the latter depends on a large number of free parameters (Sánchez-Blázquez et al. 2007). The turbulent mixing caused by merging events was initially believed to "wash out" any possible population gradient present in the progenitor galaxies (White 1980). Later modeling of the merger process in N-body simulations showed that mergers do preserve pre-existing gradients owing to the fact that violent relaxation is incomplete in mergers (van Albada 1982; Di Matteo et al. 2009). Furthermore, once hydrodynamics and star formation were included in the models it became clear that metallicity gradients are actually produced by a rapid central merger-induced starburst, and their strength is proportional to the efficiency of the dissipative process (Hopkins et al. 2008a). The gradients are predicted to only weakly depend on the remnant galactic mass (Bekki & Shioya 1999; Kobayashi 2004; Hopkins et al. 2009a).

Recently, den Brok et al. (2011), interpreting the colors as metallicity tracers, found that almost all color gradients are negative, both for elliptical and lenticular galaxies, opposite to what has been claimed in the literature. They suggested that dwarfs as well as giant early-type galaxies in the Coma cluster are less metal rich in their outer parts, without environmental influence on the gradient.

In summary, we expect metallicity gradients to be the combined result of several processes. The mass-metalicity relation (hereafter M-Z relation) for galaxies with present-day stellar masses down to $10^{10}\mathrm{M}_{\odot}$ appears to be mainly driven by the history of star formation (and not by the interplay of inflows and outflows (Vale Asari et al. 2009). After a mass assembly process dominated by mergers, the final gradients are the combined result of merger-induced star formation and the radial distribution of stars in the remnants.

4.2 Motivation

For massive ellipticals ($M_\star \geq 10^{11} M_\odot$) population diagnostics indicate mean population ages above 10 Gyr, suggesting a merger history dominated by dry mergers. We can anticipate in this case that present-day gradients result from the imprint of the radial deposition of stars in dry mergers superimposed on the pre-existing gradient. Because the proto-elliptical is most likely the result of a rapid gas-rich collapse, it is reasonable to assume an initial metallicity gradient. There are no observational constraints for this gradient, while monolithic collapse models yield metallicity gradients of 0.5 dex per radial dex. In a more conservative approach, we use $z = 0$ data on metallicity gradients of massive ellipticals, and study the effect of satellite accretion.

We anticipate that mergers should lower the metallicity gradients, because accreted stars, coming from lower-redshift galaxies, get deposited at high radii, and are probably more metal-rich than the stars in the envelope of the proto-elliptical. Quantitatively, the effect depends on two parameters. First, the density contrast between the merging galaxies. If lower-mass galaxies are denser, they survive the tidal field and end up in the remnant center. Conversely, if lower-mass galaxies are less dense, they will disrupt during the merger and their low-metallicity stars will get deposited at large radii, softening the pre-existing metallicity gradient.

The second parameter is the mean number of mergers undergone by a massive elliptical during its life. This number is hard to obtain observationally, since mergers of ellipticals lack the morphological distortions that would allow us to identify merger events in high-redshift samples. We can resort however to cosmological simulations, which establish the merger trees of present-day massive galaxies.

Because the satellites responsible for the change in metallicity deposit their stars in the outer parts, it is interesting to look for specific features in the metallicity profiles at the radii where accreted matter begins to be noticeable.

The merger histories simulated in Chapter 3 of this thesis to study size growth of ellipticals in a ΛCDM cosmology provide ideal models to study the effects of dry mergers on metallicity gradients of ellipticals.

4.3 Sample

We chose four remnants among our merger histories from Chapter 3 in order to have a subsample that is representative of our entire set of models. The selected merger histories are those labelled as 2, 3, 7 and 8, which cover our entire mass range from 5.21 to $2.18 \times 10^{11}\mathrm{M}_{\odot}$. In this subsample we include our most ‘active’ merger history with 8 accreted satellites (labelled “8”). The relevant quantities (masses, redshift, total metallicity) can be consulted in Table 4.1. We see that our initial primaries are assigned a nearly-Solar mean metallicity at the start of the simulation, whereas satellites are one tenth Solar or below, a reflection of the M-Z relation present at each redshift.

4.4 Observationally derived metallicity

4.4.1 Total metallicity

To set the total metallicity of our galaxies we used the values given by Vale Asari et al. (2009). In their study, Vale Asari et al. (2009) obtained the M-

Z relation at different lookback times for the same set of galaxies from the Sloan Digital Sky Survey (SDSS), using the stellar metallicities estimated with their spectral synthesis code STARLIGHT[1] (Cid Fernandes et al. 2005). Their parent sample consist of all the objects spectroscopically classified as galaxies from the Fifth Data Release of the SDSS, for which they applied the following selection criteria: $14.5 \leq m_r \leq 17.77$, z-band aperture covering factor > 20 percent, S/N ≥ 10 at 4750 rA and a narrow range in redshift $|\mathrm{z}-0.1\ | \geq 0.015$, with a central redshift of 0.1. There are 82662 objects in the resulting sample. Vale Asari et al. (2009) divided their parent sample into six present-day stellar mass bins centred in $\log M_*/\mathrm{M}_\odot = 10$, each one 0.30 dex wide for redshifts $z = 0$(t=0 Gyr), $z = 0.2$ (1 Gyr), $z = 0.7$ (5 Gyr) and 1.9 (9 Gyr). They found that as lookback time increases, the M-Z relation steepens and covers a large range of values (see their Figure 2).

4.4.2 Radial metallicity gradient

To consider a radial metallicity gradient for our model we used the observed relation between galaxy mass and radial metallicity gradients of early-type galaxies found by Spolaor et al. (2009). They measured the metallicity gradients of a sample of 51 early-type galaxies out to one effective radius by comparing nearly all of the Lick absorption-line indices to recent models of single stellar populations. In that study, Spolaor et al. (2009) found a sharp transition between the low- and high-mass regimes at a galaxy mass of $\sim 3.5\ \times 10^{10}$ M$_\odot$. Galaxies with masses smaller than this transition mass are observed to verify a clear correlation, namely their metallicity gradients become less negative and hence shallower with decreasing mass. On the other hand, above the high-mass turnover, several massive galaxies have steeper gradients, but a clear downturn from the low-mass trend is visible, marked by a broad scatter such that gradients become shallower with increasing mass, suggesting that the downturn could be a consequence of merging, and the observed scatter a natural result of merger properties. It should be stressed, though, that this radial metallicity gradients are verify by present-day early-type galaxies. Given the lack of estimations of radial metallicity gradients at high redshift, we will use these $z = 0$ radial metallicity gradients for all the galaxies. The initial metallicity gradients are listed in Table 4.1; they range from 0.2 to 0.3 dex per dex in radius.

4.5 Results and discussion

In Figure 4.1 we present the metallicity profiles for our sample. In each panel we plot the initial metallicity profile and the profile of the remnant galaxy when

---

[1] http://www.starlight.ufsc.br

TABLE 4.1— Masses, redshift and metallicity for the subsample

ID	model (1)	mass $10^{11}\ M_\odot$ (2)	redshift (3)	$[Z/H]_0$ (4)
2	progenitor	0.674	2.5	0.00
	s_1	0.22481	2.0000	-0.132
	s_2	0.35969	0.4000	0.028
3	progenitor	0.5210	2.50	-0.00768
	s_1	0.3720	0.55	0.00575
	s_2	0.1620	0.40	-0.09262
	s_3	0.5280	0.20	0.05367
7	progenitor	1.670	2.50	0.1012
	s_1	0.479	1.30	-0.0099
	s_2	0.1660	1.000	-0.1699
	s_3	1.6590	0.1000	0.1132
8	progenitor	2.180	2.50	0.1173
	s_1	0.546	1.2000	-0.0064
	s_2	0.1820	1.0000	-0.1499
	s_3	0.1940	0.8500	-0.1303
	s_4	0.1940	0.8000	-0.1283
	s_5	0.2360	0.7500	-0.0874
	s_6	0.2210	0.6000	0.0000
	s_7	0.6260	0.3500	0.03513
	s_8	0.6260	0.0750	0.0000

Note.- *Col. (1)*: identification number of the progenitor (same as Table 3.2 of Chapter **??**), *Col. (2)*: Galaxy model (progenitor or satellite), *Col. (3)*: mass of the galaxy, *Col. (4)*: redshift at which the accretion occurs, *Col. (5)*: Initial metallicity.

the merging process have ended. Metallicities are approximately linear with $\log(r)$, as found in nearby massive ellipticals (e.g. Peletier 1993). Gradients have been readily determined by linear fitting to the data points out to 40 kpc. Gradients are shown in Table 4.2.

Figure 4.1 shows that metallicity profiles are significantly shallower after the galaxy has suffered a number of mergers. Tendency already predicted by White (1980) (notice that in his work, metallicity is defined as the logarithm of the binding energy per particle in the initial “galaxy” at a given time, whereas in our case we took the metallicity from observational relationships).

Due to the unique nature of each merger history, we will discuss each panel of Figure 4.1 separately.

4.5.1 Remnant 2

This remnant, not the most massive one, undergoes the earliest merger, accreting the first satellite at $z = 2.0$ (9.895 Gyr). We see that at 100 kpc, the accretion of satellites results in a shallower metallicity gradient by a factor $\sim$

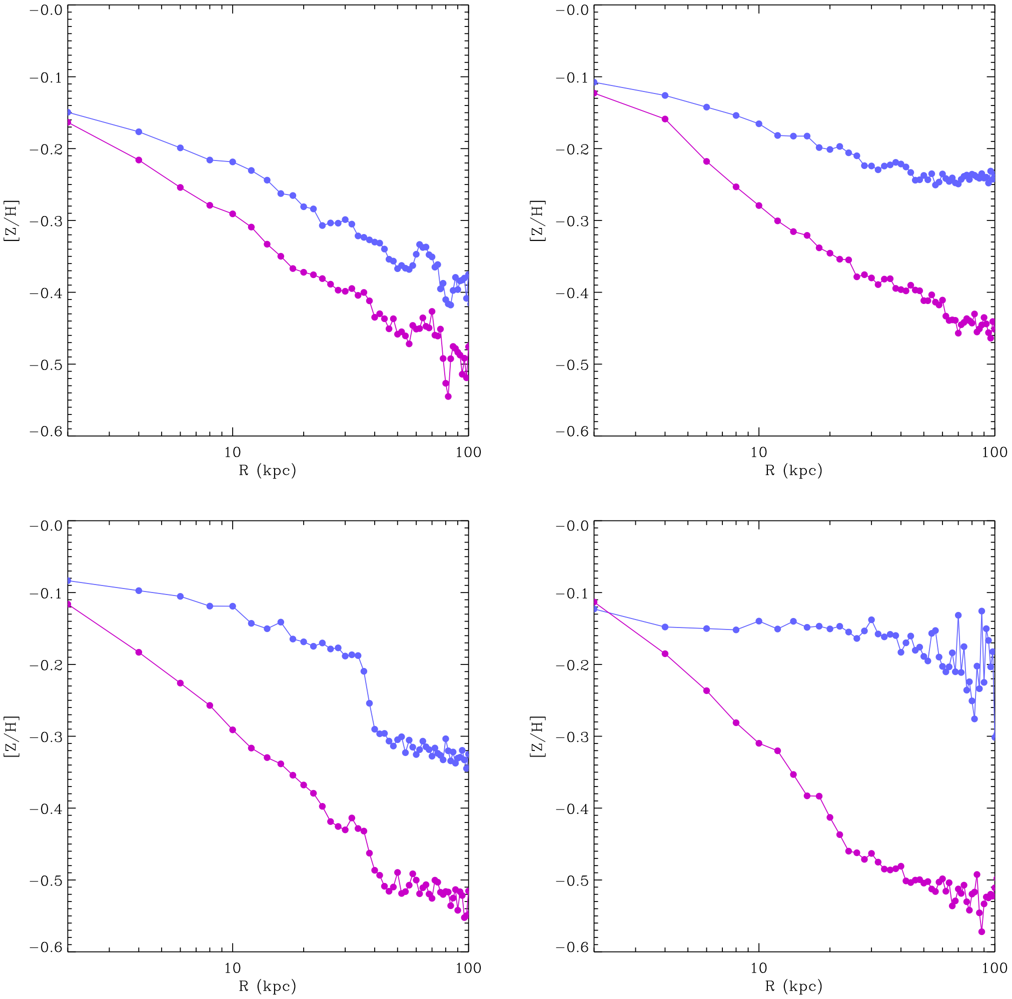

FIGURE 4.1— Metallicity as a function of the radius for 4 remnants. Upper left: remnant merger tree 2. Upper right: remnant merger tree 3. Bottom left: remnant merger tree 7. Bottom right: remnant merger tree 8. In all the panels, pink circles correspond to the initial metallicity profile and the blue circles represent the metallicity gradient of the remnant at $z = 0$.

1.26. However, notice that we are plotting up to 100 kpc, whereas the effective radius of the remnant is 3.19 kpc.

4.5.2 Remnant 3

This is our lowest mass parent galaxy. It undergoes the latest accretion of the first satellite, at $z = 0.55$. Despite its low-mass, it shows the biggest ratio between the metallicity gradients (1.91). This could be due to the fact that two of its three encounters are classified as major mergers.

4.5.3 Remnant 7

This remnant is similar to Remnant 3 in the sense that they share the same number of satellites. In this case, however, the parent-to-satellite mass ratios are grater than the regime of major and intermediate mergers of Remnant 3, which includes one mass ratio of 13:1.

4.5.4 Remnant 8

This is our more ‘active’ merger with an accretion of 8 satellites, which also has the most massive progenitor galaxy. These two aspects must be connected due to the fact that the potential well of the progenitor is the deepest among the sample. Remarkably, when accretion is taken into account, its metallicity gradient almost becomes flat.

The metallicity gradients in Figure 4.1 leads to a variation in metallicity with radius with a mean value of $\Delta[Z/H]/\log R = -0.2529 \pm 0.0493$ for the progenitors galaxies and $\Delta[Z/H]/\log R = -0.09897 \pm 0.05473$ (see Table 4.2 for the individual measurements). The mean value for the progenitors, is very similar to the found in studies of line strength gradients of early-type galaxies (e.g. Gorgas et al. 1990; Fisher et al. 1995; Sánchez-Blázquez et al. 2006). In the other hand, the mean value of our remnants is closer to the reported by Mehlert et al. (2003), in their study, they obtained a metallicity gradient of $\Delta[Z/H]/\log R = -0.10 \pm 0.12$ for their sample of 35 early-type galaxies in the Coma cluster. However, our values are lower than the predicted from dissipative and self-gravitating collapse models. For example, Larson (1974) estimated a $\Delta \log Z/\Delta \log r \sim -0.35$ and $\Delta \log Z/\Delta \log r \sim -1.0$ (Larson 1975), and Carlberg (1984) gave a $\Delta \log Z/\Delta \log r \sim -0.5$.

Gradients (Table 4.2) vary from -0.02 to -0.15. This is in agreement with our expectations. The final gradients are within, but on the shallow side, or the range observed in today’s massive ellipticals (Sánchez-Blázquez et al. 2007). This shows that our results are consistent with proto-galaxies with steeper metallicity gradients. However, our values are lower than the predicted from dissipative and self-gravitating collapse models. The final metallicity gradients are on average a factor $\sim 40\%$ of the initial $\nabla[Z/H]$.

TABLE 4.2— Metallicity gradient of the remnants and progenitors galaxies.

model (1)	$\nabla[Z/H]$ progenitor (2)	$\nabla[Z/H]$ remnant (3)
2	-0.2035 ± 0.0040	-0.1493 ± 0.0081
3	-0.2224 ± 0.0079	-0.0994 ± 0.0042
7	-0.2739 ± 0.0086	-0.1243 ± 0.0195
9	-0.3119 ± 0.0083	-0.0227 ± 0.0063

Note.- *Col. (1)*: label of the merger experiment, *Col. (2)*: metallicity gradients for the progenitors galaxies, *Col. (3)*: metallicity gradients for the remnants.

4.6 Conclusions

We have estimated the metallicity gradients of a representative subsample of our merger histories from Chapter 3 in order to examine whether we can reproduce the metallicity gradients observed in present-day elliptical galaxies by following observational mass-metallicity relationships for our cosmological-motivated dry mergers remnants.

We find that the metallicity profiles are approximately linear with $\log(r)$, and that the effect of accreting satellites is to produce a shallower metallicity gradient. The final gradients are consistent with those observed in $z = 0$ massive ellipticals. A high number or sequential accretions tend to produce a smoother metallicity gradient than fewer merger events, even when the total accreted mass is approximately the same. We also note a large scatter in the observed gradients, which scales with the number of sequential accretions, which is compatible with the large scatter in metallicity gradients observed in massive ellipticals.

The derived values in the current study are consisted with the extant in the literature. Our results show that, just from the the fact that merger-driven mixing is incomplete and the preference for mass deposition in the outer parts, the combined effect of mergers between $z = 2$ and $z = 0$ is to flatten the metallicity profile so that the final gradient is ~40% of the gradient at $z \sim 2$.

4.7 Future work

At present, individual measurements of metallicity gradients ($\nabla_{[\mathrm{Fe/H}]}$) for early-type galaxies are widely spread, ranging from $-0.54 < \nabla_{[\mathrm{Fe/H}]} < +0.2$ (Koleva et al. 2011). In this respect, Forbes et al. (2005) found that in general lower mass galaxies have shallower gradients, such trend being consistent with monolithic collapse models (Kawata 1999; Kawata & Gibson 2003; Chiosi & Carraro 2002) which invoke gas dissipation and energy injection, and it is also compatible with the galactic winds of Martinelli et al. (1998). Additionally, Mehlert et al. (2003) and Sanchez-Blazquez (2004) found typical gradients that are more consistent with the monolithic collapse formation models, suggesting that the dominant mechanism for old, early-type Coma galaxies is the monolithic collapse.

On the other hand, Ogando et al. (2005) found that higher mass galaxies scatter vertically in the metallicity-gradient versus velocity dispersion diagram, indicating a contribution by both formation processes (monolithic collapse and hierarchical clustering) and giving observational support to a hybrid formation scenario among massive galaxies (Kormendy 1989; Kobayashi 2004). However, Pipino et al. (2010) argued that such behavior can be explained with different efficiencies of star formation in the framework of the revised monolithic formation scenario, hence the scatter in the observed gradients should not be used as an evidence of the need of mergers. They also claimed that in order to explain the scatter observed by Ogando et al. (2005) and Spolaor et al. (2009) with the effects of dry mergers one can accommodate only a few of such episodes, otherwise we would observe only galaxies with flat gradients, or that galaxies require to undergo mergers with galaxies with steepest gradients, leading to the necessity of even steeper gradients than the ones of the early monolithic collapse models (Larson 1974).

From our study we have shown that within the hierarchical clustering scenario for galaxy formation it is possible to generate metallicity gradients which are compatible with observations, whilst considering the above-mentioned studies and the ones in sections 4.5 and 4.1, it is clear that there is a large scatter in the measurements of the metallicity gradients and that the validity of the monolithic collapse, the hierarchical clustering or a hybrid formation scenario in terms of metallicity gradient remains unclear. Therefore, it will be useful to expand our study to analyse with a statistically meaningful sample the differences in the final metallicity gradient due to initially steep, shallow or non-existent, radial metallicity gradients, as well as account for the different number and kind of mergers that the galaxy undergoes. Our full sample of merger histories in Chapter 3 are an excellent benchmark to better define the metallicity-mass gradient correlation for the early-type galaxies.

5

Minor mergers and disc thickening

Minor mergers, when occurring onto disc galaxies, leave strong signatures in the parent disc, including transient spirals, bars, tidal tails, star formation, and disc thickening (e.g Athanassoula et al. 1997; Bournaud & Combes 2004; Combes 2009). Understanding the effects of minor mergers on the thickness of spiral discs is useful as a means of providing observational checks on the amount of merging predicted in ΛCDM-based galaxy formation models. Minor mergers contribute to disc thickening through two mechanisms: injection of vertical mechanical energy on the pre-existing thin disc, and deposition of satellite matter onto a thick-disc configuration. In this chapter we study the effects of minor mergers on disc thickening, focussing on quantifying the effects of numerical heating. We perform a suite of merger experiments of the single accretion of one satellite onto a disc galaxy, using a range of mass ratios, orbital types and number of particles. We find that both thickening mechanisms do operate in concordance. Retrograde orbits lead to more pronounced thickening than direct orbits, despite the stronger resonant coupling of prograde orbits. The scale height of accreted matter is higher than that of pre-existing disc matter. The relative importance of heating versus mass deposition cannot be ascertained with the present experiments.

5.1 Introduction

Mergers between a large disc and small companions are far less destructive than those involving comparable-mass galaxies. In fact, such events may simply increase galaxy masses slowly while not violently disturbing discs (Quinn et al. 1993).

The discs of disc galaxies contain a substantial fraction of the baryonic matter and angular momentum of the system, and much of the evolutionary activity in these galaxies, such as the formation of stars, spiral arms, bars and rings, and the various forms of secular evolution, takes place in their discs.

Thick discs constitute a ubiquitous component of disc galaxies (see Dalcanton & Bernstein 2002; Yoachim & Dalcanton 2006), though their formation is not yet understood (van der Kruit & Freeman 2011). At least four scenarios have been invoked for thick disc formation (Combes 2011): (i) by means of the accretion and disruption of satellites (e.g. Abadi et al. 2003b), (ii) the thickening of a pre-existing thin disc through a minor merger (e.g. Villalobos & Helmi 2008; Kazantzidis et al. 2008; Villalobos & Helmi 2009; Di Matteo et al. 2011), (iii) radial migration via resonant scattering, i.e., migration of stars from the inner disc that significantly thicken the disc when it is seen edge-on (e.g.Roškar et al. 2008; Minchev et al. 2012) (iv) by *in-situ* formation from thin gas disc (e.g. Brook et al. 2005; Bournaud et al. 2007) or small amounts of star formation in the warp structure (Roškar et al. 2010).

All the above mechanisms are compatible with the structure of the Milky Way thick disc. However, they all imply a very different behavior for the early evolution of disc galaxies. The first case suggests that discs can form entirely from merging subunits in spite of their highly ordered present-day structure. In the second case, discs form largely through smooth gas accretion that is occasionally punctuated by minor merging events. A third scenario suggests either that discs form primarily through smooth monolithic collapse, with thick-disc stars precipitating out of the collapsing gas cloud (case iii, Eggen et al. 1962), or that the thick disc forms from a disc of gas that has been energetically heated by star formation (case iv, Kroupa 2002).

Minor mergers contribute to the growth of a thick disc through two qualitatively different different mechanisms. In the first case, thick-disc stars form in external galaxies and are subsequently deposited by accretion events at large scale heights (e.g. Abadi et al. 2003b; Yoachim & Dalcanton 2005). In the second case, thick-disc stars form initially in the thin disc and are then dynamically heated to large scale heights by encounters with orbiting satellites (e.g. Quinn et al. 1993; Walker et al. 1996; Robin et al. 1996; Velazquez & White 1999; Chen et al. 2001; Aguerri et al. 2001).

Kazantzidis et al. (2008), by means of dissipationless N-body simulations, investigated the cumulative effect of substructure impacts onto thin disc galaxies in the context of the ΛCDM paradigm. They suggested that at least part of a galaxy's thick-disc component may plausibly originate from the gravitational interaction between an existing thin disc and infalling satellites with mass functions, density structures, and orbital distributions of the kind expected in the ΛCDM paradigm of structure formation. CDM substructure increases the scale height of stellar discs and should be regarded as being at least partially responsible for the origin of thick discs. Their conclusion is supported by observational studies of the vertical distribution of stars in the Milky Way (Chen et al. 2001) and star count data from a number of Galactic sample fields (Robin et al. 1996). In contrast, other “thin-thick” disc kinematic studies favour models in which the thick disc forms from direct accretion of stars from infalling satellites (e.g. Yoachim & Dalcanton 2005, 2006). As argued by these authors, the detection of very slowly rotating or counterrotating thick discs supports an accretion origin for thick-disc stars.

All N-body studies of merger-induced disk thickening need to deal with a specific technical problem - the numerical heating of the disk. Even when evolved in isolation, N-body galaxy disks thicken as a result of numerical heating (errors in the integration of the particle orbits), and as a result of 2-body relaxation (orbit migration due to the graininess of the potential). The latter may translate into mass segregation (energy gains by disk particles from close encounters with the, usually more massive, halo particles). The 2-body relaxation process may be quantified as the inverse of the 2-body relaxation time $\tau_{2\mathrm{B}}$. For a gravitating system of N particles, $\tau_{2\mathrm{B}}$ increases with particle number:

$$\tau_{2\mathrm{B}} \sim \frac{0.1\,N}{\ln N\,\tau_{\mathrm{cr}}} \tag{5.1}$$

hence the 2-body relaxation effects can be decreased by increasing the number of particles in the simulation and it is inversely proportional to the crossing time (τ_{cr}) (Binney & Tremaine 2008).

A second difficulty in many of the N-body studies of minor mergers to date arises from an arbitrary choice of density contrast between the main galaxy and the merging satellite. A lower density satellite is more prone to disruption by the primary tidal field: the truncation radius r_{t} of a sphere M_2 orbiting at a distance D near a larger sphere M_1 is given by equating M_2's gravity to M_1's tidal force:

$$\frac{M_2}{r_{\mathrm{t}}^2} \approx \frac{M_1}{D^3}\,r_{\mathrm{t}} \tag{5.2}$$

hence

$$\frac{M_2}{r_{\mathrm{t}}^3} \approx \frac{M_1}{D^3} \tag{5.3}$$

which means that the tidal radii of higher-density satellites fall outside the satellite, whereas in lower-density satellites the tidal radius falls inside the satellite, leading to mass loss and, possibly, disruption.

The satellite mass loss and disruption affect merger experiments of disk thickening in two ways. First, the disruption rate determines at what radii do the accreted stars get deposited. High-density satellites spiral in, undisrupted, and deposit their stars in the remnant center, whereas low-density satellites disrupt as they spiral in, leading to the deposition of satellite mass at intermediate radii. Second, the disruption rate determines the damage that the merging satellite causes on the pre-existing disc. As the satellite mass decreases due to tidal stripping its heating effect on the disc decreases. Hence, for a study of thick disc formation, a realistic choice of densities is essential.

5.2 Motivation

In preparation for addressing the astrophysical questions outlined in § 5.1, we believe it is pertinent to address some of the more technical aspects outlined above, such as the dependency of the results on disc heating on the number of particles, and the adequate treatment of the density contrast between the merging galaxies.

In this chapter, we present a suite of N-body simulations of the accretion of a single satellite onto a disc galaxy. A set of models covering a range of mass ratios and merging orbits are rendered with numbers of particles ranging from a few hundred thousand to nearly two million. The disc thickness after the merger is analyzed taking into account the contributions of accreted material and pre-existing thin disc material. Care is taken to quantifying the varying amount of disc thickening that arises from two-body effects, by running disc galaxy models in isolation.

5.3 Galaxy model

5.3.1 Building of the galaxy model

We use the galaxy model building package GalactICS[1] (Kuijken & Dubinski 2011), which generates N-body realizations of axisymmetric galaxy models including disc, bulge and halo. This code computes the gravitational potential for a given mass model by calculating the distribution function of each component independently. The disc distribution function is a generalization to three dimensions of the planar model devised by Shu (1969). The bulge has the distribution function of King (1966), whereas the halo has a lowered Evans distribution (Kuijken & Dubinski 1994). These distribution functions have a unique density for each of the components in any given potential. Since the three components are gravitationally affecting each other, a numerical solution

---

[1] http://adsabs.harvard.edu/abs/2011ascl.soft09011K

for the Poisson equation is required to make the models self-consistent. For a full description see Kuijken & Dubinski (1995).

Bulge distribution function

For the bulge distribution function (DF) we take a King model (King 1966). This DF has the form:

$$f_{\mathrm{bulge}}(E) = \begin{cases} \rho_{\mathrm{b}}(2\pi\sigma_{\mathrm{b}}^2)^{-3/2}\mathrm{exp}[(\psi_0 - \psi_{\mathrm{c}})/\sigma_{\mathrm{b}}^2]\{\mathrm{exp}[-(E-\psi_{\mathrm{c}})/\sigma_{\mathrm{b}}^2] - 1\}, & \text{if } E < \psi_{\mathrm{c}} \\ 0, & \text{otherwise.} \end{cases} \tag{5.4}$$

It depends on the three parameters ψ_{C} (the cutoff potential of the bulge), ρ_{b} (approximately the central bulge density, ignoring the effects of the DF truncation) and σ_{b}, which governs the velocity dispersion of the bulge component. ψ_0 is the gravitational potential at the center of the model.

Halo distribution function

The halo has a DF of the lowered Evans distribution (Kuijken & Dubinski 1994). This DF is based in the model of Evans (1993) and is written as:

$$f_{\mathrm{halo}}(E, L_z^2) = \begin{cases} [(AL_{\mathrm{z}}^2 + B)\exp(-E/\sigma_0^2) + C][\exp(-E/\sigma_0^2) - 1], & \text{if } E < 0. \\ 0, & \text{otherwise.} \end{cases} \tag{5.5}$$

The halo has five free parameters: the specific angular momentum (L_{z}), the potential well depth ψ_0, the velocity and density scales σ_0 and ρ_1, the halo core radius R_{c} and the flattening parameter q. The last three parameters are contained within the parameters A, B and C; L_{z} represents the specific angular momentum in the direction in which the model is flat. The halo has a tidal radius specified by $E = 0$.

Disc distribution function

The DF for the disc is an extension of the planar DF of Shu (1969) into the vertical dimension, similar to the DF constructed by Binney (1987):

$$f_{\mathrm{disc}}(E_{\mathrm{P}}, L_{\mathrm{z}}, E_{\mathrm{z}}) = \frac{\Omega(R_{\mathrm{c}})}{(2\pi^3)^{1/2}\kappa(R_{\mathrm{c}})} \frac{\tilde{\rho}_{\mathrm{d}}(R_{\mathrm{c}})}{\tilde{\sigma}_{\mathrm{R}}^2(R_{\mathrm{c}})\tilde{\sigma}_{\mathrm{z}}^2(R_{\mathrm{c}})} \exp\left[-\frac{E_{\mathrm{p}} - E_{\mathrm{c}}(R_{\mathrm{c}})}{\tilde{\sigma}_{\mathrm{R}}^2(R_{\mathrm{c}})} - \frac{E_{\mathrm{Z}}}{\tilde{\sigma}_{\mathrm{z}}^2(R_{\mathrm{c}})}\right] \tag{5.6}$$

In this equation, $E_\mathrm{p} \equiv E - E_\mathrm{z}$ is the energy in planar motions, L_z is the specific angular moment about the axis of symmetry, R_c and E_c are the radius and energy of a circular orbit with angular momentum L_z, and Ω and κ are the circular and epicyclic frequencies at radius R_c.

The distribution functions for the various galaxy components all imply a unique volume density $(\rho_\mathrm{bulge}, \rho_\mathrm{disc}, \rho_\mathrm{halo})$ in a given potential $(\Psi(\mathrm{R}, \mathrm{z}))$. To construct a self-gravitating model, the potential is found by solving Poisson's equation using a spherical harmonic expansion, following Prendergast & Tomer (1970):

$$\nabla^2\Psi(\mathrm{R}, \mathrm{z}) = 4\pi\mathrm{G}\left[\rho_\mathrm{disc}(\mathrm{R}, \Psi, \Psi_\mathrm{z}) + \rho_\mathrm{bulge}(\Psi) + \rho_\mathrm{halo}(\mathrm{R}, \Psi)\right] \tag{5.7}$$

5.3.2 Parameters of the model

The choice of parameter values is based on the model "A" by Kuijken & Dubinski (1995), in which the core radius of the King model is 0.15 and the concentration parameter is taken to be 6.7. The radial and vertical densities of the disc are exponential, with a scale length $h_\mathrm{D} = 1.0$ and a scale height of $z_\mathrm{D} = 0.1$, and it extends to 5.0 length units. The cited model establishes a velocity dispersion in the disc such that it has a Toomre's stability parameter of $Q = 1.7$, high enough to prevent bar instabilities when evolving in isolation. A gravitational constant of $G = 1$ is used, the length unit is the disc scale length, and the total mass of the galaxy is equal to 6.44 units.

Units

Our galaxy model matches a Milky Way galaxy when the units of length, velocity and mass are the following:

- unit of length = 4.5 kpc
- unit of velocity = 220.75 $\mathrm{km\,s^{-1}}$
- mass = $5.1 \times 10^{10} M_\odot$
- time unit = 20.5 Myr

5.3.3 Satellite galaxy

The satellite is also a three component model with a disc, bulge and a halo, built as a scaled replica of the primary. In order to have satellites with realistic relative densities we have imposed that they fulfill the Tully-Fisher relation.

Following González-García & Balcells (2005), we have that homologous galaxies with the same mass ratio satisfy $L \propto V^{\alpha_{TF}}$ when the radius and masses (R) and (M), are scaled as:

$$R \propto M^{\left(1-\frac{2}{\alpha_{TF}}\right)}, \tag{5.8}$$

$$\rho \propto M^{\left(\frac{6}{\alpha_{TF}}-2\right)}. \tag{5.9}$$

We have chosen a Tully-Fisher index of 3.5 for all of our models.

5.3.4 Set of main galaxies

One of the goals of our study is to characterise the differences in physical properties due to a higher numerical resolution. Thus, we built three different sets of galaxy-satellite models: one with N=185,000 particles; one with $3N$ (555,000 particles); finally, one with $10N$ (1,850,000). The three models have the same mass for each component: 0.42, 0.82 and 5.20 for the bulge, disc and halo, respectively. Also, the same scale length ($h_{\rm D}$ = 1.0) and scale height ($z_{\rm D}$ = 0.1). The number of particles and mass for each galaxy and component can be seen in Table 5.1.

TABLE 5.1— Masses and number of particles for the three galaxy models

N_p (1)	D1 (2)	B1 (3)	H1 (4)	D2 (5)	B2 (6)	H2 (7)	$M_{\rm B}$ (8)	$M_{\rm D}$ (9)	$M_{\rm H}$ (10)	$m_{\rm B1}$ (11)	$m_{\rm D1}$ (12)	$m_{\rm H1}$ (13)
185	40	10	90	10	5	30	0.42	0.82	5.20	4.2×10^{-5}	2.05×10^{-5}	5.7×10^{-5}
555	120	30	270	30	15	90	0.42	0.82	5.20	1.4×10^{-5}	6.83×10^{-6}	1.92×10^{-5}
1850	400	100	900	100	50	300	0.42	0.82	5.20	4.2×10^{-6}	2.05×10^{-6}	5.77×10^{-6}

Note.- *Col. (1)*: Total number of particles ($\times10^3$), *Col. (2)*: disc particles of the main galaxy ($\times10^3$), *Col. (3)*: Bulge particles of the main galaxy ($\times10^3$), *Col. (4)*: Halo particles of the main galaxy ($\times10^3$), *Col. (5)*: disc particles of the satellite ($\times10^3$), *Col. (6)*: Bulge particles of the satellite ($\times10^3$), Col. (7): Halo particles of the satellite ($\times10^3$). *Col. (8)*: Bulge mass of the main galaxy, *Col. (9)*: disc mass of the main galaxy, *Col. (10)*: Halo mass of the primary, *Col. (11)*: mass of a bulge particle, *Col. (12)*: mass of a disc particle, *Col. (13)*: mass of a halo particle.

The three constructed models have almost the same central velocity dispersion and the same velocity. For illustration purposes, in Figure 5.1 we show the rotation curve and the velocity dispersion for the model with the highest number of particles (edge-on view, projected quantities). The measurements were taken as described in § 5.6 using a slit along the major axis of 4 units of length and 0.1 units of width.

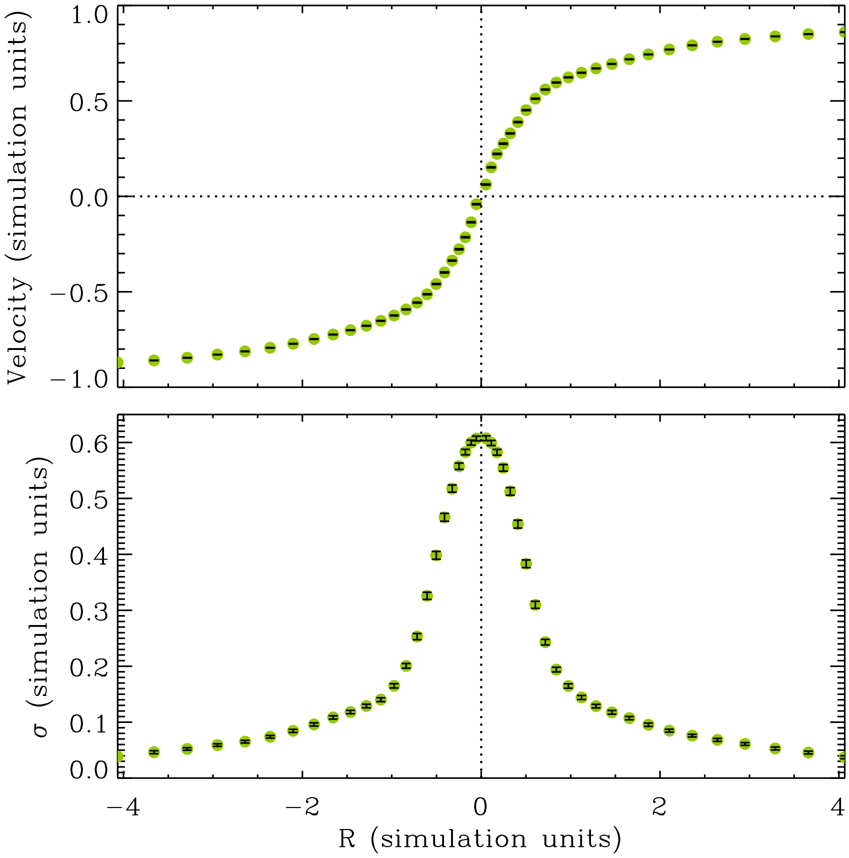

FIGURE 5.1— Velocity dispersion and rotation curve of the main galaxy with 1,400,000 particles. The rotation curve was measured in a edge-on view, whereas the velocity dispersion was measured face-on. The values are expressed in an arbitrary set of units where G=1, V=1, R=1.

In Figure 5.2 we show the stellar surface density profile of one main galaxy (seen in a face-on view). The profile resembles the typical profile of a disc galaxy with a prominent bulge ($\sim$ 1 unit length) and a disc that extends to a radius that is larger than the disc extension (which is 5 length units). Figures 5.1 and 5.2 show that in our models the bulge dominates the observed density and vertical velocity dispersion throughout the central region out to 1 disc scale length.

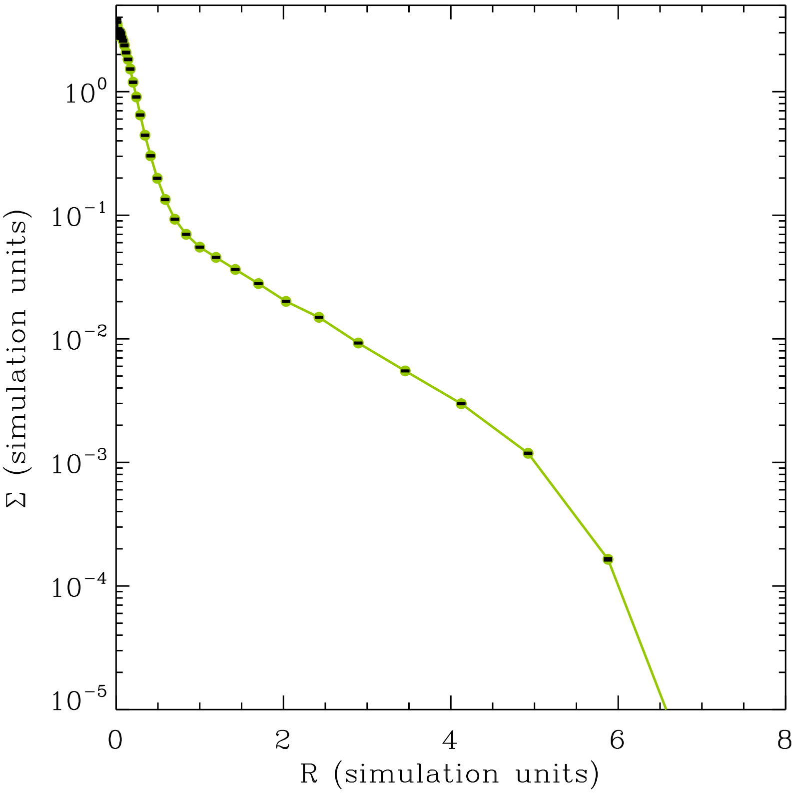

FIGURE 5.2— Stellar surface density profile of the main galaxy with the highest resolution, corresponding to the galaxy-satellite system with $10N$ particles. The values are expressed in an arbitrary set of units where G=1, V=1, R=1.

5.4 Suite of models

For our merger experiments we have chosen two models of Eliche-Moral et al. (2006) (hereafter EM06), labelled as M2TF35D and M3TF35D. For the sake of comparison, we will use the same notation. The code for our simulations is the following: MmTFα_{TF}[D/R], where M refers to the word 'mass', m gives the bulge-to-satellite mass ratio, α_{TF} indicates the used Tully-Fisher exponent (e.g., TF35 for $\alpha_{TF} = 3.5$) and the letters "D" and "R" denote a direct ("D") or a retrograde orbit ("R"), respectively.

5.4.1 Orbital parameters

We have used the coordinate system and orbital parameters of EM06. In this coordinate system, the initial merger orbit at the beginning of the simulation lies in the XY plane and the satellite lies on the +X axis with its orbital angular momentum pointing towards +Z.

The orientations of the disc spins in standard spherical coordinates are (θ,ϕ), where the subindexes 1 and 2 denote the angles of the primary and the satellite, respectively. For the direct orbit, $\theta_1 = 30°$, and for the retrograde, $\theta_1 = 150°$. In both cases, $\phi_1 = 0°$, $\theta_2 = 25°$, $\phi_2 = 90°$. Initial orbits were elliptical, with apocentre equal to twice the disc outer radius ($\sim$ 15 length units) and pericentre equal to the disc scale length ($\sim$ 1 length unit).

Considering two mass ratios, two types of orbits, a single α_{TF} and three galaxy models, we have a total of 12 different merger experiments. Given that these share some properties, we can band them together in four big groups, each containing the three different number of particles, namely N, $3N$ and $10N$. Using the notation described above, these groups are: M2TF35D (formed by M2N1850D, M2N555D and M2N185D), M2TF35R (formed by M2N1850R, M2N555R and M2N185R), M3TF35D (formed by M3N1850D, M3N555D and M2N185D) and M3TF35R (formed by M3N1850R, M3N555R and M3N185R). Since all the orbits were set up using $\alpha_{TF} = 3.5$, we have replaced "TF35" with "N+number-of-particles/10^3" to name the individual cases. See Table 5.2.

TABLE 5.2— Orbital parameters of the merger experiments separated by groups

$G_{\rm model}$ (1)	MR_1 (2)	MR_2 (3)	$R_{\rm S}/R_{\rm P}$ (4)	$L_{z,0}$ (5)	e (6)	$R_{\rm peri}$ (7)	$V_{\rm peri}$ (8)	θ_1 (9)	$t_{\rm tot}$ (10)
M2TF35D	1/2	1/6	0.46	0.4815	0.907	0.73	1.981	30	150
M2TF35R	1/2	1/6	0.46	0.4815	0.907	0.73	1.981	150	150
M3TF35D	1/3	1/9	0.39	0.3532	0.900	0.79	1.793	30	200
M3TF35R	1/3	1/9	0.39	0.3532	0.900	0.79	1.793	150	200

Note.- *Col. (1)*: group of model, *Col. (2)*: mass ratio between the luminous mass of the satellite and the bulge mass of the primary, *Col.(3)*: initial mass ratio between the luminous matter of the satellite and the luminous mass of the primary galaxy, *Col. (4)*: initial ratio between the half-mass radii of the satellite and the primary galaxy, *Col. (5)*: initial angular momentum of the orbit in simulations units, *Col. (6)*: orbit eccentricity, *Col. (7)*: distance between the two galaxies at the pericentre in simulations units, *Col. (8)*: velocity at the pericentre passage in simulation units, *Col. (9)*: initial angel between the angular momentum of the orbit and the spin of the disc of the primary galaxy, *Col. (10)*: total time in simulations units.

5.5 Computational details

5.5.1 Runs

The simulations were executed in the Lapalma cluster[2]. For all the simulations, a force accuracy parameter of 0.005 was used, sufficient to protect against big errors in the force calculation, and a tolerance in the time accuracy of 0.02, which in combination with the maximum and minimum range in the time step (0.1 and 0.001, respectively) guarantees a good time integration. We set an unequal softening for all components: 0.5 for the halo particles, 0.2 for the disc and 0.1 for the bulge. Each simulation took an average wall-clock-time of 36 hours. In the Appendix B there is an example of a GADGET-2 parameter input file.

Prior to the beginning of the simulations, each galaxy model was allowed to evolve in isolation for 21 simulation steps, which correspond approximately to 430 Myr. For these simulations, we set an equal softening length of 0.02 for all the components, which is smaller than the value used for the merger experiments.

5.6 Methods

In this section, we explain how we have measured the physical properties of the models.

5.6.1 Vertical distribution

To measure the vertical distribution, we first put the galaxy model center in the origin of coordinates in an edge-on view. Then we define four fixed radial positions that are a fraction of the chosen total length (r_{max}, which is usually a factor of the disc length) as $R = r_{\mathrm{max}}/10$, $R = r_{\mathrm{disc}}/6$, $R = r_{\mathrm{max}}/3$ and $R = r_{\mathrm{max}}$. Finally, we define a radial bin of width 0.03 and measure the mass-weighted median z-coordinate of the particles at each fixed radius.

Numerical thickening of the disc

To characterise the thickening of the disc, it is necessary to estimate the contribution of the numerical thickening that is produced by the artificial relaxation of the system and by the numerical heating at short temporal scale (inherent

---

[2] One node of the *Red Española de Supercomputación* which is located at the *Centro de Astrofísica de La Palma* (CALP) in the Canary Island. This supercomputer of 512 CPUs PowerPc 970FX at 2.2 Ghz runs under the linux platform and provides a total of 14 TB of data storage.

consequence of the discreteness of the potential in the N-body system). To estimate this correction, we will follow Eliche-Moral et al. (2006) in assuming that the two-body effect and the merger dynamics independently contribute to the energy injection into the vertical direction of the disc. Two-body vertical heating of discs is dominated by interactions with the primary halo particles, which should not vary greatly if the disc is being thickened by the satellite accretion; meanwhile, the accretion-driven injection of vertical kinetic energy onto the disc should not change significantly under small variations of the disc thickness produced by the halo-disc two-body effect. Then, we have:

$$K_{\mathrm{z,simul}} = K_{\mathrm{z,initial}} + \Delta K_{\mathrm{z,2B}} + \Delta K_{\mathrm{z,merging}}, \tag{5.10}$$

or

$$\sigma^2_{\mathrm{z,simul}} = \sigma^2_{\mathrm{z,initial}} + \Delta\sigma^2_{\mathrm{z,2B}} + \Delta\sigma^2_{\mathrm{z,merging}}, \tag{5.11}$$

where K_{z} denotes vertical kinetic energy, σ_z is the vertical velocity dispersion and the subindexes *simul, initial, 2B, merging*, stand for: final measured value, initial measured value, two-body contribution, merger contribution merger, respectively.

Because the discs are approximately isothermal in the vertical direction (Spitzer 1942; van der Kruit & Searle 1981), $h_{\mathrm{z}} = \sigma_{\mathrm{z}}/\left(2\pi G\rho_0\right)^{1/2}$, where ρ_0 is the central disc density. In the regime of low mass accretion, valid in the present experiment, vertical disc surface density is conserved, i.e. $\mu \propto \rho h_{\mathrm{z}} = \mathrm{const.}$; hence, $h_{\mathrm{z}} \propto \sigma^2_{\mathrm{z}}$ and equation (5.11) becomes:

$$h_{\mathrm{z,simul}} = h_{\mathrm{z,initial}} + \Delta h_{\mathrm{z,2B}} + \Delta h_{\mathrm{Z,merging}} \tag{5.12}$$

The quantity we are after is $h_{\mathrm{z,merging}}$. Thus, with these approximations, thickening effects accrue linearly:

$$\Delta h_{\mathrm{z,merging}} = \Delta h_{\mathrm{z,simul}} - \Delta h_{\mathrm{z,2B}}, \tag{5.13}$$

which is equivalent to:

$$h_{\mathrm{z,merging}} = h_{\mathrm{z,simul}} - \Delta h_{\mathrm{z,2B}}, \tag{5.14}$$

where $h_{\mathrm{z,simul}}$ is the raw measurement and $\Delta h_{\mathrm{z,2B}}$ can be considered as the measurement given by the progenitor galaxy when it evolves in isolation for the complete duration of the simulation.

As the vertical distribution will be calculated using the weighted median of the z axis, we will refer to it as:

$$\mid z \mid_{\mathrm{merging}} = \mid z \mid_{\mathrm{simul}} - \Delta h_{\mathrm{z,2B}} \tag{5.15}$$

5.6.2 Separation distance

To estimate the separation distance between the primary galaxy and the satellite, we measure the relative distance between the medians of the mass distribution of the bulges at each snapshot.

5.6.3 Surface density

To measure the surface density, first we put the galaxy model in a face-on view and select a maximum coordinate ($r_{\rm max}$) at which we will measure. Next, we define a linearly-spaced grid of logr values, between an minimum $\log r = 0.01$ and $r_{\rm max}$; then we find the projected coordinates, the cumulative mass $M_{\rm cum}$ and calculate $M^i_{\rm cum}/\pi * ((x^i_{\rm proj})^2 + (y^i_{\rm proj})^2)$ for each i particle.

5.6.4 Rotation curve

The rotation curve is calculated trying to mimic the way the observers does, i.e. placing a “slit” along the galaxy major axis of length equivalent to the disc length, with a width which is a factor of the disc scale length. Then the material contained in the slit is divided in 50 logarithmically-spaced intervals. In each interval, the median of the projected velocity of the particles is calculated an taken as mean velocity. The root mean square of the distribution of projected velocities is taken as the velocity dispersion. Velocities and dispersions are smoothed by convolving with a kernel of width 2 spatial bins. Velocity and dispersion errors are estimated as the width of the distribution divided by the square root of the number of particles in the bin. This recipe tends to overestimate the errors; we find that division by $5^{1/2}$ approximately corrects for this overestimate, and we apply this correction factor.

5.7 Results

The evolution of our models follow the typical behavior of the merger between two discs with different mass, described with great detail since the first simulation work of Toomre & Toomre (1972). After the first pericentre passage, tidal tails and bridges appear connecting the galaxy and the satellite, and the disc of the primary develops distortions and spiral patterns. The disc of the primary galaxy experienced thickening, consistent with all merger simulations. At the end of the simulation, the material of the satellite is distributed unevenly throughout the disc of the primary galaxy. A fraction of the satellite material reached the center of the remnant, though it mostly settled down at the outer radii.

5.7.1 Surface density profile

In Figure 5.3 we show the face-on surface density profile of our merger experiments with the highest numerical resolution, separated by its mass ratio and type of orbit. We see that, in general, the accretion of a satellite results in a reduction of the surface density at the innermost radii and an increase of the surface density at the most external radii ($R \gtrsim 15$ kpc), the latter being more acute for the direct orbits. This reflects the stronger spin-orbit coupling of direct orbits.

5.7.2 Vertical distribution

The discs of all our remnants show higher vertical scales than the discs of the initial galaxies. To quantify the disc thickening due to accretion of a satellite we have measured the final vertical distribution of *i*) the total luminous material, *ii*) the material originally belonging to the primary disc, *iii*) that originally belonging tho the disc of the satellite, and *iv*) that originally belonging to the bulge of the satellite.

In Figure 5.4 we show the measurements of the vertical distribution calculated as described in section 5.6. We have considered $r_{max} = 5$ for all the components, which corresponds to the initial disc length. Thus, the smallest two fixed radii give us an estimation of the vertical distribution of the inner disc, which is affected by the bulge, whereas the third fixed radius provides information about the outer disc and the largest of the outskirts that are heavily affected by the merging process. The data have been plotted separately according to the fixed radii at which they have been measured. In all the plots, the red triangles correspond to the total luminous matter (i.e., discs and bulges of the primary and satellite), the blue asterisks to the disc of the primary galaxy, the lime-green open diamonds to the disc of the satellite, and the orange filled circles to the bulge of the satellite. If we follow the vertical distribution of the luminous material, we can see that it is very similar to the primary disc, as expected for a minor merger accretion. Also expected, the satellite disc shows the highest vertical distribution due to its disruption. Now, if we focus on the experiment groups, we see that the retrograde cases exhibit larger vertical distributions than the direct cases, but when we consider the different number of particles we do not observe a clear trend between them.

Figure 5.4 shows the raw measurements, which are affected by the contribution of the initial vertical distribution and by the numerical thickening due to the code performance (the $\Delta h_{\mathrm{z,2B}}$ is defined in Section 5.6). To correct our values from the numerical thickening, we have simulated the three primary galaxies in isolation (see Table 5.1 for the particles allocation) for the whole

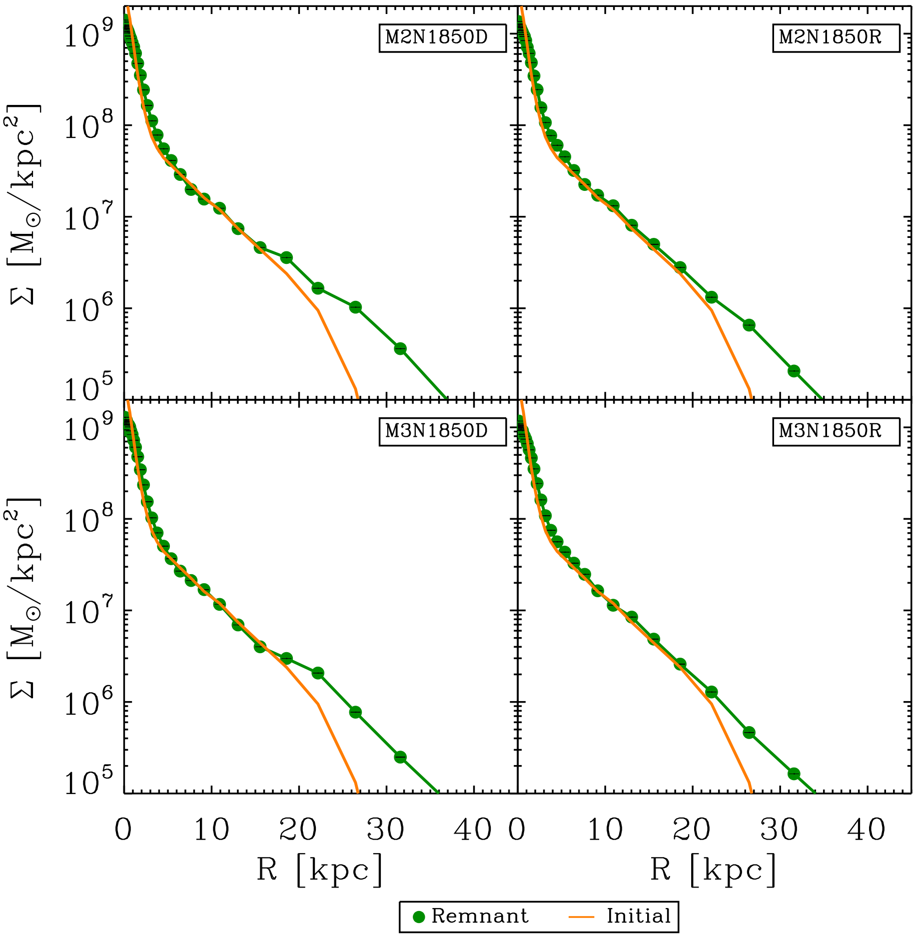

FIGURE 5.3— Face-on stellar surface density profiles of the remnants with the highest numerical resolution separated by its mass ratio and type of orbit. The orange lines correspond to the surface density of the main galaxies at the beginning of the simulations and the filled green circles to the total luminous matter of the remnants at the end of the simulation.

simulation time and we have measured the vertical distribution in the same way as the merger experiments.

In Figure 5.5 we show the $\Delta h_{\mathrm{z,2B}}$ of the three primary galaxy discs separated by model an by radius. The green filled circles correspond to the primary galaxy with the lowest number of particles (which in addition to the satellite particles will form a system with $N = 185,000$ particles); the orange filled circles correspond to the primary galaxy which has three times more particles

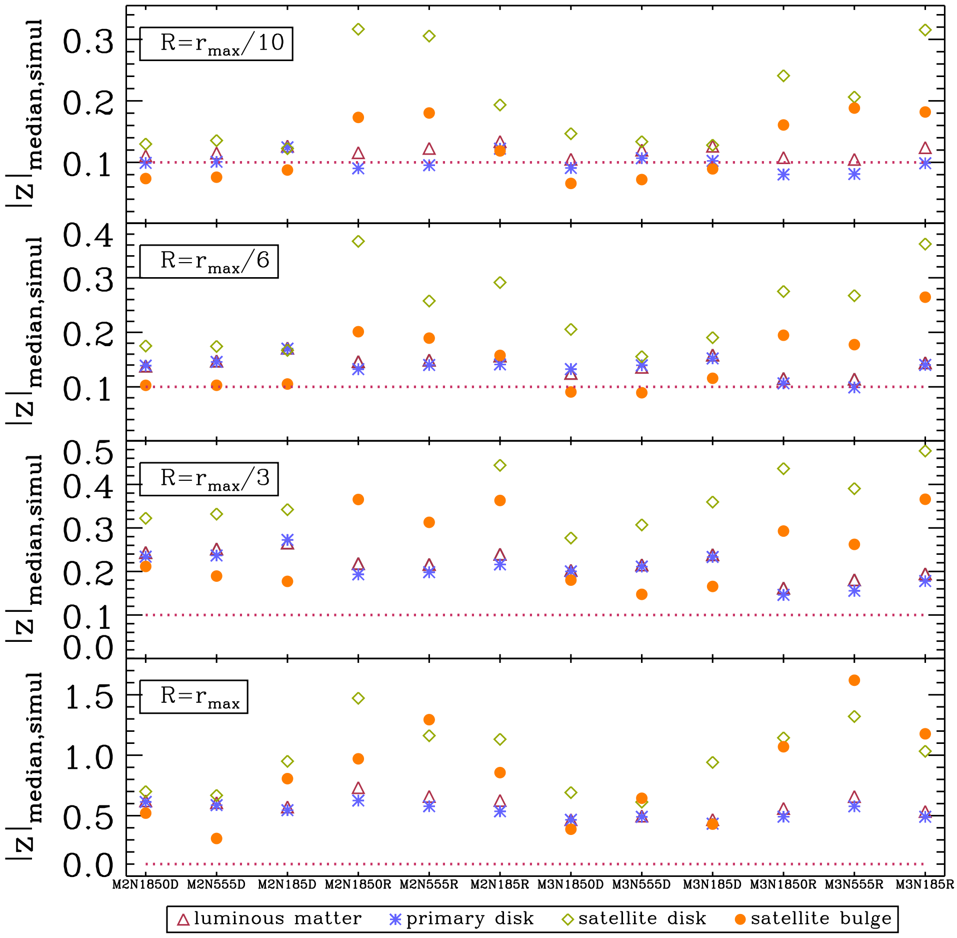

FIGURE 5.4— Medians of the vertical distribution of each remnant separated by components and by the radius at which it has been measured. The red triangles correspond to the total luminous matter, the blue asterisks to the luminous particles that originally formed the disc, the lime-green diamonds correspond to the satellite disc, and the orange filled circles to the luminous particles of the satellite bulge. Top: measurements at the innermost fixed radius which represent ∼ 10% of the primary disc length. Middle-up: measurements of the fixed radius that enclosed ∼ 20% of the initial disc length. Middle-bottom: measurements roughly corresponds to the half mass radius of primary disc. Bottom: measurements at the maximum radius. Given that the satellite bulge particles do not reach such external radius, its presence is statistically insignificant. In all the panels the red line corresponds to the initial scale height ($z_D = 0.1$).

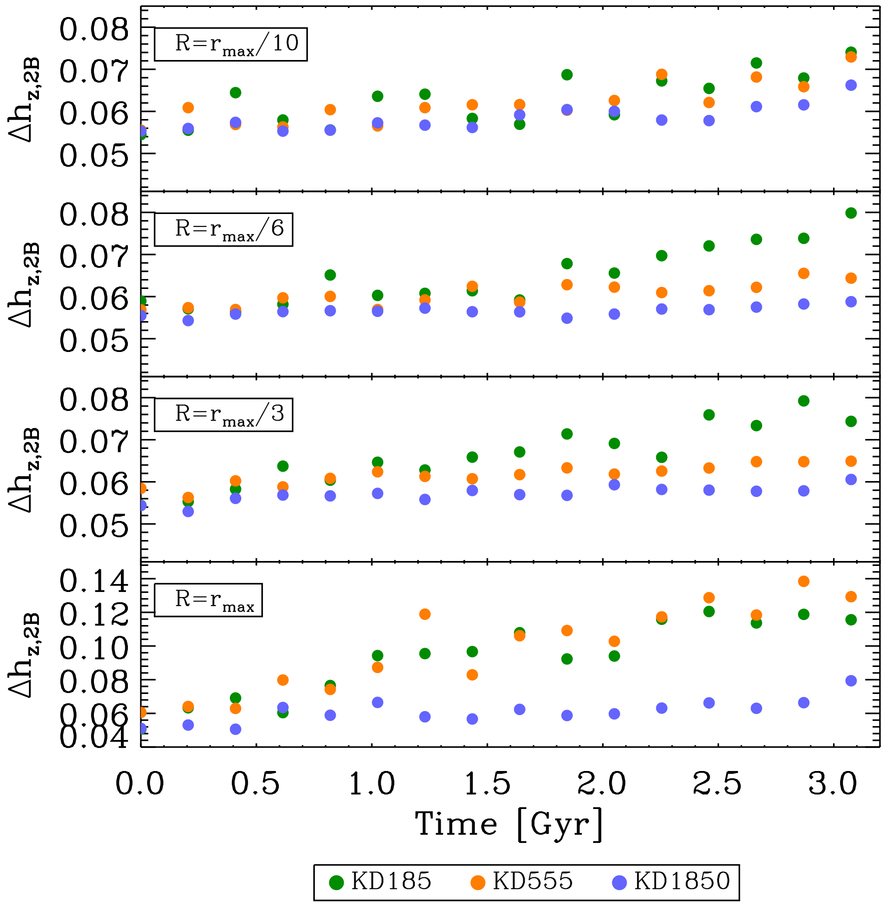

FIGURE 5.5— Medians of the change in the disc vertical distribution for the isolate temporal evolution of the three primary galaxies. Blue filled circles: progenitor galaxy that will form the system with 185,000 particles. Orange filled circles: progenitor galaxy that will be used for the 555,000 particles systems. Green filled circles: progenitor galaxy that will generate the system with 1,850,000 particles.

than the previous one, and the blue filled circles to the primary galaxy with the highest number of particles (main galaxy-satellite system with $10N$). Even though the evolution time for some models is $\sim$ 4 Gyr, we have only plotted the time that is common to all of them. In Figure 5.5, we see that the medians of the vertical distribution at the beginning were very similar regardless of the radius taken into account, and how the values start to increase, especially for the model with the lowest number of particles, while the one with the highest number of particles remains nearly constant at all radii. This corroborates the hypothesis that a high number of particles reduces the numerical thickening due to the residual collisions in the code.

In Table 5.3 we present the medians of the data shown in Figure 5.5. The values for the model with the highest numerical resolution are the same as 0.05 found by Eliche-Moral et al. (2006) and very similar to those found by Kuijken & Dubinski (1995). To avoid underestimating or overestimating the $\Delta h_{\rm z,2B}$ correction in the models, we will apply the appropriate correction according to their number of particles and radius of measurement of each merger experiment. The vertical heights corrected from numerical heating (eqn. 5.15) are show in Figure 5.6.

TABLE 5.3— Medians of the $\Delta h_{\rm z,2B}$ computed from the isolated evolution of the primaries galaxies.

R (1)	$KD185$ (2)	$KD555$ (3)	$KD1850$ (4)
$r_{\rm max/10}$	0.0672 ± 0.0072	0.0626 ± 0.0045	0.0567 ± 0.0153
$r_{\rm max/6}$	0.0697 ± 0.0077	0.0623 ± 0.0024	0.0564 ± 0.0142
$r_{\rm max/3}$	0.0714 ± 0.0072	0.0633 ± 0.0028	0.0568 ± 0.0145
$r_{\rm max}$	0.1137 ± 0.0238	0.1184 ± 0.0197	0.0587 ± 0.0181

Note.- *Col. (1)*: radius at which the median vertical distribution were measured, *Col. (2)*: medians of the median vertical distribution for the isolated primary model with the lowest number of particles, *Col.(3)*: medians of the median vertical distribution for the isolated primary model with the intermediate number of particles, *Col. (4)*: medians of the median vertical distribution for the isolated primary model with the largest number of particles.

In Figure 5.6, we find that for all the models the vertical distribution is extended at large radii , i.e. the discs are broadening gradually. The vertical distribution of the total luminous matter is dominated by the vertical scale of the primary disc, which has a slightly lower vertical distribution. The vertical scale of the satellite disc is always lower, implying that its material contributes to the thick disc formation. The vertical distribution of the satellite bulge is always lower than the satellite disc except for the most external radius, although such radius is populated by just a few bulge particles and it is not statistically significant. However, at lower radii, its vertical distribution is closer to that of the primary disc, which means that these particles contribute to the inner structure.

We also see in Figure 5.6 that the satellite material shows a higher median distribution in the retrograde cases than the direct cases at $r_{\rm max}/3$ for both

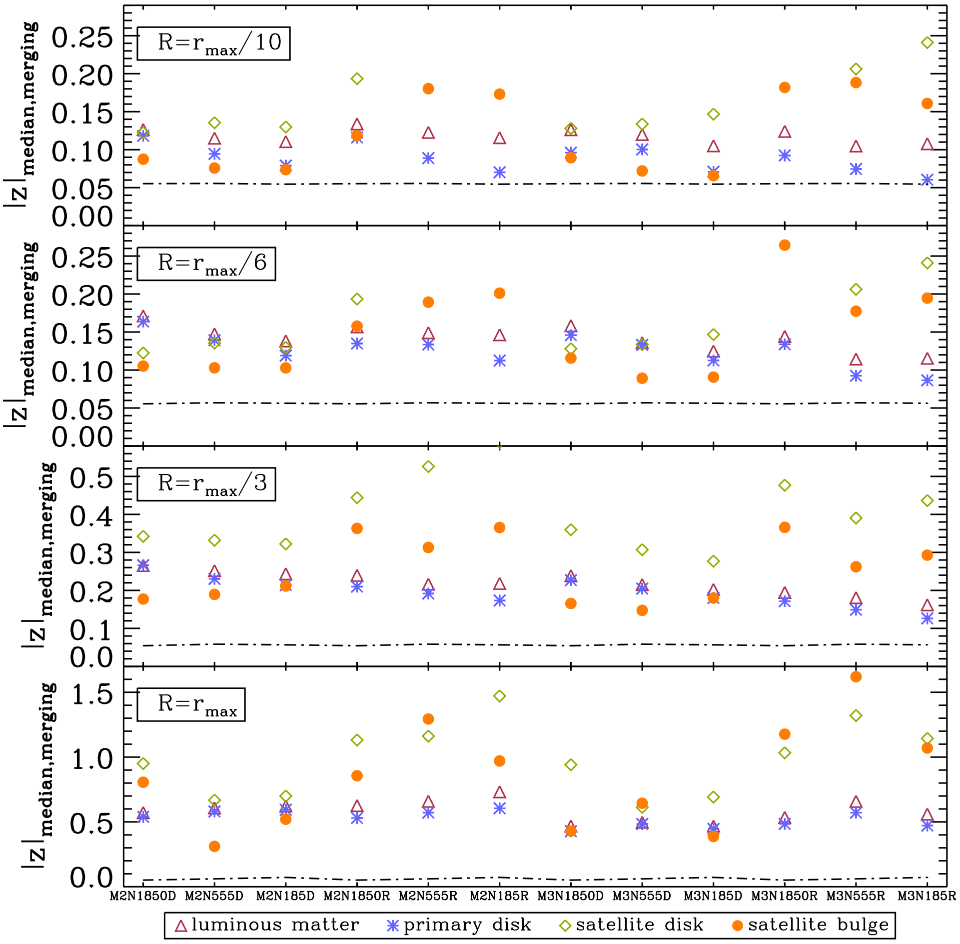

FIGURE 5.6— Medians of the vertical distribution for each remnant corrected from the two-body effect. We have kept the same notation and symbol meaning as in Figure 5.4. The dashed line corresponds to the value of the two-body correction, which is different for different number of particles in the progenitor galaxy.

mass ratios. On the other hand, the models with mass ratio 3:1 have a lower vertical scale. This is easier to see in Figure 5.7, in which we show the vertical distribution of the luminous matter as a function of the radius measured at eight fixed radii (1.8, 2.25, 3.0, 3.75, 6.0, 7.5,18 and 22.5 kpc). Our mergers produce flared discs as other published simulations of disc thickening by minor mergers (Walker et al. 1996; Villalobos & Helmi 2008). Flaring is inevitable in merger models because the dense inner regions have stronger disc forcing compared to companion forcing and the perpendicular response is small, in contrast to the low-density outer regions that have lower local disc forcing and stronger companion forcing, so the disc responds more to perturbations; besides, minor mergers also add more energy and mass to the outer disc than the inner disc (Bournaud et al. 2009). We also see that the retrograde orbits are more efficiently increasing the vertical distribution in the outskirts of the disc. The reason is that the direct orbit precesses causing the fusion to be closer to the main galaxy plane, whereas the prograde orbit keeps its inclination, thus impressing more vertical energy.

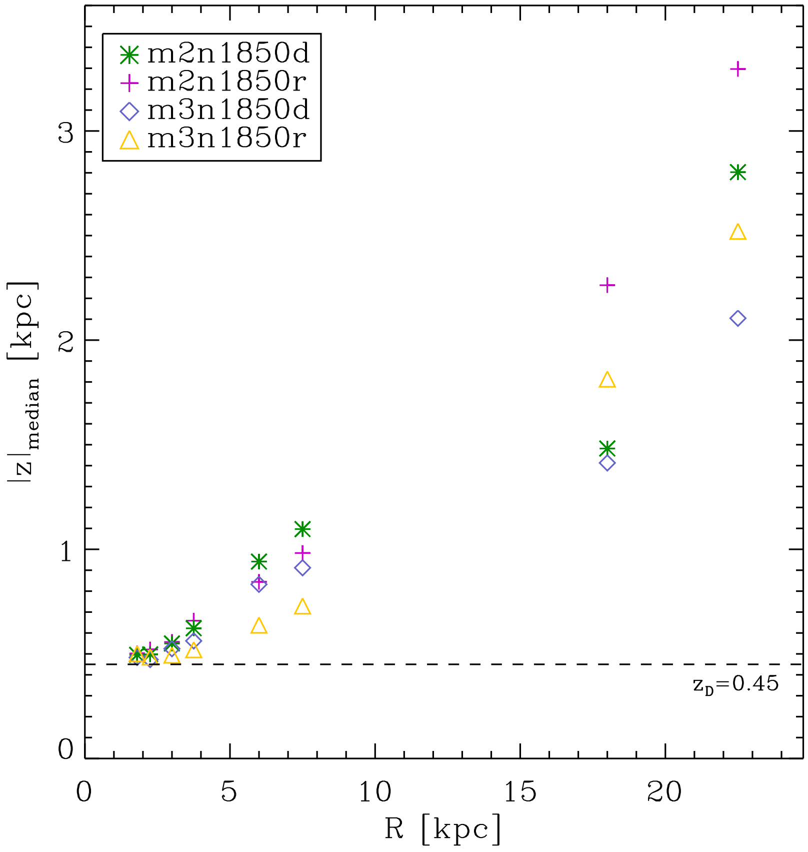

FIGURE 5.7— Vertical distribution of the remnant as a function of the radius for the remnants with the highest numerical resolution. Data are measured at 8 fixed radii: 1.8, 2.25, 3.0, 3.75, 6.0, 7.5,18 and 22.5 kpc. The dashed line indicates the initial scale height.

Comparison with other work

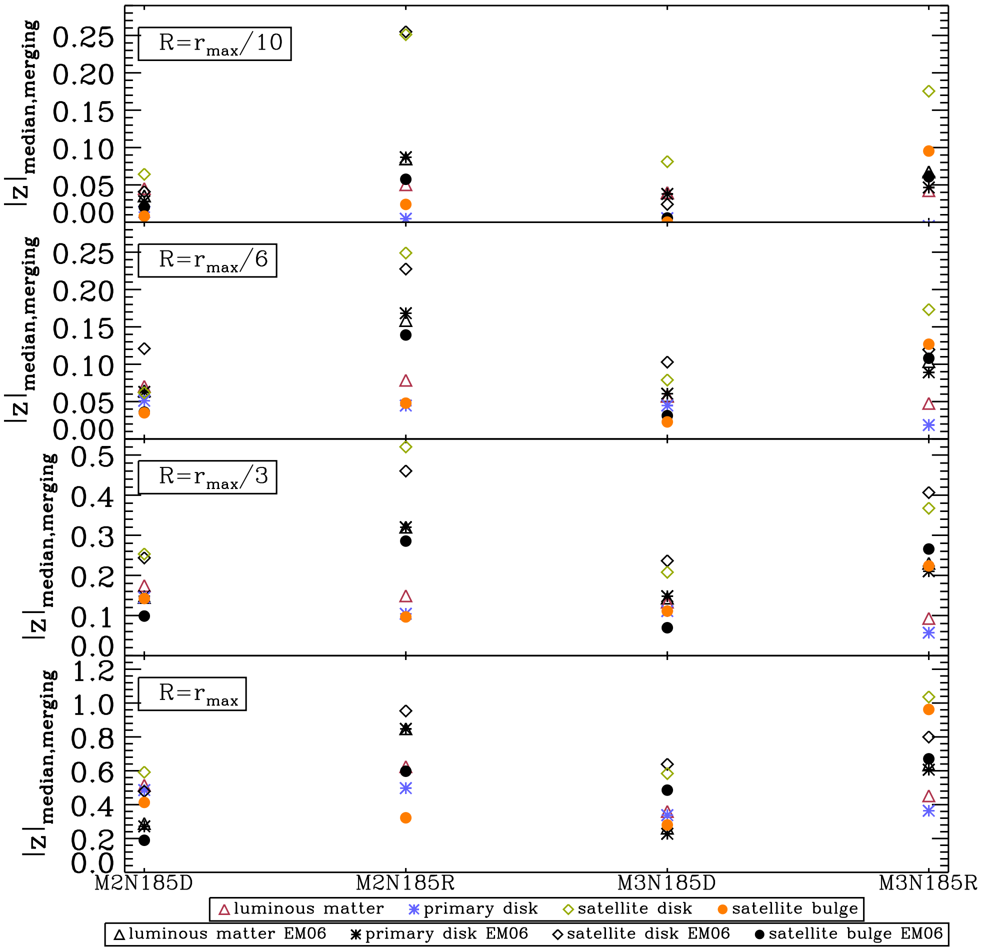

FIGURE 5.8— Median vertical distribution of the low numerical resolution remnants compared with the data of Eliche-Moral et al. (2006). Both corrected from numerical heating. We have kept the same plot style and notation than in previous figures. The black-colored symbols represent the Eliche-Moral et al. (2006) measurements.

Our low numerical resolution models, both direct and retrograde groups (M2N185D, M2N185R, M3N185D and M3N185R), are comparable with EM06 data. EM06 measured the vertical distribution of their remnants, but their models had only 185,000 particles, which is equal to the number of particles of our merger experiments with the smallest numerical resolution. On the other hand, their work was focused on the bulge growth. In this sense, the present study can be considered as an expansion of their work. In Figure 5.8 we show the median vertical distribution for our four models along with the data of EM06 data. The direct cases at the smallest radius nicely match our measurements. This is no longer observed at more external radii, especially for the retrograde cases where the difference within the same component can be as high as 40% (see top panel). That difference could be due to the way the vertical distribution is measured or it could be explained by taking into account that, even though we are comparing the same galaxy model, the simulations were executed with a different code in a different machine, facts that lead to macroscopic variations related to the the unavoidable stochasticity connected to disc dynamics in all simulations of disc-halo systems (Sellwood & Debattista 2009). Regardless of this, we find that our data have a good Pearson correlation coefficient of 0.932 for the M2N185D model, 0.867 for the prograde case (M2N185R), 0.917 for the M3N185D and 0.897 for its prograde case.

5.7.3 Orbit-vertical scale relationship

A clear relationship between the value of the median vertical distribution for each component and the model characteristics (number of particles, direct or retrograde orbit) is not apparent in Figure 5.6. To determine if the observed increase in the vertical distribution is connected with a particular event in the simulation, for example the merging of the galaxies, we have separated the merger experiments in groups and have focused on the evolution of the primary disc at radius $r_{\max}/3$. Also, we determined the separation distance between the centre of mass of the the primary and satellite bulges along the whole simulation.

In Figure 5.9 we show the simulation experiments that form the group M2TF35D. On the top panel we plot the separation distance between the bulges, which can be interpreted as the separation between the galaxies, as a function of time. Next, we show the median vertical distribution of the primary disc, starting from the model with the highest numerical resolution toward the lowest. The data has been plotted separately according to the radius at which they were measured (same fixed radii as figures 5.6, 5.4 and 5.8). In all the plots, the magenta filled circles represent the innermost radius; in order of increasing radius, we have green, orange and blue circles, the last ones corresponding to the maximum radius. In Figure 5.9 we see that the orbits of the three models are quite similar, with a slightly different pericentre radius. The low numerical resolution model (M2N185D) presents a bump at $\sim 0.7 - 0.8$Gyr. We also find that the maximum of the vertical distribution coalesces with the first pericentre passage. If we observe the temporal evolution of the vertical distribution of the models, we find that, except for the most external radius, the behavior is very similar and is markedly more stable after ~ 1.2Gyr, when the merger has been completed.

In Figure 5.10 we show a similar plot for the retrograde group (cf. 5.9), keeping the same notation and symbol meaning. The orbit described after the first pericentre passage in these models differ from those featured in Figure 5.9: the satellite separates a distance ~ 6 kpc before the second pass for the pericentre until it finally merges at time ~ 1.7Gyr. The increase in the vertical distribution for the most external radius is greater than in the direct cases. This means that the satellite material contributes predominantly to enrich the outer regions of the primary disc without significantly altering the vertical distribution at inner radii. Interestingly, the fusion times for both direct and retrograde orbits are almost the same, due to the fact that the orbits are highly radial and hence very similar.

To illustrate that the models with large mass ratio show a similar trend, in Figure 5.11 we present the cases with direct orbit.

In Table 5.4 we collect the results obtained for the thickening of the disc in all our models, focusing on the third fixed radius (corresponding to ~7.5 kpc), which is large enough to avoid bulge contamination but not too external to be affected by the tidal tails and flares. We see that the model with direct orbits undergoes more thickening than the retrograde cases, even though it seems contradictory to what we discussed above (see the trend in Figure 5.7).

Table 5.4— Thickening of all the merger experiments.

model (1)	$\mid z_{\rm disc} \mid_{\rm f} / \mid z_{\rm disc} \mid_0$ (2)	$\mid z_{\rm lm} \mid_{\rm f} - \mid z_{\rm disc} \mid_0$ (3)
$M2N185D$	4.252	0.2026
$M2N555D$	4.038	0.194
$M2N1850D$	3.860	0.188
$M2N185R$	3.351	0.177
$M2N555R$	3.369	0.158
$M2N1850R$	3.128	0.163
$M3N185D$	3.629	0.176
$M3N555D$	3.588	0.157
$M3N1850D$	3.244	0.147
$M3N185R$	2.743	0.132
$M3N555R$	0.948	0.123
$M3N1850R$	2.278	0.106

Note.- *Col. (1)*: model name, *Col. (2)*: thickening due to thin disc growth, *Col.(3)*: thickening due to the satellite accretion.

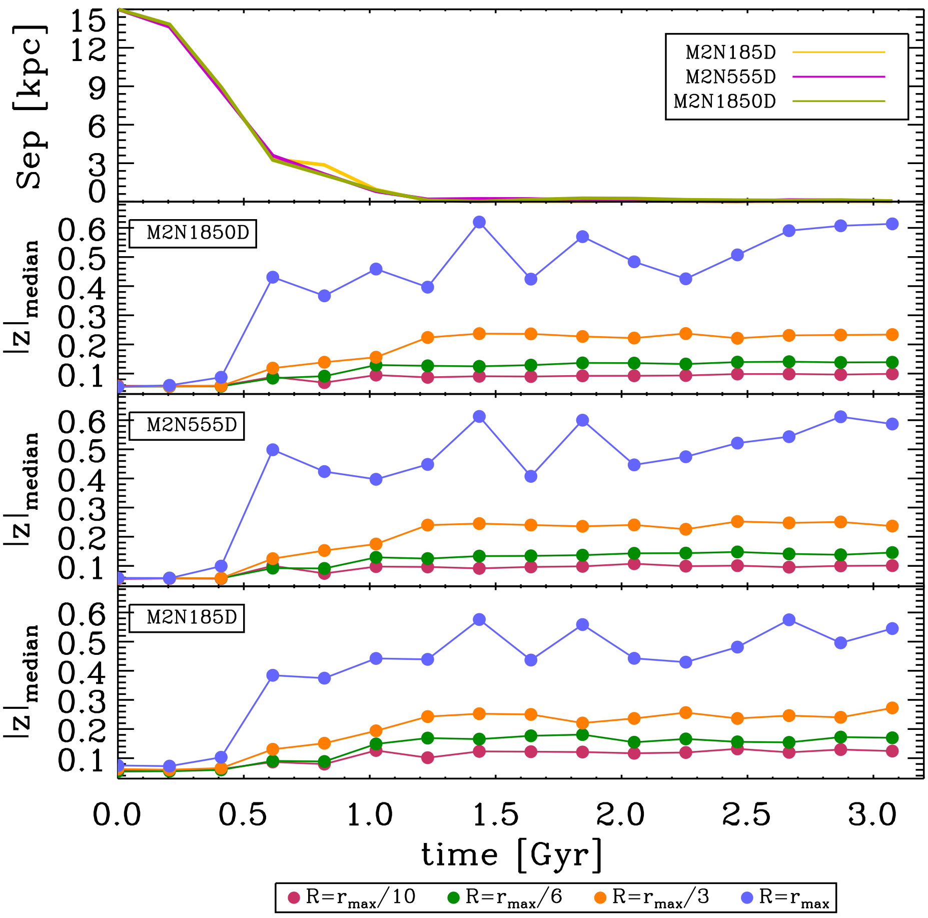

FIGURE 5.9— Temporal evolution of the vertical distribution (corrected from numerical heating) of the discs for the models in the group M2TF35D. Top: separation distance between the bulges of the primary galaxy and the satellite bulge. The orange, magenta and pale-green lines correspond to the model with the lowest number of particles (M2N185D), the intermediate particle number model (M2N555D) and the one with the largest number of particles (M2N1850D), respectively. In all the plots, the red filled circles correspond to the measurements at the most internal radius, the green filled circles to the measurement at the next radius, the orange filled circles correspond to approximately the half-mass radius, and the blue circles to the maximum radius, which is the total length of the disc. Middle-Up: model with the highest number of particles. Middle-bottom: intermediate model. Bottom: model with the smallest number of particles.

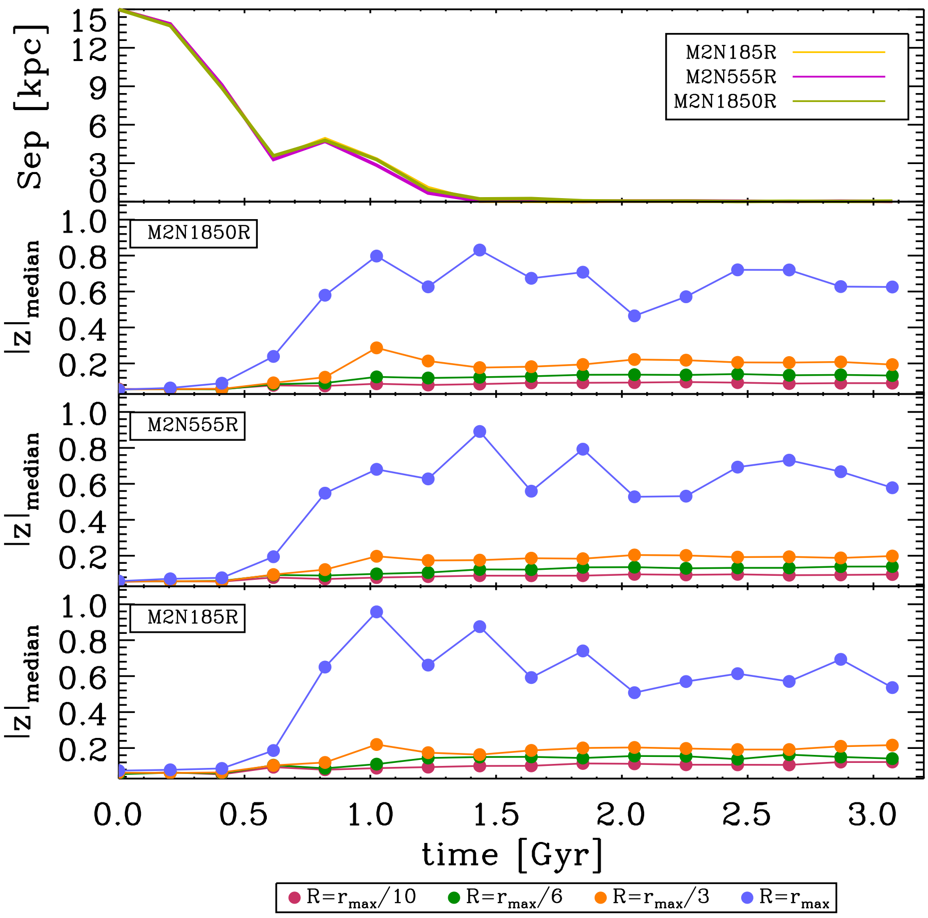

FIGURE 5.10— Temporal evolution of the vertical distribution (corrected from numerical heating) of the discs for the models in the group M2TF35R (retrograde orbit). The meaning of the symbols are the same as in Figure 5.9. Middle-up panel: model with the highest number of particles; middle-bottom: intermediate model; bottom panel: model with the smallest number of particles.

5.7.4 Velocity dispersion profile

The vertical kinetic energy characterised in terms of the z-component of the velocity dispersion provides information about the thickening. In Figure 5.12 we present the velocity dispersion of our highest numerical resolution remnants, at the start and at the end of the mergers. The initial profiles show a pattern typical of disk galaxies, namely a peak in the region of the bulge, reaching a

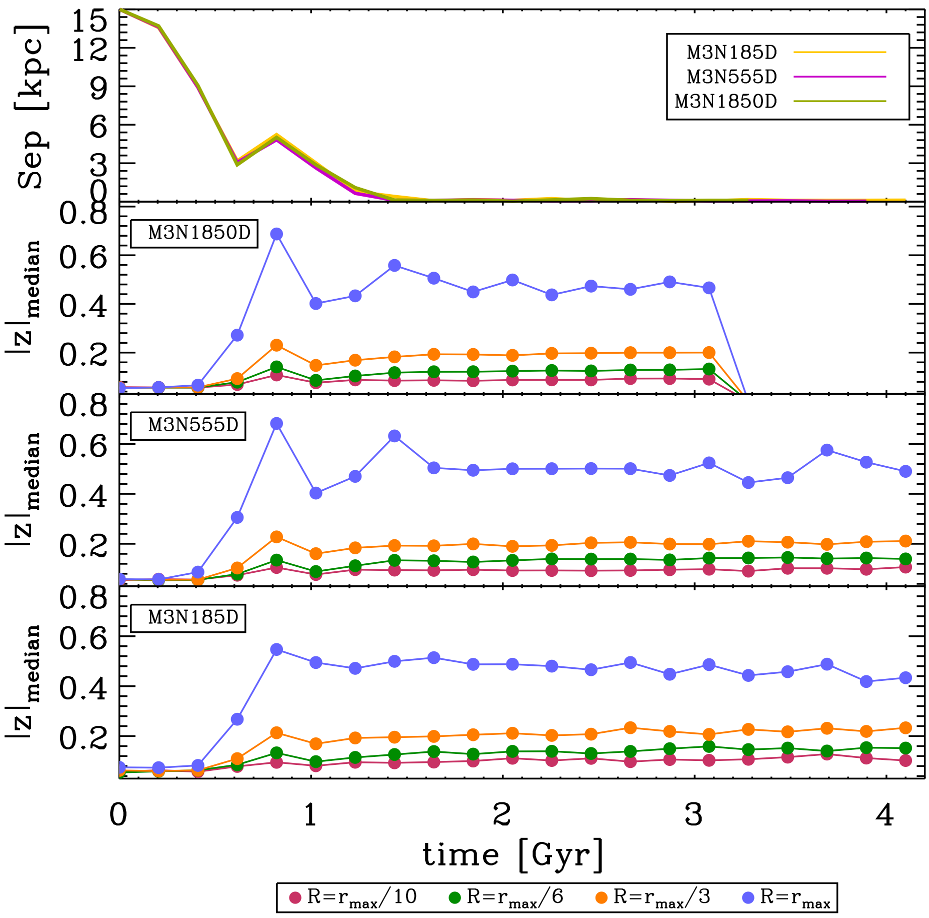

FIGURE 5.11— Temporal evolution of the vertical distribution (corrected from numerical heating) of the discs for the models in the group M3TF35R. We keep the notation of Figures 5.9 and 5.10. In this case, the time axis is more extended for the intermediate number of particles model (M3N555D) and for the model with the lowest number of particles (M3N185D).

central dispersion $\sigma_z = 130 \text{ km s}^{-1}$, and a sharp decrease toward the disk which shows vertical dispersions $\sigma_z \sim 10 \text{ km s}^{-1}$. The final profiles show a similar bulge-disk pattern, but σ_z in the region of the disk has increased by factors between 3 and 5. These factors are similar to the increase in vertical scale-height, as expected from $h_z = \sigma_z / (2\pi G \rho_0)^{1/2}$ (Spitzer 1942; van der Kruit & Searle 1981). Dispersions gently decrease with radius in the prograde mergers, and are flat or slightly increasing with radius in the retrograde mergers. On the other hand, dispersions are slightly higher in the retrograde mergers as compared with their corresponding prograde cases. These differences are due to the differences in the merger orbits: as noted above, inclined prograde orbits migrate toward the plane of the primary disk and inject less vertical energy to the primary disk than the corresponding retrograde orbits.

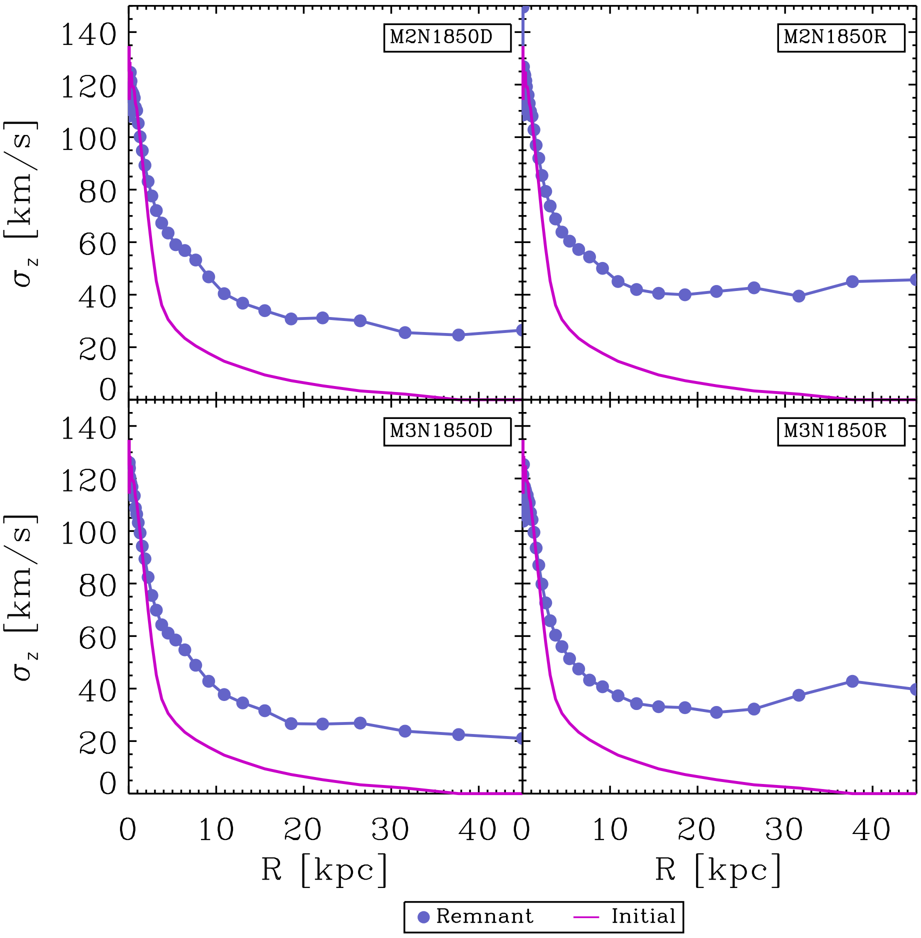

FIGURE 5.12— Vertical velocity dispersion of the luminous matter for all the merger experiments (cf. 5.3). The pink lines correspond to the main galaxy a the beginning of the simulations and the blue points correspond to the remnants.

5.7.5 Isophotes

Bournaud et al. (2009) argued that, if the thick discs have a merger origin, one may expect the remnant to show “boxy” isophotes when the galaxy is seen edge-on. In figure 5.13 we plot our highest resolution remnants and search for this type of isophotes. Instead, we find “disc-like” isophotes. This means that the low-mass regime of our merger experiments is insufficient to perturb the disc so as to produce a change in the isophotes. This could be achieved throught the accretion of more than one satellite.

5.8 Conclusions

Our models exhibit the typical characteristics of a minor merger event. The satellite is completely disrupted, injecting its material to the primary galaxy inducing the formation of tidal tails and transient distortions.

The types of orbit described by our satellites are very similar for all the models. The twelve models reach the pericentre radius at ~ 0.6 Gyr and complete the fusion around 1.4 Gyr. This suggests that there is no dependency between the orbits and the number of particles.

Our highest numerical resolution model has values of numerical heating that are very similar to those found by Eliche-Moral et al. (2006) and Kuijken & Dubinski (1995); on the other hand, our lower numerical resolution models show larger values and greater variations at the different measured radii.

The median of the vertical distribution of the remnant is dominated by the primary galaxy disc, whereas the satellite disc contributes to enrich the outer regions of the primary disc, sparsely altering the inner radii. The satellite bulge contributes to the inner structure of the remnant, given that we find only a small amount of original bulge particles at the most external radius. Since there is no clear relationship between the number of particles and the vertical distribution (after the two-body encounter correction) the differences must be due to global instabilities.

Comparing a subset of our remnants with the Eliche-Moral et al. (2006) data we have found that our results are in good agreement with a Pearson correlation coefficient ~ 0.90 for the direct cases and 0.88 for the retrograde cases.

We find that the single accretion of a low-mass satellite produces a thickening of ~ 2.7–3.5. Nevertheless, it is not sufficient to perturb the disc and to produce the boxy isophotes expected if the thick disc is formed by mergers.

Our conclusion is that both mechanisms, the accretion of satellites and the heating of the disc, play a role in the building of the thick disc in the merger-driven scenario. The accretion of a satellite results in the deposition of mass in

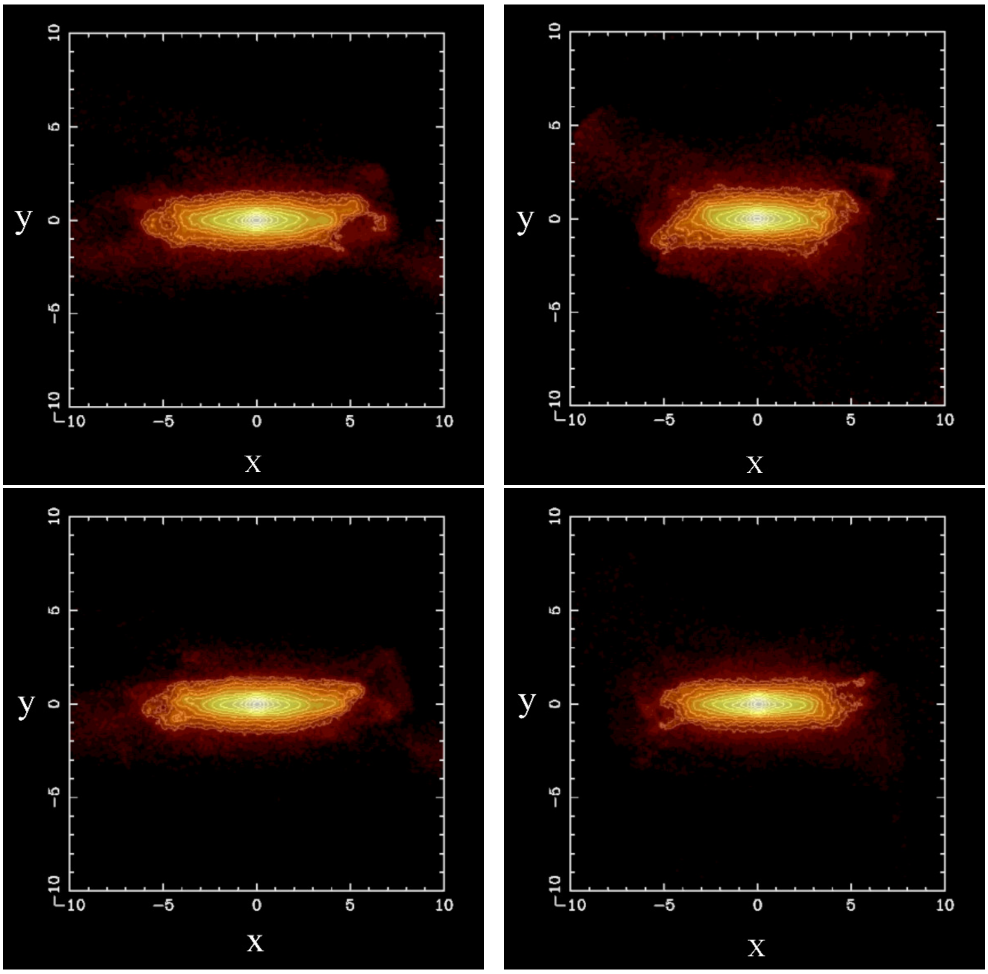

FIGURE 5.13— Edge-on view of the luminous matter and density contours. Upper left: remnant m2n1850d. Upper right: remnant m2n1850r. Bottom left: remnant m3n1850d. Bottom right: remnant m3n1850r. In all the panels, contours are plotted in 20 logarithmic levels (0.0, 0.05, 0.11, 0.16, 0.22, 0.28, 0.33, 0.38, 0.44, 0.50, 0.55, 0.61, 0.66, 0.71, 0.77, 0.82, 0.88, 0.94, 0.99, 1.04), from zero to a maximum coordinate of 10 length units. Units are expressed in simulation length units where [R]=1.

the outer parts and the injection of kinetic energy into the disc, thus heating the disc, and enhancing the settling of thin disc material into greater heights. We stress the necessity of more than one satellite to shape a thick disc by tidal debris of disrupted systems or to produce a big change in the direction of the angular momentum of the disc to generate a slowly rotating or counterrotating thick disc.

5.9 Future work

Currently, the efforts to explain the formation of thick discs have appealed to the importance of the ΛCDM scenario. For example, Bournaud et al. (2009) suggested that thick discs are formed internally in unstable, gas-rich, clumpy disks at high redshift. Recently, Doménech-Moral et al. (2012), through four middle-mass disc galaxies obtained from hydrodynamic simulations in a ΛCDM scenario, found that the structural parameters (e.g. the scale height) of the simulated thick discs suggest that such a component could result from the combination of different thickening mechanisms that include merger-driven processes, but also long-lived internal perturbations of the thin disc. On the other hand, Forbes et al. 2012 have pointed out that thick discs need not be formed from thin discs, suggesting that the formation is due to an age-velocity dispersion correlation, in which the high velocity dispersion of gas in discs at $z \sim 2$ decreases along with the cosmological accretion rate, while at lower redshift, the dynamically colder gas forms the low velocity dispersion stars of the thin disk. In other words, the thick disc is forming not because of external perturbers, mergers, or gradual heating of a thin disk, but because σ decreases with time and newly formed stars induce transient instabilities in the disc. Both of these processes are strongly dependent on the cosmological situation in which the disc finds itself, i.e. its accretion history.

There is no other galactic accretion history better-known than the Milky Way's (e.g. Peñarrubia et al. 2011; Belokurov et al. 2010). Furthermore, since a large fraction of stars in the present-day universe live in galaxies comparable to the Milky Way and because the large majority of Milky Way stars live in the disc, our galaxy's disc represents a unique benchmark to test the thin-thick disc dichotomy. Our cosmological merger histories as are envisioned in Section 3.9 can also be useful for this purpose. If we took our merger histories since $z \sim 1$, the epoch of disc settling (Kassin et al. 2012), and replaced the parent galaxy with a Milky Way-like model, from these simulations we would obtain a set of remnants with unique merger histories. Since thick-disc evolution can be used as a tracer of the merger history of the Galaxy, by measuring the thickening of the disc and directly comparing with studies of kinematical properties of the Galactic thick disk with Galactic height Z (e.g. Moni Bidin et al. 2012), we could quantify the number of satellites that a typical galaxy like the Milky Way has accreted, thereby putting constraints on the current merger rate. We may also explore the differences due to the characteristics of the accreted satellites by varying their morphological type or their dark matter content. Additionally, we can re-simulate some of these simulations with higher numerical resolution to study the spatial distribution of the resulting bound substructures at different epochs.

From these proposed simulations, it will also be possible to perform a study similar to the one we developed for the elliptical galaxies (Chapter 4), i.e. analysing the metallicity gradients that such satellites generate on the host galaxy to test whether the observed flat gradient (Bovy et al. 2012; Cheng et al. 2012) may also be consistent with a merger-driven scenario for thick disc formation.

6

Conclusions

Voyagers 1 and 2 have traveled billions of miles through the ocean of space,
exploring dozens of new worlds along the way
and revolutionizing our knowledge of the solar system in which we live.
And as a gift of the brilliant mission design,
these robot ships are no longer bound by the Sun's gravity.
They have passed the outermost planets
and are on their way to the cold,
dark near-vacuum that constitutes interstellar space. Nothing can stop them.
A billion years from now, when everything on Earth
we've ever made has crumbled into dust,
when the continents are changed beyond recognition
and our species is unimaginably altered or extinct,
the Voyager record will still speak for us.

Carl Sagan and Ann Druyan
Cosmic Journey: The Voyager Interstellar Mission and Message

By means of numerical N-body simulations, we have explored three different problems in the framework of the dry mergers scenario of galaxy evolution: *i*) we studied the effects of dry mergers on the size evolution of high-redshift compact elliptical galaxies; *ii*) we estimated the metallicity gradients of a present-day massive elliptical generated by dry mergers; *iii*) finally, we examined the contribution of minor dry mergers towards the generation of a thick disc in a disc galaxy. In the following paragraphs, we briefly present the main conclusions of this work. In the subsequent sections, we enumerate the conclusions of each part in greater detail.

For the massive elliptical galaxies, we find that, although we neglect all dissipationless process in our merger simulations, we sucessfully reproduce their observed size evolution. In addition, the weak evolution in the velocity dispersion that we find is compatible with observations. Our results, suggest that dry minor mergers cannot be ruled out as a mechanism to generate present-day elliptical galaxies.

Our dry merger remnants show estimated (radial) metallicity gradients similar to those observed for early-type galaxies.

We have found that our results are not conclusive about the formation of the thick disc. We need to perform simulations in which the initial galaxy incorporates more physical properties, such as star formation efficency and gas hydrodynamics. Also, it is necessary to explore more types of orbits and higher number of accreted satellites to give a comprehensive view of the merger-driven scenario of galaxy growth.

Size evolution of elliptical galaxies in a Λ CDM universe

From the merger experiments of the accretion of satellites by a high-redshift compact elliptical galaxy, we show that cosmologically-motivated merger histories with satellite sizes derived from observational relationships are able to reproduce the size evolution of the massive elliptical galaxies.

For the study of the massive galaxies the main conclusions are:

- Remnants at $z = 0$ are less compact than their $z = 2$ counterparts, as a result from the merging and interactions with the accreted satellites, which loose their structure and deposit their material in the outer part of the main galaxy, producing its size growth.
- Cosmologically-motivated dry minor mergers can generate a size growth of a factor of ~ 4 with a mass increase of a factor of 2, which is compatible with observations.
- The accretion of realistic satellites produces a moderate increase in the velocity dispersion of the remnant, in agreement with some observational works that found a mild evolution in the velocity dispersion of massive early-type galaxies, favoring the scenario where massive galaxies grow inside-out.
- We fit a power law relationship between stellar mass and effective radius: $r_{e_f}/r_e(z = 2.5) = (1.182 \pm 0.035) \left(\frac{M_{\star f}}{M_\star(z{=}2.5)}\right)^{(1.547\pm0.147)}$.
- Our remnants verify the following relationship between stellar mass and velocity dispersion: $\sigma_f/\sigma(z = 2.5) = (1.008\pm0.011) \left(\frac{M_{\star f}}{M_\star(z{=}2.5)}\right)^{(0.044\pm0.038)}$.
- To first order of approximation, the estimated dynamical mass of our remnants is smaller than the stellar mass.

- Our merger experiments obey $M_{dyn} \approx 2\left(\sigma^2 r_e/G\right)$, which involves a lower $K(n)$ than the that given by Cappellari et al. (2006).

Effects of dry mergers on the metallicity gradients of massive elliptical galaxies

By assuming that the metallicity of our remnants only depends on their mass and the redshift at with they are accreted, we have estimated the metallicity gradients for a subsample of our merger histories remnants using observational relationships. We have found that our remnants reproduce the metallicity gradient trends of observed early-type galaxies.

For our remnants subsample, we find the following:

- The metallicity gradient steepness is correlated to the mass of the progenitor galaxy.
- The effect of accreting satellites is to produce a shallower metallicity gradient.
- Our results show that, just from the the fact that merger-driven mixing is incomplete and the preference for mass deposition in the outer parts, the combined effect of mergers between $z = 2$ and $z = 0$ is to flatten the metallicity profile so that the final gradient is ∼40% of the gradient at $z \sim 2$.

Minor mergers and disc thickening

From the dissipationless minor merger accretion between two disc galaxies we have found that a single accretion event produces the thickening of a pre-existing thin disc. The formed "thick-disc" shows a flared appearance. We find that the mass deposited by a single low-mass satellite is insufficient to form entirely form a thick disc from disrupted satellite debris. Also, we see that the injection of kinetic energy is not enough to generate the disky isophotes expected for a thick disc.

For our 12 merging experiments, we find:

- Satellites with a Tully-Fisher index of 3.5 reach the center of the remnant and are completely destroyed.
- The models with highest numerical resolution have values of numerical heating very similar to those found by Eliche-Moral et al. (2006) and Kuijken & Dubinski (1995).

- Single accretion of a low-mass satellite produces a thickening of a factor ~ 2.7–3.5.

- The median of the vertical distribution of the remnant is dominated by the primary galaxy disc, whereas the satellite disc contributes to enrich the outer regions of the primary disc, sparsely altering the inner radii. The satellite bulge contributes to the inner structure of the remnant.

- We compared our lowest numerical resolution models with Eliche-Moral et al. (2006) data. We found that our results are in good agreement, with a Pearson correlation coefficient ~ 0.90 for the direct cases and 0.88 for the prograde cases.

- There is no clear relationship between the number of particles and the vertical distribution (after the two-body encounter correction), so the differences must be due to global instabilities.

- Retrograde orbits produce a thicker vertical distribution at the outermost radii than the direct orbits. Conversely, in the direct orbits case, the thickening is greater at inner radii.

- The generated thick disc is populated with both satellite debris and the original disc material that is dynamically heated and occupies greater heights during the merging process.

A

Appendix section of chapter 3

A.1 Building spherical two-component model

In this section we will explain how the Smulders & Balcells code generates the galaxy models.

In deriving models analytically or numerically there are in general two different approaches. One is to start with a distribution function, which is a function of integrals of the motion, and try to derive the potential by solving Poisson's equation. The other is to start with a potential-density pair and try to derive the distribution function. The latter is the simplest to apply to spherical systems.

A.1.1 Potential-density pair

Since the density distribution, which is derived from the surface brightness profile, is the most important link between models and real galaxies, it is important to use a method which leaves the density intact. In the present method, models are constructed that are composed of a luminous and a dark matter component, for which the density profiles are precisely known. The two components are in equilibrium in the total potential and therefore the model composed of these two components is also in equilibrium.

To find the distribution function for the two components separately, Eddington's formula has to be solved for the separate densities in the potential generated by the total density. For a system with density ρ_{T}, which is composed of densities ρ_1 and ρ_2, with a potential ϕ_{T} composed of potentials ϕ_1 (which satisfies Poisson's equation for ρ_1) and ϕ_2 (which satisfies Poisson's equation for ρ_2), so that:

$$\rho_T = \rho_1 + \rho_2 \qquad \text{and} \qquad \phi_T = \phi_1 + \phi_2 \tag{A.1}$$

the equation's that have to be solved to get the distribution functions for the components ρ_1 and ρ_2 are:

$$f_1(\mathrm{E}) = \frac{1}{\sqrt{8}\pi^2}\int_0^{\mathrm{E}} \frac{\partial^2\rho_1}{\partial\phi_T^2}\frac{d\phi_T}{\sqrt{\mathrm{E}-\phi_T}} \tag{A.2}$$

$$f_2(\mathrm{E}) = \frac{1}{\sqrt{8}\pi^2}\int_0^{\mathrm{E}} \frac{\partial^2\rho_2}{\partial\phi_T^2}\frac{d\phi_T}{\sqrt{\mathrm{E}-\phi_T}} \tag{A.3}$$

The distribution function of the total system is simply:

$$f_{\mathrm{T}}(\mathrm{E}) = f_1(\mathrm{E}) + f_2(\mathrm{E}) \tag{A.4}$$

The family of models used on the code are:

$$\begin{aligned}
\rho_{\mathrm{l}}(r) &= M_{\mathrm{l}}\frac{a_{\mathrm{J}}}{4\pi r^2(a_{\mathrm{J}}+r)^2}\\
\rho_{\mathrm{d}}(r) &= M_{\mathrm{d}}\frac{a_H}{2\pi r(r+a_{\mathrm{H}})^3}\\
\phi_{\mathrm{l}}(r) &= M_{\mathrm{l}}G\ln\Big(\frac{r}{r+a_{\mathrm{J}}}\Big)\\
\phi_{\mathrm{d}}(r) &= -M_{\mathrm{d}}G\frac{1}{a_{\mathrm{H}}+r}\\
\rho_{\mathrm{T}}(r) &= \rho_{\mathrm{l}}(r) + \rho_{\mathrm{d}}(r)\\
\phi_{\mathrm{T}}(r) &= \phi_{\mathrm{l}}(r) + \phi_{\mathrm{d}}(r)
\end{aligned} \tag{A.5}$$

In this model, ρ_{l} is the density of the luminous matter. It has the same density profile as the Jaffe model. The term ρ_{H} is the density of the halo, and it has the density profile of a Hernquist model. This is a two-parameter family of models, which depends on the ratio between M_{l} and M_{d} and the ratio between the half-mass radius of the luminous matter and the half-mass radius of the halo. The latter is determined by the parameter a in the following way:

$$r_{l\frac{1}{2}}/r_{h\frac{1}{2}} = \frac{1}{(1+\sqrt{2})a_{\mathrm{H}}} \tag{A.6}$$

The half-mass radius of the Jaffe component is equal to 1, and the half-mass radius of the Hernquist component of the models is equal to $(\sqrt{2}+1)a_{\mathrm{H}}$.

The cumulative mass of the Jaffe component of the model is equal to:

$$M_{\rm l}(r) \;=\; M_l \frac{r}{1+r} \tag{A.7}$$

The cumulative mass for the Hernquist component of the model is:

$$M_{\rm d}(r) \;=\; M_{\rm d} \frac{r^2}{(r+a_{\rm H})^2} \tag{A.8}$$

The total mass of the Jaffe component is equal to $M_{\rm l}$, whereas the total mass of the Hernquist component is equal to $M_{\rm d}$.

A.1.2 Distribution functions of the models

The shapes of the distribution functions of the isotropic model are shown in Figure A.1. Both the distribution function of the Jaffe Component of the model and the halo component of the model are nonnegative, monotonically decreasing functions of the energy.

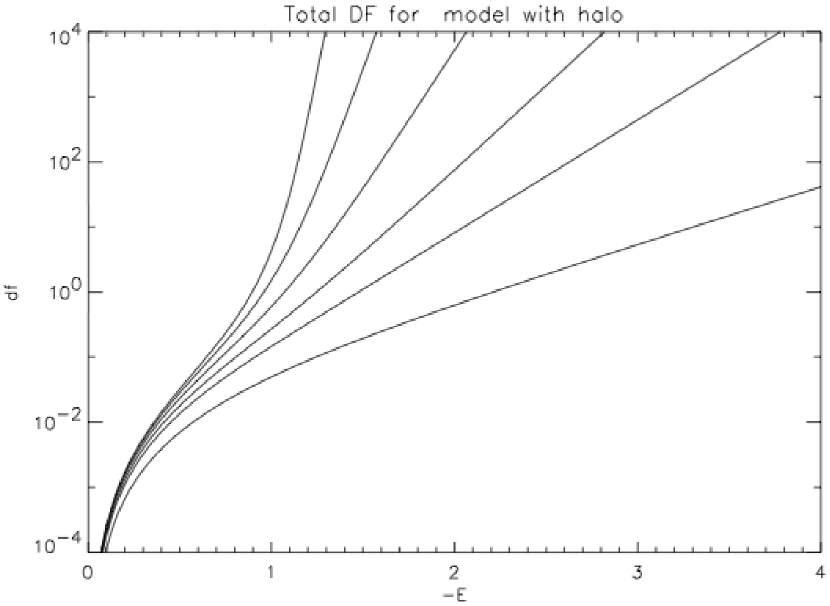

FIGURE A.1— Distribution functions of the total isotropic model. $M_{\rm d} + M_{\rm l}$ is set equal to 1, and $a = 1$ for all the models. The ratios $M_{\rm d} : M_{\rm l}$ from top to bottom are 16:1, 8:1, 4:1, 2:1, 1:1 and 0:1.

Figure A.1 shows the total distribution function for models with haloes. Here, the total mass is set to one, thus what is shown are models that have a distribution function that is almost equal to the distribution function of a Hernquist model, for those who have a high value for the ratio $M_{\rm d} : M_{\rm l}$ and models that have a Jaffe distribution function when $\rm M_d = 0$. The other models are intermediate cases of these two extremes. For the Hernquist model with $a_{\rm H} = 1$, the minimum value for the energy is -1. This is also where the distribution function diverges for the Hernquist model.

Velocity dispersion of the model

The radial and tangential velocity dispersions can be calculated analytically for these models. The velocity anisotropy of the models satisfies $\sigma_{\rm r}/\sigma_{\rm t} = 1 + r^2/r_{\rm a}^2$ (Merritt 1985). This can be used to solve the Jeans equation:

$$\frac{d(\rho\sigma_{\rm r}^2)}{dr} + 2\frac{\rho}{r}\left(\sigma_{\rm r}^2 - \sigma_{\rm r}^2\right) = -\rho\frac{d\phi}{dr} \tag{A.9}$$

This is a first order linear differential equation which can be solved to give:

$$\sigma_{\rm r}^2 = \frac{1}{\left(r_{\rm a}^2 + r^2\right)\rho(r)} \int_{r'}^{\infty} \rho(r')r'^2\frac{d\phi}{dr'}\left[1 + (r_{\rm a}/r')^2\right]dr' \tag{A.10}$$

When solving equation (A.10) for a model with a halo, it is important to note that the total potential should be used, but only the density of the luminous matter. The Jaffe model should be viewed as a density in the given potential, which can be different from the potential generated by the density of the Jaffe model itself. Thus, the velocity dispersion for the Jaffe part of our model is given by:

$$\sigma_{\rm r}^2 = \frac{1}{\left(r_{\rm a}^2 + r^2\right)\rho_{\rm l}(r)} \int_{r'}^{\infty} \rho_{\rm l}(r')r'^2\frac{d\phi_{\rm T}}{dr'}\left[1 + (r_{\rm a}/r')^2\right]dr' \tag{A.11}$$

The solution of equation (A.11), can be obtained using *Mathematica*. Hence, near the center the radial velocity dispersion has the following expansion:

$$\sigma_{\rm r}^2 = \frac{M_{\rm l}}{2} + \left(\frac{M_{\rm d}}{a^2} - 2M_{\rm l}\right)r \tag{A.12}$$

Line of sight velocity dispersion of the model

The line of sight velocity dispersion $\sigma_{\rm p}^2$ at projected radius from the galaxy center R can be calculated using the following equation:

$$I(R)\sigma_{\rm p}^2 = \frac{2}{\gamma}\int_R^{\infty}\left(1 - \beta\frac{R^2}{r^2}\right)\frac{\rho\sigma_{\rm r}^2 r dr}{\sqrt{r^2 - R^2}} \tag{A.13}$$

(Hernquist 1990) In equation (A.13), β is equal to:

$$\beta = \frac{r^2}{r^2 + r_{\mathrm{a}}^2} \tag{A.14}$$

To obtain the line-of-sight velocity dispersion for the Jaffe part of the model ρ_{l} should be used (instead of ρ) and the projected surface brightness of the Jaffe part of the model. For a Jaffe model the projected surface brightness is given by:

$$I(R) = \frac{1}{4R} + \frac{1 - (2 - R^2)X(R)}{2\pi\,(1 - R^2)} \tag{A.15}$$

(Jaffe 1983) where R is the projected radius, and $X(R)$ is defined as:

$$X(R) \equiv \frac{1}{\sqrt{1 - R^2}} \operatorname{arccosh}\left(\frac{1}{r}\right) \qquad R < 1 \tag{A.16}$$

$$X(R) \equiv \frac{1}{\sqrt{R^2 - 1}} \arccos\left(\frac{1}{r}\right) \qquad R > 1 \tag{A.17}$$

(Tremaine et al. 1994).

Numerical integration is probably the best method for calculating the line-of-sight velocity dispersion. Since the integral in equation A.13 has to be taken from R to infinity and the integrand diverges at $r \approx R$, it is useful to use the substitution $z = R/r \; dr = -Rz^{-2}dz$ so that the integral is taken from 0 to 1, and then use Gauss-Chebyshev integration for dealing with the singularity at z =1.

Comparison of the line-of-sight velocity dispersion with real galaxies

The effect of adding a Hernquist halo to a Jaffe model is to flatten the line-of-sight velocity dispersion profile out to a certain radius at the center. By setting $a = \sqrt{M_{\mathrm{d}}/2M_{\mathrm{l}}}$, the radial velocity dispersion has its first derivative set to zero (see equation A.12). This also generates line-of-sight velocity dispersion which are flat at the centre. By varying the parameters M_{d}, a and r_a, it is possible to get a wide variety of velocity dispersion profile shapes. For haloes with large values of a and M_{d}, it is even possible to get line-of-sight velocity dispersions with a local minimum at the center and to have a local maximum at certain distance from the center.

A.2 GADGET-2 input file

Finally, we give an example of the input file of the GADGET-2 code to perform the simulations. In this file, the parameters that control the characteristics of the simulation are set; for instance, the name of the input and output files, the integration time, the output frequency, the accuracy of time integration, the force accuracy, the domain update frequency, the memory allocation, and the softening length.

```
%  Relevant files

InitCondFile   M_7.ggd
OutputDir      .

EnergyFile         energy.txt
InfoFile           info.txt
TimingsFile        timings.txt
CpuFile            cpu.txt

RestartFile        restart
SnapshotFileBase   snapshot

OutputListFilename parameterfiles/output_list.txt

% CPU time -limit

TimeLimitCPU      345600  % seconds
ResubmitOn        0
ResubmitCommand   my-scriptfile


% Code options

ICFormat                 1
SnapFormat               1
ComovingIntegrationOn    0

TypeOfTimestepCriterion  0
OutputListOn             0
PeriodicBoundariesOn     0
```

```
%  Caracteristics of run

TimeBegin          25546.0472   % Begin of the simulation
TimeMax            25696.7672   % End of the simulation

Omega0               0
OmegaLambda          0
OmegaBaryon          0
HubbleParam        1.0
BoxSize              0

% Output frequency

TimeBetSnapshot        20.
TimeOfFirstSnapshot    25546.0472

CpuTimeBetRestartFile     10800.0    ; here in seconds
TimeBetStatistics         0.5

NumFilesPerSnapshot       1
NumFilesWrittenInParallel 1

% Accuracy of time integration
ErrTolIntAccuracy     0.04
CourantFac            0.15
MaxSizeTimestep       0.1
MinSizeTimestep       0.0001


% Tree algorithm, force accuracy, domain update frequency

ErrTolTheta            0.7
TypeOfOpeningCriterion 0
ErrTolForceAcc         0.005
TreeDomainUpdateFrequency    0.1


%  Further parameters of SPH

DesNumNgb              80
```

```
MaxNumNgbDeviation      10
ArtBulkViscConst        0.75
InitGasTemp             10000         % always ignored if set to 0
MinGasTemp              50

% Memory allocation

PartAllocFactor       80
TreeAllocFactor       0.999
BufferSize            120          % in MByte


% System of units

UnitLength_in_cm          1;3.085678e21        ;  1.0 kpc
UnitMass_in_g             1;1.989e43           ;  1.0e10 solar masses
UnitVelocity_in_cm_per_s 1;1e5                 ;  1 km/sec
GravityConstantInternal  1;0


% Softening lengths

MinGasHsmlFractional 2.

SofteningGas       0
SofteningHalo      0
SofteningDisk      0.02
SofteningBulge     0.04
SofteningStars     0
SofteningBndry     0

SofteningGasMaxPhys       0
SofteningHaloMaxPhys      0
SofteningDiskMaxPhys      0.02
SofteningBulgeMaxPhys     0.04
SofteningStarsMaxPhys     0
SofteningBndryMaxPhys     0

MaxRMSDisplacementFac 0.2
```

B

Appendix section of chapter 5

Example of the input file of the GADGET-2 code to perform the simulations. In this file are set the parameters that control the characteristics of the simulation such as: the name of the input and output files, the integration time, the output frequency, the accuracy of time integration, the force accuracy, the domain update frequency, the memory allocation and the softening length.

B.1 GADGET-2 input file

```
%  Relevant files

InitCondFile       /gpfs/projects/can11/can11002/M3TF35D/M3N555D/galaxy.ggd
OutputDir          /gpfs/projects/can11/can11002/M3TF35D/M3N555D
EnergyFile         energy.txt
InfoFile           info.txt
TimingsFile        timings.txt
CpuFile            cpu.txt
RestartFile        restart
SnapshotFileBase   snapshot
OutputListFilename parameterfiles/output_list.txt

% CPU time -limit
TimeLimitCPU     126300  % seconds
ResubmitOn        0
ResubmitCommand   my-scriptfile

% Code options
```

```
ICFormat                1
SnapFormat              1
ComovingIntegrationOn   0
TypeOfTimestepCriterion 0
OutputListOn            0
PeriodicBoundariesOn    0

%  Caracteristics of run
TimeBegin           0.0     % Begin of the simulation
TimeMax           200.0     % End of the simulation

Omega0              0
OmegaLambda          0
OmegaBaryon          0
HubbleParam         1.0
BoxSize              0

% Output frequency
TimeBetSnapshot        5.
TimeOfFirstSnapshot    0
CpuTimeBetRestartFile     1800.0    ; here in seconds
TimeBetStatistics         1.0
NumFilesPerSnapshot       1
NumFilesWrittenInParallel 1

% Accuracy of time integration
ErrTolIntAccuracy      0.02
CourantFac             0.15
MaxSizeTimestep       0.1
MinSizeTimestep       0.001

% Tree algorithm, force accuracy, domain update frequency
ErrTolTheta            0.8
TypeOfOpeningCriterion 1
ErrTolForceAcc         0.005

TreeDomainUpdateFrequency    0.1

%  Further parameters of SPH
DesNumNgb              80
```

```
MaxNumNgbDeviation     10
ArtBulkViscConst       0.75
InitGasTemp            10000         % always ignored if set to 0
MinGasTemp             50

% Memory allocation
PartAllocFactor       17.5
TreeAllocFactor       0.999
BufferSize            70          % in MByte

% System of units
UnitLength_in_cm         1;3.085678e21        ;  1.0 kpc
UnitMass_in_g            1;1.989e43           ;  1.0e10 solar masses
UnitVelocity_in_cm_per_s 1;1e5                ;  1 km/sec
GravityConstantInternal  1;0

% Softening lengths
MinGasHsmlFractional 2.
SofteningGas       0
SofteningHalo      0.05
SofteningDisk      0.02
SofteningBulge     0.01
SofteningStars     0
SofteningBndry     0

SofteningGasMaxPhys       0
SofteningHaloMaxPhys      0.05
SofteningDiskMaxPhys      0.02
SofteningBulgeMaxPhys     0.01
SofteningStarsMaxPhys     0
SofteningBndryMaxPhys     0

MaxRMSDisplacementFac 0.2
```

B.2 Queue system

File the set of instructions to put in queue the simulations.

```
#\! /bin/bash
#
# @ job_name = M3N555D
# @ initialdir =/gpfs/projects/can11/can11002/M3TF35D/M3N555D
# @ output = OUTPUT/g2.%j.out
# @ error =  OUTPUT/g2.%j.err
# @ total_tasks = 128
# @ wall_clock_limit = 35:00:00
# @

#environment
export MP_EUILIB=gm
export OBJECT_MODE=32
export MP_RSH=ssh

srun  /gpfs/projects/can11/bin/Gadget2 galaxy.param
```

B.3 Orbit of the encounter

Example of the input file for the program to place in orbit the galaxies models.

```
galaxia.xvp
satelite.xvp
M3N555P10R.xvp
 $parslist
     model1 = 1
     model2 = 1
     massrat = 0.11
     sizerat = 0.39
     sep0 = 15.0
     vrad = -0.00131
     vtan = 0.24331
     theta1 = 150.
     phi1 = 180.
     theta2 = 25.
```

```
    phi2 = 90.
$END
```

Bibliography

Aarseth, S. J. 1963, MNRAS, 126, 223

Aarseth, S. J. 1985, in Multiple time scales, p. 377 - 418, ed. J. U. Brackbill & B. I. Cohen, 377–418

Aarseth, S. J. 1999, PASP, 111, 1333

Abadi, M. G., Navarro, J. F., Steinmetz, M., & Eke, V. R. 2003a, ApJ, 591, 499

Abadi, M. G., Navarro, J. F., Steinmetz, M., & Eke, V. R. 2003b, ApJ, 597, 21

Abazajian, K., Adelman-McCarthy, J. K., Agüeros, M. A., et al. 2003, AJ, 126, 2081

Aguerri, J. A. L. 2012, Advances in Astronomy, 2012

Aguerri, J. A. L., Balcells, M., & Peletier, R. F. 2001, A&A, 367, 428

Arimoto, N. & Yoshii, Y. 1986, A&A, 164, 260

Athanassoula, E., Puerari, I., & Bosma, A. 1997, MNRAS, 286, 284

Bachiller, R. 2009, Astronomía: De Galileo a los telescopios espaciales, ed. L. S. L.

Balcells, M. & Peletier, R. F. 1994, AJ, 107, 135

Balcells, M. & Quinn, P. J. 1990, ApJ, 361, 381

Barnes, J. & Hut, P. 1986, Nature, 324, 446

Bekki, K. & Shioya, Y. 1999, ApJ, 513, 108

Belokurov, V., Walker, M. G., Evans, N. W., et al. 2010, ApJL, 712, L103

Bernardi, M., Sheth, R. K., Nichol, R. C., et al. 2006, AJ, 131, 2018

Bertin, G., Ciotti, L., & Del Principe, M. 2002, A&A, 386, 149

Bezanson, R., van Dokkum, P. G., Tal, T., et al. 2009, ApJ, 697, 1290

Binney, J. 1987, in NATO ASIC Proc. 207: The Galaxy, ed. G. Gilmore & B. Carswell, 399–412

Binney, J. & Tremaine, S. 2008, Galactic Dynamics: Second Edition (Princeton University Press)

Bird, J. C., Kazantzidis, S., & Weinberg, D. H. 2012, MNRAS, 420, 913

Blanton, M. R., Hogg, D. W., Bahcall, N. A., et al. 2003, ApJ, 592, 819

Bournaud, F. 2009, ArXiv e-prints

Bournaud, F., Chapon, D., Teyssier, R., et al. 2011, ApJ, 730, 4

Bournaud, F. & Combes, F. 2004, in SF2A-2004: Semaine de l'Astrophysique Francaise, ed. F. Combes, D. Barret, T. Contini, F. Meynadier, & L. Pagani, 645

Bournaud, F., Elmegreen, B. G., & Elmegreen, D. M. 2007, ApJ, 670, 237

Bournaud, F., Elmegreen, B. G., & Martig, M. 2009, ApJL, 707, L1

Bournaud, F., Jog, C. J., & Combes, F. 2005, A&A, 437, 69

Bovy, J., Rix, H.-W., Liu, C., et al. 2012, ApJ, 753, 148

Bower, R. G., Lucey, J. R., & Ellis, R. S. 1992a, MNRAS, 254, 589

Bower, R. G., Lucey, J. R., & Ellis, R. S. 1992b, MNRAS, 254, 589

Boylan-Kolchin, M., Ma, C.-P., & Quataert, E. 2005, MNRAS, 362, 184

Brook, C. B., Gibson, B. K., Martel, H., & Kawata, D. 2005, ApJ, 630, 298

Bryan, G. L. & Norman, M. L. 1998, ApJ, 495, 80

Buitrago, F., Trujillo, I., Conselice, C. J., et al. 2008, ApJL, 687, L61

Bundy, K., Ellis, R. S., Conselice, C. J., et al. 2006, ApJ, 651, 120

Cappellari, M., Bacon, R., Bureau, M., et al. 2006, MNRAS, 366, 1126

Cappellari, M., Emsellem, E., Krajnović, D., et al. 2011, MNRAS, 416, 1680

Cappellari, M., McDermid, R. M., Alatalo, K., et al. 2012, Nature, 484, 485

Carlberg, R. G. 1984, ApJ, 286, 416

Cenarro, A. J. & Trujillo, I. 2009, ApJL, 696, L43

Chen, B., Stoughton, C., Smith, J. A., et al. 2001, ApJ, 553, 184

Cheng, J. Y., Rockosi, C. M., Morrison, H. L., et al. 2012, ApJ, 746, 149

Chiosi, C. & Carraro, G. 2002, MNRAS, 335, 335

Cid Fernandes, R., Mateus, A., Sodré, L., Stasińska, G., & Gomes, J. M. 2005, MNRAS, 358, 363

Cimatti, A., Cassata, P., Pozzetti, L., et al. 2008, A&A, 482, 21

Cimatti, A., Nipoti, C., & Cassata, P. 2012, MNRAS, 422, L62

Closson Ferguson, H. & CANDELS Collaboration. 2011, in American Astronomical Society Meeting Abstracts No. 218, 328.01

Combes, F. 2009, in Astronomical Society of the Pacific Conference Series, Vol. 419, Galaxy Evolution: Emerging Insights and Future Challenges, ed. S. Jogee, I. Marinova, L. Hao, & G. A. Blanc, 31

Combes, F. 2011, in IAU Symposium, Vol. 271, IAU Symposium, ed. N. H. Brummell, A. S. Brun, M. S. Miesch, & Y. Ponty, 119–126

Comerón, S., Elmegreen, B. G., Knapen, J. H., et al. 2011, ApJ, 741, 28

Conselice, C. J. 2003, ApJS, 147, 1

Conselice, C. J. 2006, ApJ, 638, 686

Conselice, C. J., Bundy, K., Trujillo, I., et al. 2007, MNRAS, 381, 962

Cooper, M. C., Griffith, R. L., Newman, J. A., et al. 2012, MNRAS, 419, 3018

Cox, T. J., Dutta, S. N., Di Matteo, T., et al. 2006, ApJ, 650, 791

Daddi, E., Renzini, A., Pirzkal, N., et al. 2005, ApJ, 626, 680

Dalcanton, J. J. & Bernstein, R. A. 2002, AJ, 124, 1328

Davis, M., Faber, S. M., Newman, J., et al. 2003, in Society of Photo-Optical Instrumentation Engineers (SPIE) Conference Series, Vol. 4834, Society of Photo-Optical Instrumentation Engineers (SPIE) Conference Series, ed. P. Guhathakurta, 161–172

de Jong, R. S. 1996, A&A, 313, 45

De Lucia, G. & Blaizot, J. 2007, MNRAS, 375, 2

de Vaucouleurs, G. 1959, Handbuch der Physik, 53, 275

Dehnen, W. 2000, in Astronomische Gesellschaft Meeting Abstracts, Vol. 17, Astronomische Gesellschaft Meeting Abstracts, ed. R. E. Schielicke, 1

Dehnen, W. 2001, MNRAS, 324, 273

den Brok, M., Peletier, R. F., Valentijn, E. A., et al. 2011, MNRAS, 414, 3052

Di Matteo, P., Lehnert, M. D., Qu, Y., & van Driel, W. 2011, A&A, 525, L3

Di Matteo, P., Pipino, A., Lehnert, M. D., Combes, F., & Semelin, B. 2009, A&A, 499, 427

Djorgovski, S. & Davis, M. 1987, ApJ, 313, 59

Doménech-Moral, M., Martínez-Serrano, F. J., Domínguez-Tenreiro, R., & Serna, A. 2012, MNRAS, 421, 2510

D'Onghia, E. & Burkert, A. 2004, ApJL, 612, L13

Dressler, A. 1980, ApJ, 236, 351

Dunkley, J., Spergel, D. N., Komatsu, E., et al. 2009, ApJ, 701, 1804

Eggen, O. J., Lynden-Bell, D., & Sandage, A. R. 1962, ApJ, 136, 748

Eliche-Moral, M. C., Balcells, M., Aguerri, J. A. L., & Gonzalez-Garcia, A. C. 2005, ArXiv Astrophysics e-prints

Eliche-Moral, M. C., Balcells, M., Aguerri, J. A. L., & González-García, A. C. 2006, A&A, 457, 91

Eliche-Moral, M. C., González-García, A. C., Aguerri, J. A. L., et al. 2012, A&A, 547, A48

Eliche-Moral, M. C., González-García, A. C., Balcells, M., et al. 2011, A&A, 533, A104

Emsellem, E., Cappellari, M., Krajnović, D., et al. 2007, MNRAS, 379, 401

Eskridge, P. B. & Frogel, J. A. 1999, Ap&SS, 269, 427

Evans, N. W. 1993, MNRAS, 260, 191

Faber, S. M. & Jackson, R. E. 1976, ApJ, 204, 668

Fan, L., Lapi, A., Bressan, A., et al. 2010, ApJ, 718, 1460

Fan, L., Lapi, A., De Zotti, G., & Danese, L. 2008, ApJL, 689, L101

Fernández Lorenzo, M., Cepa, J., Bongiovanni, A., et al. 2011, A&A, 526, A72

Ferré-Mateu, A., Vazdekis, A., Trujillo, I., et al. 2012, MNRAS, 423, 632

Fisher, D., Franx, M., & Illingworth, G. 1995, ApJ, 448, 119

Forbes, D. A., Sánchez-Blázquez, P., & Proctor, R. 2005, MNRAS, 361, L6

Forbes, J., Krumholz, M., & Burkert, A. 2012, ApJ, 754, 48

Franx, M. & Illingworth, G. 1990, ApJL, 359, L41

Franx, M., Moorwood, A., Rix, H.-W., et al. 2000, The Messenger, 99, 20

Garnett, D. R. 2002, ApJ, 581, 1019

Gavazzi, G., Garilli, B., & Boselli, A. 1990, A&AS, 83, 399

Gibson, B. K. 1997, MNRAS, 290, 471

González-García, A. C. & Balcells, M. 2005, MNRAS, 357, 753

González-García, A. C., Oñorbe, J., Domínguez-Tenreiro, R., & Gómez-Flechoso, M. Á. 2009, A&A, 497, 35

González-García, A. C. & van Albada, T. S. 2003, MNRAS, 342, L36

Gorgas, J., Efstathiou, G., & Aragon Salamanca, A. 1990, MNRAS, 245, 217

Graham, A. W. 2011, ArXiv e-prints

Greengard, L. & Rokhlin, V. 1987, J. Comput. Phys., 2, 23

Guo, Y., McIntosh, D. H., Mo, H. J., et al. 2009, MNRAS, 398, 1129

Guo, Y., McIntosh, D. H., Mo, H. J., et al. 2010, VizieR Online Data Catalog, 739, 81129

Hemsendorf, M., Spurzem, R., & Sigurdsson, S. 1997, in Astronomische Gesellschaft Abstract Series, Vol. 13, Astronomische Gesellschaft Abstract Series, ed. R. E. Schielicke, 53

Hernquist, L. 1990, ApJ, 356, 359

Hernquist, L. 1993, ApJ, 409, 548

Hernquist, L. & Katz, N. 1989, ApJS, 70, 419

Hernquist, L. & Ostriker, J. P. 1992, ApJ, 386, 375

Hilz, M., Naab, T., Ostriker, J. P., et al. 2012, ArXiv e-prints

Hockney, R. W. & Eastwood, J. W. 1988, Computer simulation using particles

Holmberg, E. 1941, ApJ, 94, 385

Hopkins, P. F., Bundy, K., Hernquist, L., Wuyts, S., & Cox, T. J. 2010a, MNRAS, 401, 1099

Hopkins, P. F., Cox, T. J., Dutta, S. N., et al. 2009a, ApJS, 181, 135

Hopkins, P. F., Croton, D., Bundy, K., et al. 2010b, ApJ, 724, 915

Hopkins, P. F., Hernquist, L., Cox, T. J., et al. 2005, ApJ, 630, 705

Hopkins, P. F., Hernquist, L., Cox, T. J., Dutta, S. N., & Rothberg, B. 2008a, ApJ, 679, 156

Hopkins, P. F., Hernquist, L., Cox, T. J., Keres, D., & Wuyts, S. 2009b, ApJ, 691, 1424

Hopkins, P. F., Hernquist, L., Cox, T. J., & Kereš, D. 2008b, ApJS, 175, 356

Hubble, E. P. 1936, Realm of the Nebulae

Huertas-Company, M., Aguerri, J. A. L., Bernardi, M., Mei, S., & Sánchez Almeida, J. 2011, A&A, 525, A157

Hut, M. Trenti, P. 2008, Scholarpedia, 3, 3930

Isobe, T., Feigelson, E. D., Akritas, M. G., & Babu, G. J. 1990, ApJ, 364, 104

Ivison, R. J., Smail, I., Amblard, A., et al. 2012, MNRAS, 3496

Jaffe, W. 1983, MNRAS, 202, 995

Jorgensen, I., Franx, M., & Kjaergaard, P. 1996, MNRAS, 280, 167

Kassin, S. A., Weiner, B. J., Faber, S. M., et al. 2012, ApJ, 758, 106

Kaufmann, T., Mayer, L., Carollo, M., & Feldmann, R. 2012, ArXiv e-prints

Kaviraj, S., Peirani, S., Khochfar, S., Silk, J., & Kay, S. 2009, MNRAS, 394, 1713

Kawata, D. 1999, PASJ, 51, 931

Kawata, D. & Gibson, B. K. 2003, MNRAS, 346, 135

Kazantzidis, S., Bullock, J. S., Zentner, A. R., Kravtsov, A. V., & Moustakas, L. A. 2008, ApJ, 688, 254

Kennicutt, Jr., R. C., Roettiger, K. A., Keel, W. C., van der Hulst, J. M., & Hummel, E. 1987, AJ, 93, 1011

Khochfar, S. & Silk, J. 2006, ApJL, 648, L21

King, I. R. 1966, AJ, 71, 64

Knapen, J. H., Comeron, S., Elmegreen, B., Sheth, K., & S4G Collaboration. 2012, in American Astronomical Society Meeting Abstracts, Vol. 219, American Astronomical Society Meeting Abstracts, 417.04

Kobayashi, C. 2004, MNRAS, 347, 740

Koleva, M., Prugniel, P., de Rijcke, S., & Zeilinger, W. W. 2011, MNRAS, 417, 1643

Kormendy, J. 1977, ApJ, 218, 333

Kormendy, J. 1989, ApJL, 342, L63

Kormendy, J. & Bender, R. 1996, ApJL, 464, L119

Kormendy, J. & Bender, R. 2012, ApJS, 198, 2

Kormendy, J. & Fisher, D. B. 2005, in Revista Mexicana de Astronomia y Astrofisica Conference Series, Vol. 23, Revista Mexicana de Astronomia y Astrofisica Conference Series, ed. S. Torres-Peimbert & G. MacAlpine, 101–108

Kormendy, J. & Kennicutt, Jr., R. C. 2004, ARA&A, 42, 603

Kriek, M., van der Wel, A., van Dokkum, P. G., Franx, M., & Illingworth, G. D. 2008, ApJ, 682, 896

Kroupa, P. 2002, MNRAS, 330, 707

Kuijken, K. & Dubinski, J. 1994, MNRAS, 269, 13

Kuijken, K. & Dubinski, J. 1995, MNRAS, 277, 1341

Kuijken, K. & Dubinski, J. 2011, Astrophysics Source Code Library, 9011

La Barbera, F., Lopes, P. A. A., de Carvalho, R. R., de La Rosa, I. G., & Berlind, A. A. 2010, MNRAS, 408, 1361

Larson, R. B. 1974, MNRAS, 166, 585

Larson, R. B. 1975, MNRAS, 173, 671

Laurikainen, E., Salo, H., Buta, R., Knapen, J. H., & Comerón, S. 2010, MNRAS, 405, 1089

Leauthaud, A., Tinker, J., Behroozi, P. S., Busha, M. T., & Wechsler, R. H. 2011, ApJ, 738, 45

Lequeux, J., Peimbert, M., Rayo, J. F., Serrano, A., & Torres-Peimbert, S. 1979, A&A, 80, 155

Li, Y., Hernquist, L., Robertson, B., et al. 2007, ApJ, 665, 187

Lintott, C., Schawinski, K., Bamford, S., et al. 2011, MNRAS, 410, 166

Lintott, C. J., Schawinski, K., Slosar, A., et al. 2008, MNRAS, 389, 1179

López-Sanjuan, C., Balcells, M., García-Dabó, C. E., et al. 2009a, ApJ, 694, 643

López-Sanjuan, C., Balcells, M., Pérez-González, P. G., et al. 2009b, A&A, 501, 505

López-Sanjuan, C., Balcells, M., Pérez-González, P. G., et al. 2010, ApJ, 710, 1170

López-Sanjuan, C., Le Fèvre, O., Ilbert, O., et al. 2012, ArXiv e-prints

Malin, D. F. & Carter, D. 1980, Nature, 285, 643

Malin, D. F. & Carter, D. 1983, ApJ, 274, 534

Martinelli, A., Matteucci, F., & Colafrancesco, S. 1998, MNRAS, 298, 42

Martinez-Manso, J., Guzman, R., Barro, G., et al. 2011, ApJL, 738, L22

Martínez-Serrano, F. J., Serna, A., Domínguez-Tenreiro, R., & Mollá, M. 2008, MNRAS, 388, 39

McIntosh, D. H., Bell, E. F., Rix, H.-W., et al. 2005, ApJ, 632, 191

McMillan, S. L. W. & Aarseth, S. J. 1993, ApJ, 414, 200

Mehlert, D., Thomas, D., Saglia, R. P., Bender, R., & Wegner, G. 2003, A&A, 407, 423

Méndez-Abreu, J., Aguerri, J. A. L., Corsini, E. M., & Simonneau, E. 2008, A&A, 478, 353

Merritt, D. 1985, AJ, 90, 1913

Mihos, J. C. 1995, ApJL, 438, L75

Minchev, I., Famaey, B., Quillen, A. C., et al. 2012, ArXiv e-prints

Moni Bidin, C., Carraro, G., & Méndez, R. A. 2012, ApJ, 747, 101

Morgan, W. W. & Mayall, N. U. 1957, PASP, 69, 291

Naab, T. & Burkert, A. 2003, ApJ, 597, 893

Naab, T., Johansson, P. H., & Ostriker, J. P. 2009, ApJL, 699, L178

Naab, T., Johansson, P. H., Ostriker, J. P., & Efstathiou, G. 2007, ApJ, 658, 710

Naab, T., Khochfar, S., & Burkert, A. 2006, ApJL, 636, L81

Naab, T. & Trujillo, I. 2006, MNRAS, 369, 625

Newman, A. B., Ellis, R. S., Bundy, K., & Treu, T. 2012, ApJ, 746, 162

Nigoche-Netro, A., Ruelas-Mayorga, A., & Franco-Balderas, A. 2009, MNRAS, 392, 1060

Nipoti, C., Treu, T., Auger, M. W., & Bolton, A. S. 2009, ApJL, 706, L86

Nipoti, C., Treu, T., Leauthaud, A., et al. 2012, MNRAS, 422, 1714

Nitadori, K. & Aarseth, S. J. 2012, MNRAS, 424, 545

Norman, M. L., Bryan, G. L., Harkness, R., et al. 2007, ArXiv e-prints

Ogando, R. L. C., Maia, M. A. G., Chiappini, C., et al. 2005, ApJL, 632, L61

Oser, L., Naab, T., Ostriker, J. P., & Johansson, P. H. 2012, ApJ, 744, 63

Oser, L., Ostriker, J. P., Naab, T., Johansson, P. H., & Burkert, A. 2010, ApJ, 725, 2312

O'Shea, B. W., Bryan, G., Bordner, J., et al. 2004, ArXiv Astrophysics e-prints

Patton, D. R., Carlberg, R. G., Marzke, R. O., et al. 2000, ApJ, 536, 153

Peñarrubia, J., Zucker, D. B., Irwin, M. J., et al. 2011, ApJL, 727, L2

Peletier, R. F. 1993, in European Southern Observatory Conference and Workshop Proceedings, Vol. 45, European Southern Observatory Conference and Workshop Proceedings, ed. I. J. Danziger, W. W. Zeilinger, & K. Kjär, 409

Peletier, R. F., Davies, R. L., Illingworth, G. D., Davis, L. E., & Cawson, M. 1990, AJ, 100, 1091

Peng, C. Y., Ho, L. C., Impey, C. D., & Rix, H.-W. 2002, AJ, 124, 266

Pérez-González, P. G., Gil de Paz, A., Zamorano, J., et al. 2003, MNRAS, 338, 525

Pérez-González, P. G., Trujillo, I., Barro, G., et al. 2008, ApJ, 687, 50

Pipino, A., D'Ercole, A., Chiappini, C., & Matteucci, F. 2010, MNRAS, 407, 1347

Prendergast, K. H. & Tomer, E. 1970, AJ, 75, 674

Prieto, M., Eliche-Moral, M. C., Balcells, M., et al. 2012, ArXiv e-prints

Qu, Y., Di Matteo, P., Lehnert, M. D., van Driel, W., & Jog, C. J. 2011, A&A, 535, A5

Quilis, V. 2004, MNRAS, 352, 1426

Quilis, V. & Trujillo, I. 2012, ApJL, 752, L19

Quinn, P. J. 1984, ApJ, 279, 596

Quinn, P. J., Hernquist, L., & Fullagar, D. P. 1993, ApJ, 403, 74

Rix, H.-W., Barden, M., Beckwith, S. V. W., et al. 2004, ApJS, 152, 163

Robin, A. C., Haywood, M., Creze, M., Ojha, D. K., & Bienayme, O. 1996, A&A, 305, 125

Roškar, R., Debattista, V. P., Brooks, A. M., et al. 2010, MNRAS, 408, 783

Roškar, R., Debattista, V. P., Stinson, G. S., et al. 2008, ApJL, 675, L65

Sakai, S., Mould, J. R., Hughes, S. M. G., et al. 2000, ApJ, 529, 698

Sanchez-Blazquez, P. 2004, PhD thesis, Universidad Complutense de Madrid, Spain

Sánchez-Blázquez, P., Forbes, D. A., Strader, J., Brodie, J., & Proctor, R. 2007, MNRAS, 377, 759

Sánchez-Blázquez, P., Gorgas, J., & Cardiel, N. 2006, A&A, 457, 823

Sandage, A., Freeman, K. C., & Stokes, N. R. 1970, ApJ, 160, 831

Scarlata, C., Carollo, C. M., Lilly, S. J., et al. 2007, ApJS, 172, 494

Sellwood, J. A. & Debattista, V. P. 2009, MNRAS, 398, 1279

Serna, A., Domínguez-Tenreiro, R., & Sáiz, A. 2003, ApJ, 597, 878

Sersic, J. L. 1968, Atlas de galaxias australes

Shen, S., Mo, H. J., White, S. D. M., et al. 2003, MNRAS, 343, 978

Shu, F. H. 1969, ApJ, 158, 505

Smulders, M. & Balcells, M. 1995, Master's thesis, Groningen University

Spitzer, Jr., L. 1942, ApJ, 95, 329

Spolaor, M., Proctor, R. N., Forbes, D. A., & Couch, W. J. 2009, ApJL, 691, L138

Springel, V. 2005, MNRAS, 364, 1105

Springel, V., Di Matteo, T., & Hernquist, L. 2005a, ApJL, 620, L79

Springel, V., White, S. D. M., Jenkins, A., et al. 2005b, Nature, 435, 629

Springel, V., Yoshida, N., & White, S. D. M. 2001, NewA, 6, 79

Stadel, J. G. 2001, PhD thesis, UNIVERSITY OF WASHINGTON

Strateva, I., Ivezić, Ž., Knapp, G. R., et al. 2001, AJ, 122, 1861

Szomoru, D., Franx, M., & van Dokkum, P. G. 2012, ApJ, 749, 121

Tapia, M. T., Balcells, M., & Eliche-Moral, M. C. 2010a, in IAU Symposium, Vol. 262, IAU Symposium, ed. G. Bruzual & S. Charlot, 432–433

Tapia, M. T., Balcells, M., & Eliche-Moral, M. C. 2010b, in American Institute of Physics Conference Series, Vol. 1240, American Institute of Physics Conference Series, ed. V. P. Debattista & C. C. Popescu, 423–424

Toomre, A. & Toomre, J. 1972, ApJ, 178, 623

Tremaine, S., Richstone, D. O., Byun, Y.-I., et al. 1994, AJ, 107, 634

Tremonti, C. A., Heckman, T. M., Kauffmann, G., et al. 2004, ApJ, 613, 898

Trujillo, I., Cenarro, A. J., de Lorenzo-Cáceres, A., et al. 2009, ApJL, 692, L118

Trujillo, I., Conselice, C. J., Bundy, K., et al. 2007, MNRAS, 382, 109

Trujillo, I., Ferreras, I., & de La Rosa, I. G. 2011, MNRAS, 415, 3903

Trujillo, I., Förster Schreiber, N. M., Rudnick, G., et al. 2006, ApJ, 650, 18

Tully, R. B. & Fisher, J. R. 1977, A&A, 54, 661

Vale Asari, N., Stasińska, G., Cid Fernandes, R., et al. 2009, MNRAS, 396, L71

van Albada, T. S. 1982, MNRAS, 201, 939

van de Sande, J., Kriek, M., Franx, M., et al. 2011, ApJL, 736, L9

van den Bergh, S. 1976, ApJ, 206, 883

van den Bosch, F. C. 2001, MNRAS, 327, 1334

van der Kruit, P. C. & Freeman, K. C. 2011, ARA&A, 49, 301

van der Kruit, P. C. & Searle, L. 1981, A&A, 95, 105

van der Wel, A., Bell, E. F., van den Bosch, F. C., Gallazzi, A., & Rix, H.-W. 2009, ApJ, 698, 1232

van der Wel, A., Rix, H.-W., Wuyts, S., et al. 2011, ApJ, 730, 38

van Dokkum, P. G., Brammer, G., Fumagalli, M., et al. 2011, ApJL, 743, L15

van Dokkum, P. G., Franx, M., Kriek, M., et al. 2008, ApJL, 677, L5

van Dokkum, P. G., Kriek, M., & Franx, M. 2009, Nature, 460, 717

van Dokkum, P. G., Whitaker, K. E., Brammer, G., et al. 2010, ApJ, 709, 1018

Velazquez, H. & White, S. D. M. 1999, MNRAS, 304, 254

Villalobos, Á. & Helmi, A. 2008, MNRAS, 391, 1806

Villalobos, Á. & Helmi, A. 2009, MNRAS, 399, 166

Villalobos, Á., Kazantzidis, S., & Helmi, A. 2010, ApJ, 718, 314

Visvanathan, N. & Sandage, A. 1977, ApJ, 216, 214

von Hoerner, S. 1960, Z. Astrophys., 50, 184

Walker, I. R., Mihos, J. C., & Hernquist, L. 1996, ApJ, 460, 121

Weinberg, D. H., Hernquist, L., & Katz, N. 1997, ApJ, 477, 8

Weinzirl, T., Jogee, S., Conselice, C. J., et al. 2011, ApJ, 743, 87

Whitaker, K. E., Kriek, M., van Dokkum, P. G., et al. 2012, ApJ, 745, 179

White, S. D. M. 1980, MNRAS, 191, 1P

White, S. D. M. & Frenk, C. S. 1991, ApJ, 379, 52

White, S. D. M. & Rees, M. J. 1978, MNRAS, 183, 341

Whitmore, B. C. & Gilmore, D. M. 1991, ApJ, 367, 64

Yoachim, P. & Dalcanton, J. J. 2005, ApJ, 624, 701

Yoachim, P. & Dalcanton, J. J. 2006, AJ, 131, 226